Bridging large and small scales of water models using hybrid Molecular Dynamics/Fluctuating Hydrodynamics framework

ARTURS SCUKINS

Doctor Of Philosophy

– ASTON UNIVERSITY –

September 2014

ASTON UNIVERSITY

Bridging large and small scales of water models using hybrid Molecular Dynamics/Fluctuating Hydrodynamics framework

ARTURS SCUKINS

Doctor Of Philosophy, 2014

Thesis Summary

This thesis presents a two-dimensional water model investigation and development of a multiscale method for the modelling of large systems, such as virus in water or peptide immersed in the solvent.

We have implemented a two-dimensional 'Mercedes Benz' (MB) or BN2D water model using Molecular Dynamics. We have studied its dynamical and structural properties dependence on the model's parameters. For the first time we derived formulas to calculate thermodynamic properties of the MB model in the microcanonical (NVE) ensemble. We also derived equations of motion in the isothermal–isobaric (NPT) ensemble. We have analysed the rotational degree of freedom of the model in both ensembles.

We have developed and implemented a self-consistent multiscale method, which is able to communicate micro- and macro- scales. This multiscale method assumes, that matter consists of the two phases. One phase is related to micro- and the other to macroscale. We simulate the macro scale using Landau Lifshitz-Fluctuating Hydrodynamics, while we describe the microscale using Molecular Dynamics. We have demonstrated that the communication between the disparate scales is possible without introduction of fictitious interface or approximations which reduce the accuracy of the information exchange between the scales. We have investigated control parameters, which were introduced to control the contribution of each phases to the matter behaviour. We have shown, that microscales inherit dynamical properties of the macroscales and vice versa, depending on the concentration of each phase. We have shown, that Radial Distribution Function is not altered and velocity autocorrelation functions are gradually transformed, from Molecular Dynamics to Fluctuating Hydrodynamics description, when phase balance is changed.

In this work we test our multiscale method for the liquid argon, BN2D and SPC/E water models. For the SPC/E water model we investigate microscale fluctuations which are computed using advanced mapping technique of the small scales to the large scales, which was developed by Voulgarakisand et. al. [1].

Keywords: Hybrid methods, Multiscale methods, 'Mercedes Benz' water model, BN2D, Large and small scales, Molecular Dynamics, Landau Lifshitz-Fluctuating Hydrodynamics, CABARET

Acknowledgements

First and foremost I am grateful to my supervisor Dr Dmitry Nerukh for encouragement and valuable advices during my research at Aston University.

I wish to thank my colleagues Dr Evgen Pavlov and Dr Vitaly Bardik for support and guidance during the project.

Special thanks to my collaborating colleagues Dr Sergey Karabasov and Dr Anton Markesteijn from Cambridge University and Queen Mary University of London for an exceptional contribution to the project.

I would also like to thank Dr Makoto Taiji, Dr Vasily Goloviznin and Dr Ivan Korotkin for help with the technical aspects during my research.

Also I want to thank G8 Research Council Initiative on Multilateral Research Funding for giving me an opportunity to participate in the research.

The last but not the least thanks to my family for the strongest emotional support.

Contents

1 **Introduction** 14

1.1 Analytical methods 17

1.1.1 Matched asymptotics method 17

1.1.2 Multiscale expansion method 19

1.1.3 Dimensional analysis 19

1.2 Computational methods 19

1.2.1 Multigrid methods 20

1.2.2 Domain decomposition methods 21

1.2.3 Adaptive resolution methods 22

1.2.4 Dissipative Particle Dynamics 23

1.2.5 Hybrid Molecular Dynamics and Hydrodynamics methods 24

1.3 The main idea of our approach 25

1.4 Thesis outline 26

2 **Bridging large and small scales** 28

2.1 Conservation equations 29

2.1.1 Mass conservation 31

2.1.2 Momentum conservation 34

2.1.3 Energy conservation 36

2.2 Implementation 37

2.2.1 MD simulation 37

2.2.2 Landau Lifshitz-Fluctuating Hydrodynamics 40

2.2.3 Interpolation in between the scales 42

2.2.4 Communicating large and small scales 43

2.3 ‘One way’ coupling 45

2.3.1 FH phase 45

2.3.2 LL-FH simulation 46

2.3.3 MD phase . . . 48
2.3.4 MD simulation . . . 49
2.3.5 Stability analysis . . . 52
2.3.6 Structure and Dynamics of the liquid . . . 59
2.4 ‘Two way’ coupling . . . 60
2.4.1 FH phase . . . 62
2.4.2 MD phase . . . 63
2.4.3 Simulation . . . 64
2.4.4 Stability analysis . . . 64
2.4.5 Structure and Dynamics of the liquid . . . 70
2.5 Total energy rescaling . . . 72
2.5.1 Implementation . . . 74
2.6 Conclusions . . . 77

3 Water models 79
3.1 Two-dimensional ‘Mercedes Benz’ or BN2D water model . . . 80
3.1.1 Molecular model and details of computation . . . 81
3.1.2 Equations of motion . . . 82
3.1.3 Thermodynamics . . . 84
3.1.4 Structural and dynamic properties . . . 87
3.1.5 Simulation . . . 87
3.1.6 Analysis . . . 89
3.1.7 Summary . . . 99
3.2 ‘Two way’ coupling using BN2D water model . . . 101
3.2.1 Simulation . . . 101
3.2.2 Analysis . . . 103
3.2.3 Conclusions . . . 107
3.3 SPC/E water model implementation of the hybrid framework . . . 109
3.3.1 Model and details of computation . . . 109
3.3.2 Cubic spline interpolation . . . 111
3.3.3 Finite size of the water molecules . . . 112
3.3.4 Pure water . . . 115
3.3.5 Variable coupling parameter s . . . 119
3.3.6 Peptide in water . . . 121

4 Conclusions 124
4.1 BN2D water model 125
4.2 Bridging large and small scales 125
4.3 Pure water 126
4.4 Variable coupling parameter s 127
4.5 Peptide in water 127
4.6 Outlook 127

5 Supplementary files 136
5.1 Simulation of three-dimensional liquid argon with the variable coupling parameter s profile 136
5.2 Simulation of dialanine with 1444 SPC/E water molecules when the variable coupling parameter s profile is fixed to the simulation domain center 137
5.3 Simulation of dialanine with 30000 SPC/E water molecules when the variable coupling parameter s profile is fixed to the simulation domain center 137
5.4 Simulation of dialanine with 30000 SPC/E water molecules when the variable coupling parameter s profile is moving with the peptide's geometrical center . . . 137

A Appendix 141
A.1 Relaxation method 141
A.2 Method of characteristics ('one way' coupling case) 142
A.3 Method of characteristics ('two way' coupling case) 143
A.4 Ergodicity 145
A.5 Thermodynamics of BN2D water model in the NVE ensemble 146
  A.5.1 Temperature 148
  A.5.2 Pressure 148
  A.5.3 Isochoric heat capacity 149
  A.5.4 Isothermal compressibility 149
A.6 Equations of motion in the NPT ensemble 150
A.7 Program structure for the MB water model 154
A.8 Potential derivatives 154
  A.8.1 Lennard-Jones part 155
  A.8.2 Hydrogen bonding part 156
A.9 Predictor-Corrector method 158

List of Figures

1.1 Domain decomposition method for two non-overlapping different grids. The solution of the first subdomain is denoted as ξ_1 and the second as ξ_2, while the solution on the interface of these two subdomains as ϕ 21

1.2 Pictorial representation of the adaptive simulation box and local molecular representation. The low resolution (coarse-grained) region is on the right, indicated by B, and the high resolution (atomistic) region A is on the left. The transition (hybrid) region H with the switching function $w(x)$ (curve in grey) is in the middle; The figure is taken from [2] 22

1.3 The visibility of matter description is controlled by the parameter s. If $s = 1$ the matter is fully described by continuum phase, in the transition zone $0 < s < 1$ matter is represented by a mixture of both continuum and atomistic descriptions, if $s = 0$ fully atomistic description is considered 26

2.1 In the xy-plane a 2D simulation domain is shown, with the black dots representing MD particles; the FH phase is modelled on a regular grid (white lines); the coupling parameter s has a Gaussian profile in this example and its projection on the xy-plane is shown in colour 30

2.2 Schematic representation of the numerical schemes. a) Conserved variables of the MD and FH phase, such as density and momentum are defined at the cell's centre on the regular grid, while the mass and momentum fluxes are located on the cell faces. b) The CABARET numerical scheme evaluates conservative variables (circles) every half timestep, while the fluxes (triangles) are obtained every timestep between the conservative variables evaluation 42

2.3 Linear interpolation illustration in 2D space (x and y) 43

2.4 The relative difference between the FH and MD phase densities at one of the cells, when $\alpha^*, \beta^* = 2$ 53

2.5 The relative difference between the FH and MD phase densities at one of the cells, when $\alpha^*, \beta^* = 1000$ 53

2.6 The relative difference between the FH and MD phase densities at one of the cells, when $\alpha^*, \beta^* = 20000$ 54

2.7 The relative difference between the FH and MD phase velocities (x component) at one of the cells, when $\alpha^*, \beta^* = 2$ 55

2.8 The relative difference between the FH and MD phase velocities (x component) at one of the cells, when $\alpha^*, \beta^* = 1000$ 55

2.9 The relative difference between the FH and MD phase velocities (x component) at one of the cells, when $\alpha^*, \beta^* = 20000$ 56

2.10 Velocity fluctuations of the FH phase u_x and MD phase $\sum_p u_{xp}$, when $\alpha^*, \beta^* =$ 20000 and different coupling parameter s values; ‘one way’ coupling of 2D argon 56

2.11 The standard deviation of density of the coupled system $\tilde{\rho}$, when $\alpha^*, \beta^* = 20000$, pure FH phase ρ and MD phase $\sum_p \rho_p$ 58

2.12 The standard deviation of the velocity’s x component of the coupled system $\tilde{u}$, when $\alpha^*, \beta^* = 20000$, pure FH phase u_x and MD phase $\sum_p u_{xp}$ 58

2.13 The radial distribution functions of 2D liquid argon in the case of ‘one way’ coupling are the same for all s, α^* and β^* 59

2.14 MD particles velocity autocorrelation functions for $\alpha^*, \beta^* = 20000$ 60

2.15 The density and velocity fluctuations of the mixture (denoted by tilde), of the MD and FH phases in a random cell; the case of ‘two way’ coupling of 2D liquid argon; parameter $s = 0.1$; a) corresponds to the density and c) velocity x component, when $\alpha^* = 2,\ \beta^* = 50$; b) corresponds to the density and d) velocity x component, when $\alpha^* = 50,\ \beta^* = 50$ 65

2.16 The density and velocity fluctuations of the mixture (denoted by tilde), of the MD and FH phases in a random cell; the case of ‘two way’ coupling of 2D liquid argon; parameter $s = 0.8$; a) corresponds to the density and c) velocity x component, when $\alpha^* = 2,\ \beta^* = 50$; b) corresponds to the density and d) velocity x component, when $\alpha^* = 50,\ \beta^* = 50$ 66

2.17 The relative difference between the FH and MD phase densities if $s = 0.1$ in the case of ‘two way’ coupling of 2D liquid argon; single plots are depicted for all sets of β^*, when $\alpha^* = 50$ and $\alpha^* = 1000$, due to the negligible difference between plots; 67

2.18 The relative difference between the FH and MD phase densities if $s = 0.8$ in the case of ‘two way’ coupling of 2D liquid argon; single plots are depicted for all sets of β^*, when $\alpha^* = 50$ and $\alpha^* = 1000$, due to the negligible difference between plots; 68
2.19 The relative difference between the FH and MD phase velocities when $s = 0.1$ and $\alpha^* = 2$; in the case of ‘two way’ coupling of 2D liquid argon 69
2.20 The relative difference between the FH and MD phase velocities when $s = 0.1$ and $\alpha^* = 1000$; in the case of ‘two way’ coupling of 2D liquid argon 69
2.21 The relative difference between the FH and MD phase velocities when $s = 0.8$ and $\alpha^* = 2$; in the case of ‘two way’ coupling of 2D liquid argon 70
2.22 The relative difference between the FH and MD phase velocities when $s = 0.8$ and $\alpha^* = 1000$; in the case of ‘two way’ coupling of 2D liquid argon 70
2.23 MD particles velocity autocorrelation functions for $\alpha^*, \beta^* = 50$; in the case of ‘two way’ coupling of 2D liquid argon 71
2.24 Radial distribution function of 2D liquid argon is in the case of ‘two way’ coupling 72
2.25 The relative difference between the FH and MD phase a) densities and b) velocities; total energy rescaling is used, $\alpha^*, \beta^* = 20000$ 75
2.26 MD phase velocities of a random cell for $\alpha^*, \beta^* = 20000$ and $s = 0.1$, with (using α_E, black line) and without energy rescaling 76
2.27 α_E^* plots for different s values, $\alpha^*, \beta^* = 20000$, where velocity is rescaled from the total energy scaling concept 76
2.28 MD phase velocities of a random cell for $\alpha^*, \beta^* = 20000$ and $s = 0.8$, with (using α_E, black line) and without energy rescaling 77

3.1 Two-dimension ‘Mercedes Benz’ (MB or BN2D) water model 81
3.2 Simulated isothermal compressibility β_T^*, pressure P^*, isochoric heat capacity C_V^*, isothermal expansion coefficient α^* in the NVE ensemble, $\rho^* = 0.9$. The error bars for β_T^* are shown to illustrate slow convergence for this parameter 89
3.3 Experimental water isothermal compressibility β_T, pressure P, isochoric heat capacity C_V, isothermal expansion coefficient α (taken from [3]) 90
3.4 The fluctuations of the 1^{st} order derivative with respect to the area for different system sizes (the number of molecules is indicated), $T^* = 0.21$. 91
3.5 a) convergence of the 1^{st} order derivative of the MB potential with respect to area b) isothermal compressibility , $T^* = 0.21, N = 2500$ 91

3.6 Simulated isothermal compressibility β_T^*, volume V^*, isobaric heat capacity C_p^*, isothermal expansion coefficient α^* in the NPT ensemble, $P^* = 0.195$. 92
3.7 The dependence of the pressure for the NVE ensemble and density for the NPT ensemble on temperature. Two different simulations are depicted here, black squares are the density vs temperature in the NPT ensemble and red circles are the pressure vs temperature in the NVE ensemble. The blue arrowed line shows that for the temperature $T^* = 0.215$ and pressure $P^* = 0.195$ in the NPT ensemble density becomes $\rho^* = 0.9$, while in the case of the NVE ensemble with density $\rho^* = 0.9$ and temperature $T^* = 0.215$ pressure becomes $P^* = 0.195$, resulting in the same state of the system regardless the approach used 93
3.8 Velocity autocorrelation functions at $T^* = 0.195$ for BN2D and SPC water models 94
3.9 Radial distribution function at $T^* = 0.16$. The reference molecule is shown in green. The ‘interstitial’ water is magenta 95
3.10 Orientational distribution (3.38) of MB water as a function of distance at $T^* = 0.16$ 95
3.11 Radial distribution function for different σ_{HB}^* in orientational part of MB potential, at temperature 300K 96
3.12 Structures formed for different σ_{HB}^* in orientational part of the MB potential, at temperature 300K. Where a) $\sigma_{HB}^* = 0.0085$, b) $\sigma_{HB}^* = 0.085$, c,d) $\sigma_{HB}^* = 0.5$ . . . 97
3.13 Velocity autocorrelation function for different σ_{HB}^* in orientational part of the MB potential, at temperature 300 K 98
3.14 Rotation velocity autocorrelation function for different σ_{HB}^* in orientational part of the MB potential, at temperature 300 K 99
3.15 The standard deviation of the rotational velocity with the timestep dt^* (NVE ensemble). 100
3.16 Equation of state for MB water model. 102
3.17 Standard deviation of velocity x component of the pure MD phase (MB) $\sum_p u_{xp}$, FH phase u_x and coupled system’s mixture velocity $\tilde{u}_x$ 104
3.18 The difference between the mixture and phase velocities a) $\tilde{u}_x - \sum_p u_{xp}$ and b) $\tilde{u}_x - u_x$ for $s = 0.1$ and $s = 0.8$ 104
3.19 Velocity x component profiles of the MD phase $\sum_p u_{xp}$ and FH phase u_x; ‘two way’ coupling, BN2D water model; a) $s = 0.1$, b) $s = 0.8$ 105
3.20 Radial distribution function of BN2D water model for different coupling parameter s values 105
3.21 Translational velocity autocorrelation function for different s values calculated from the particles velocities 106

3.22 Translational velocity autocorrelation function for different s values calculated from the $\tilde{u}$ velocity fluctuations in the cell centres 107
3.23 SPC/E water model representation 110
3.24 Three-dimensional linear interpolation of the velocity component u_x 111
3.25 Cubic spline interpolation of the velocity component u_x 112
3.26 Contributions of a particle to the MD phase density and momentum is calculated as a fractions of its volume d_{mol}^3 in different cells 112
3.27 SPC/E water model MD phase density fluctuations in a random cell with and without 'blob' filter 113
3.28 SPC/E water model velocity x component fluctuations in a random cell with and without 'blob' filter 114
3.29 Standard deviation of the SPC/E water model MD phase density fluctuations with and without 'blob' filter, where ρ is measured in $\frac{Da}{nm^3}$ 114
3.30 Standard deviation of the SPC/E water model MD phase x velocity component fluctuations in $\frac{nm}{ps}$ with and without 'blob' filter 115
3.31 Radial distribution function of SPC/E water model $O-O$ (oxygen-oxygen) . . . 116
3.32 Radial distribution function of SPC/E water model $O-H$ (oxygen - hydrogen) . 116
3.33 Velocity autocorrelation function of the SPC/E water model particles for different parameter s 117
3.34 Standard deviations of the density for the pure and coupled system of SPC/E water model MD phase with different parameter s 118
3.35 Standard deviations of the velocity x component for pure and coupled system of SPC/E water model MD phase with different parameter s 118
3.36 3D liquid argon with sphere type profile of the coupling parameter s. Initially, particles in the center were marked in red colour, where $s = 0$, gradually changing colour to blue on the edges, where $s = 0.99$ (view of a slice) 120
3.37 A snapshot of the simulation of 3D liquid argon with sphere type profile of the coupling parameter s. Initially, particles in the center were marked in red colour, where $s = 0$, gradually changing colour to blue on the edges, where $s = 0.99$ (view of a slice) 121
3.38 Initial distribution of dialanine and 1444 SPC/E water molecules in simulation using variable coupling parameter s profile. Parameter s is zero for 40% of the simulation domain and positioned at its center. Then parameter s gradually (linear) increases to 0.99 at the edges 122

3.39 A snapshot of distribution of dialanine and 1444 SPC/E water molecules in simulation using variable coupling parameter s profile. Parameter s is zero for 40% of the simulation domain and positioned at its center. Then parameter s gradually (linear) increases to 0.99 at the edges 122

List of Tables

2.1 Lennard-Jones potential parameters, where N_A is Avagadro number [4] 52

2.2 ‘One way’ coupling simulation conditions in dimensionless units (LJ potential) . 52

2.3 The standard deviations of $\rho - \sum_p \rho_p$, for different α^*, β^* and s, (“-” unstable simulation); The standard deviation was calculated using 34000 FH iterations 57

2.4 The standard deviations of $u_x - \sum_p u_{xp}$ for different α^*, β^* and s, (“-” unstable simulation); The standard deviation was calculated using 34000 FH iterations . . 57

3.1 The variables used in MD simulations. r_{HB} is hydrogen bond length, m_{H_2O} is the water molecule mass, I is the moment of inertia [5], ε_{HB} is the hydrogen bond energy, ε_{LJ} is the Lennard-Jones energy, σ^*_{LJ} is 0.7 of the r^*_{HB} 89

1

Introduction

CONTENTS

1.1 Analytical methods 17
  1.1.1 Matched asymptotics method 17
  1.1.2 Multiscale expansion method 19
  1.1.3 Dimensional analysis 19
1.2 Computational methods 19
  1.2.1 Multigrid methods 20
  1.2.2 Domain decomposition methods 21
  1.2.3 Adaptive resolution methods 22
  1.2.4 Dissipative Particle Dynamics 23
  1.2.5 Hybrid Molecular Dynamics and Hydrodynamics methods 24
1.3 The main idea of our approach 25
1.4 Thesis outline 26

One of the most prominent scientific achievements in the last century was in the biomolecular computation. This discipline allows to create, control and manipulate biomolecular systems [6].

These systems are referred to as large biomolecular systems i.e proteins, that play vital role in living organisms. They perform various functions, such as replicating DNA, transporting molecules from one location to another, catalyzing metabolic reactions, and many more [7]. Proteins are characterized by long chains of amino acid residues. The sequence of these amino acids determine the folding of these chains into a specific structure, that defines protein's activity. Folded protein structures (conformations) can exist for a certain period of time, which lasts from minutes up to years. Later these folded proteins are dismantled by the cell's machinery. If proteins are misfolded, then they are destroyed more rapidly. It happens because misfolded proteins are unstable and more likely to be targeted for a destruction.

It is believed, that surrounding solvent molecules play important role in the process of protein folding [8]. Recent investigations showed connection between water molecules in the vicinity of the proteins and protein conformations [9].

According to the study, protein chains are guided by the water's hydration shell before conformation is performed. An ability to predict and control this guidance, which drives protein to a particular conformation, is highly demanded, because it defines all the rearrangements of the protein and its characteristics.

In order to simulate large systems, such as virus in water or the connection between water and protein molecules, computational techniques can be used. The best scenario, in terms of accuracy, would be to simulate the protein together with all water molecules available during the experiment. However, this task is computationally expensive, since accurate description of all molecules leads to enormous calculations. For this reason various computational tricks and approximations are employed, such that the number of solvent molecules is reduced or molecule's description is simplified.

For example, implicit solvent method which instead of considering solvent molecules explicitly represents them as a continuous medium. Thus, method reduces dramatically degrees of freedom of solvent, since its molecules are not considered explicitly. Implicit solvent models assume that non-polar atoms of a solute tend to gather together and occupy non-polar media, whereas polar and charged groups of the solute tend to remain in water [10]. The method is based on the Poisson equation which describes the electrostatic interactions. Therefore, protein is characterized with the point charges with known spatial distribution in a low dielectricum and the solvent posses high dielectric properties (contains ions distributed from Boltzmann statistics). Since, accurate Poisson-Boltzmann equation requires large computational effort, approximations are used, such as generalized Born approximation. Which replaces the electrostatic potential calculation with the approximate solvent-induced reaction field energy [11].

Implicit solvent methods are utilized in the well known software, such as CHARMM [12] or AMBER [13] and are frequently used for the study of the drug delivery problems (across biological membranes), protein folding, solute-solvent interactions in structural and chemical processes, etc. These methods proved to be effective, although they have drawbacks, such as inaccurate account for the hydrophobic effect (which is important in the folding processes) and hydrogen bonding with the solvent.

The study [9] demonstrated, that the amount of surrounding water (explicit description) cannot be reduced dramatically, hence not all approximations can be used.

Water molecule itself has a V shape structure with a characteristic diameter of 2.74Å and is commonly referred to as a small scale description of the matter.

In order to evaluate the size of the problem or computational efforts required to accurately simulate protein folding, the number of numerical operations is counted. This number scales with the amount of particles, if complexity of interaction is not considered. Hence, when individual water molecules are considered in the matter description, then for the realistic system size simulations the number of operations is enormous.

On the other extreme the size of the experimental system is regarded as the large or macroscale. Large scales are normally used for the engineering purposes and can be in length of more than a meter. A range of scales between the micro- and marco- scale is known as the mesoscale.

In general, large systems are simulated using empirical models, such as Navier -Stokes conservation equations or Hydrodynamics [14]. This model proved to be effective for the vast majority of engineering problems, although in some cases, when complexity of the processes in the system is critical, results are rather mixed. Unfortunately, this method is not applicable for the protein folding study due to the lack of the information on how the microstructure influence macroscale behaviour of the system and vice versa. Although, an effort was made by Irving and Kirkwood to overcome this limitation. They derived equations of hydrodynamics from the principles of the classical statistical mechanics. That resulted in an accurate representation of the macroscopic parameters in terms of molecular variables [15]. However, this approach did not reduce computation costs and lacks influence of the large scales on the small scales.

On the other hand, hydrodynamics, despite the fact that it cannot resolve microscopic details was successfully implemented in some practical experiments.

As we noted before the environment around the protein is critical for the folding process.

For instance, Brody et.al. [16] used a micromixer to move protein in and out of a free-stream flow in a microchamber, where the concentration of denaturant was changing rapidly, that eventually forced protein to fold and unfold. Similar set-ups were studied computationally by [17], where the microchannel was composed of two inlets and one outlet. They have studied membrane fabrication by controlled shear stress and an interfacial cross-linking reaction between the two streams of the fluid.

Unfortunately, these types of simulations are limited by the coarse hydrodynamics methods.

Other extreme can be considered, such as quantum many-body theory, which is assumed to be the true first principle [18]. This approach does not have any empirical parameters to fit and focuses on obtaining the wave functions, that posses all information about the system. The problem here is that independent variables are as many as the number of electrons and nuclei in the system. Consequently, it is an impossible task to simulate large systems. After all, the wave function contains too much information, that in most cases is not needed. In practice there are simplifications, which reduce computational costs, however, for the large size systems they still remain ineffective.

No individual technique applicable to the large or small scales is able to resolve protein folding in the real size system with feasible computation effort. However, such large systems can be solved if multiscale approaches are used. The multiscale means that it considers simultaneously both small and large scales. These approaches preserve the size of the system, although the complexity of the system is simplified by approximations where details are not of great interest. Although, in many cases structure and shape of water molecules are important.

If studied process is described at a particular scale, large or small, the relevant method is used. However, understanding the relationship between the different levels of physical models is not a trivial task and it is essential to connect both representation.

Multiscale methods are based on two ideas. First, the large system can be characterized by models of different complexity. Second, the use of accurate methods in regions, where details are needed, such as regions where defects, chemical reactions, etc. are present. The rest is simulated with the coarse methods (large scales), which normally are cheaper.

Here, multiscale methods are classified into two groups: analytical methods and computational methods. Some of these methods are discussed in the following sections.

1.1 Analytical methods

1.1.1 Matched asymptotics method

Method of ‘matched asymptotics’ is commonly used when solution changes abruptly in a small region, such as boundary layers. This localized region is called ‘inner region’. Dominant features of the ‘inner region’ are different from the feature of the rest region, that is called ‘outer region’. In order to estimate the solution in the ‘inner region’ a stretched variable is introduced [19].

Considerations above can be illustrated using the one-dimensional advection-diffusion equation

$$\partial_t\xi^\varepsilon+\partial_x\xi^\varepsilon=\varepsilon\partial_x^2\xi^\varepsilon, \tag{1.1}$$

where $\xi^\varepsilon(x,t)$ is a physical quantity, t denotes time, x is the spatial coordinate, $\varepsilon \to 0$ in general represents the small scales (i.e region where details are of great interest, for instance cooling of the hot wall by the flow of cool liquid, where cooling is dominated by the diffusion in the boundary layer).

The initial condition is not important for the method description, while the boundary conditions are essential and given by $\xi^\varepsilon(0,t)=\xi_0(t)$ and $\xi^\varepsilon(1,t)=\xi_1(t)$.

Due to the small value of ε the right hand side can be neglected yielding an advection equation

$$\partial_t\Xi+\partial_x\Xi=0, \tag{1.2}$$

which is not exactly the same as the original equation. The solution of the advection equation Ξ is denoted as the 'outer solution' and requires one boundary condition $\Xi|_{x=0}=\xi_0^\varepsilon$, again the initial conditions are not of great importance for the demonstration of the method.

An assumption is made that abrupt change of the solution appears at the boundary layer at $x \to 1$, although the boundary layer is not accounted in the solution of the advection equation (1.2). The boundary layer can be used to connect solution of the advection equation (1.2) with the solution of the initial problem (1.1) [20].

According to the 'matched asymptotics' method a stretching variable is introduced

$$y=\frac{x-1}{\delta}, \tag{1.3}$$

where δ is known as a boundary layer thickness.

Now the initial differential equation (1.1) can be expressed in terms of the stretching variable

$$\partial_t\tilde{\xi}^\varepsilon+\frac{1}{\delta}\partial_y\tilde{\xi}^\varepsilon=\frac{\varepsilon}{\delta^2}\varepsilon\partial_y^2\tilde{\xi}^\varepsilon. \tag{1.4}$$

This equation gives non-trivial balance, when δ and ε are close and for the current demonstration are assumed to be equal. This yields the following differential equation

$$\partial_y\tilde{\xi}=\partial_y^2\tilde{\xi}, \tag{1.5}$$

where $\tilde{\xi}$ is the solution in the boundary layer. Derivative with respect to time can be neglected, since $\delta\cdot\partial_t\tilde{\xi}$ is small. Integrating once the equation above gives

$$\tilde{\xi}=\partial_y\tilde{\xi}+C_1, \tag{1.6}$$

in order to match the solution with the 'outer region' we assume that $\partial_y\tilde{\xi}|_{y\to-\infty}=0$, hence $C_1=\Xi(1,t)$. The second boundary condition is $\tilde{\xi}|_{y=0}=\xi_1(t)$. Integrating again and expressing in terms of the initial variable x, the boundary layer solution is given by

$$\tilde{\xi}(x,t) = \Xi(1,t) + (\xi_1(t) - \Xi(1,t))e^{\frac{x-1}{\delta}}. \tag{1.7}$$

In this particular case, 'matched asymptotics' method allows to connect large system Ξ description with the boundary layer $x \to 1$, which is regarded as the small scales description (region). This method can be effectively applied to the boundary layer problems and internal vortices.

Apart from this technique other analytical approaches are available, such as averaging methods, multiscale expansions, etc [20].

1.1.2 Multiscale expansion method

A brief review of the method is given here, more details can be found in [20].

The multiscale expansion method employs the expansion of the solution and it is used for the ordinary differential equations (ODE), that contain small parameter ε. Thus, method can be applied to systems with disparate scales. The solution is assumed to be given by

$$\xi(t) \approx \xi_0(t) + \varepsilon\xi_1(t) + \varepsilon^2\xi_2(t), \tag{1.8}$$

which is later substituted back in the initial differential equation.

The objective is to find ξ_0, ξ_1. Effectively, the consequent solution of ξ_1 substituted back into the expansion will account for the effect of the small contribution $\varepsilon\xi_1(t)$ in (1.8).

1.1.3 Dimensional analysis

In engineering 'dimensional analysis' is commonly used, which can be very useful for a quick guess of important features. It allows to identify the relationships between the different physical quantities by analysing their dimensions. In order to do that Buckingham π theorem is used [21]. The most remarkable example is Kolmogorov's prediction about the small scale structures in a fully developed turbulent flows [22].

In general, analytical techniques are limited to a set of problems they can be applied to, mostly in Hydrodynamics. Unfortunately, molecular phenomena, such as protein folding, cannot be effectively investigated using these methods. For this purpose computational methods are employed.

1.2 Computational methods

Computational methods are usually applied to Partial Differential Equations (PDE). These methods employ various numerical techniques in order to obtain solution that is very close to the exact one.

A standard procedure for numerical methods is as follows:

1. Discretize PDE using, for example, finite differences or finite element methods [23], that are popular in Hydrodynamics. In matrix form discretized PDE can be expressed as

$$A_h \xi_h = f_h, \tag{1.9}$$

where h denotes the grid size.

2. Solve obtained linear system using iterative methods, that generate a sequence of improving approximate solutions [24].

The iterative method convergence is determined by the condition number of matrix A_h. Usually, this condition number scales as $k(A_h) \approx h^{-2}$. Thus, for smaller h the convergence is slower [24].

1.2.1 Multigrid methods

One of the computational mutiscale methods is ‘multigrid method’, which became a practical tool in 70s, and was later extended to Molecular Dynamics and Monte Carlo simulations [25]. In particular, Brandtl suggested to use this tool for the study of the marcoscale behaviour of multiphysics problems [26].

This method can be demonstrated if Poisson’s equation is considered

$$\Delta\xi(x) = f(x) \tag{1.10}$$

with the boundary condition $\xi|_{\partial\Omega} = 0$, where $\partial\Omega$ is a contour of the whole simulation domain Ω, here initial conditions are not important for the demonstration of the method. Apply finite differences framework to (1.10) and consider an iterative method, for instance the relaxation method (see Appendix A.1), on two different grids that correspond to the grid sizes h (fine grid) and $2h$ (coarse grid). Here the fine grid represents the small scales, while the coarse grid the large scales.

In order to transfer the solution between the grids, projection operator is introduced, which maps fine grid functions on the coarser grids P_h^{2h}. And interpolation operator, which maps coarser grid functions on the finer grids P_{2h}^h.

The algorithm of multigrid method can be demonstrated as the following procedure:

1. Run a few steps (iterations) on the fine grid using, for instance the relaxation method [27].

2. Calculate the residual on the fine grid $r_h = A_h\xi_h - f_h$.

3. Project residual to the coarse grid $r_{2h} = P_{h2}^h r_h$.

4. Solve on the coarse grid $A_{2h}e_{2h} = r_{2h}$, where $e_{2h} = \xi_{2h} - \xi^*$ is the error vector and ξ^* is the exact solution of (1.10).

5. Interpolate to the fine grid $\xi_h \leftarrow \xi_h - P_h^{2h} e_{2h}$.

This method can be generalized to any subsequent grid sizes, covering all scales. However, multigrid method requires sufficient computational effort and does not have the best accuracy.

Many other classic iterative algorithms are available, such as the fast multipole method, adaptive mesh refinement, multi-resolution representation, or domain decomposition [20].

1.2.2 Domain decomposition methods

The domain decomposition method also employs various grids, although the implementation is different. The whole simulation domain is divided into subdomains and the strategy is to match the solutions in different subdomains.

The advantages of this method are:

1. convenience to use in parallel computing;
2. different models or different algorithms can be used in each subdomain [28].

The solution of the first subdomain is denoted as ξ_1 and the second as ξ_2, while the solution on the interface of these two subdomains as ϕ Fig. 1.1.

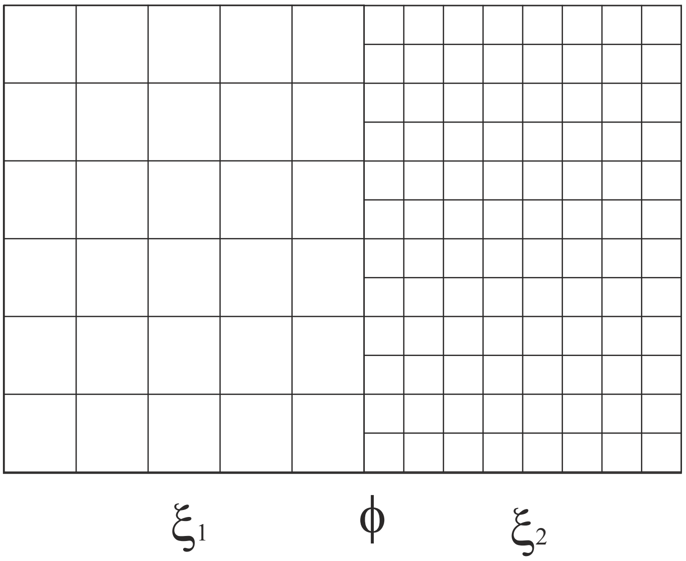

Figure 1.1: Domain decomposition method for two non-overlapping different grids. The solution of the first subdomain is denoted as ξ_1 and the second as ξ_2, while the solution on the interface of these two subdomains as ϕ

Equation (1.10) can be rewritten as a linear system if finite differences are used

$$A\xi = f, \tag{1.11}$$

where $\xi = (\xi_1, \xi_2, \phi)^T$, A and f are relevant matrices, the subscript h, which corresponds to the grid size is omitted. The linear system can be expanded in

$$\begin{pmatrix} A_{11} & 0 & A_{13} \\ 0 & A_{22} & A_{23} \\ A_{31} & A_{32} & A_{33} \end{pmatrix} \begin{pmatrix} \xi_1 \\ \xi_2 \\ \phi \end{pmatrix} = \begin{pmatrix} f_1 \\ f_2 \\ f_\phi \end{pmatrix}.$$

When ξ_1 and ξ_2 are eliminated, the solution at the interface between subdomains is given by

$$S\phi = g, \tag{1.12}$$

where $g = f_\phi - A_{31}A_{11}^{-1}f_1 - A_{32}A_{22}^{-1}f_2$ and $S = A_{33} - A_{31}A_{11}^{-1}A_{13} - A_{32}A_{22}^{-1}A_{23}$.

The solution at the interface can be written in the following way

$$S\phi = A_{33} - A_{31}\xi_1 - A_{32}\xi_2, \tag{1.13}$$

where the two equations $A_{11}\xi_1 = A_{13}\phi$ and $A_{22}\xi_2 = A_{23}\phi$ are solved independently, and g is treated in the same manner.

Effectively, the solution for the original problem is obtained, when normal derivatives as well as the solutions between the subdomains match at the interface [20].

Finally, the subdomains can be either overlapping or not. However, if subdomains overlap, the boundary conditions must be chosen correctly, otherwise the method may not converge. More information about the decomposition methods can be found in [28].

1.2.3 Adaptive resolution methods

It is assumed that there are two different representations of the matter. Fritsch et al. [2], generalized the adaptive resolution idea, where molecules smoothly changed their level of representation as a function of position by moving through a transition region Fig. 1.2.

Figure 1.2: Pictorial representation of the adaptive simulation box and local molecular representation. The low resolution (coarse-grained) region is on the right, indicated by B, and the high resolution (atomistic) region A is on the left. The transition (hybrid) region H with the switching function $w(x)$ (curve in grey) is in the middle; The figure is taken from [2]

The transition is accomplished by changing the degrees of freedom of the molecules, such that the tetrahedral particles are gradually introduced. Their corresponding spheres are denoted as coarse grained description. These tetrahedral particles are build of four molecules bound by the Lennard-Jones interaction potential type springs. When molecules are passing to the coarse grained region, they are gradually loosing their degrees of freedom (DOF), such as rotational and vibrational ones, until they become spheres with only translational DOFs of the centre of mass [2].

This transition process is described by two different representations, that are interpolated by a function $w(x)$, with $w = 1$ in fine-grained (small scales) region, and $w = 0$ in the coarse-grained region (large scales).

The fine grained region is described by individual water molecules. While the coarse grain region is described by the coarse grained spheres, which interact with each other through central forces.

Hence, in the transition region, the total force between interacting particles α and β located at the X_α and X_β respectively consists of two parts $\Xi_{tot} = \Xi^A_{\alpha\beta} + \Xi^B_{\alpha\beta}$, the all atom interaction given by

$$\Xi^A_{\alpha\beta} = w(X_\alpha)w(X_\beta)\sum_{ij}\vec{F}^A_{\alpha_i\beta_j} \tag{1.14}$$

and the coarse grain contribution

$$\Xi^B_{\alpha\beta} = (1 - w(X_\alpha)w(X_\beta))\vec{F}^B_{\alpha\beta}, \tag{1.15}$$

where A denotes the fine grained, B the coarse grained representation, $\vec{F}^A_{\alpha_i,\beta_j}$ is the interaction force between i atom of molecule α and j atom of β molecule, and $\vec{F}^B_{\alpha\beta}$ is the mass- centre of mass interaction.

In this case unphysical drift due to the pressure difference at the boundaries of the transition region can arise, hence, the authors removed it by introducing a thermodynamics force, which acts on the molecules

$$F_{th}(x) = \frac{M_\alpha}{\rho_0}\nabla p(x), \tag{1.16}$$

where ρ_0 is all-atom density, M_α is molecule's mass and p is pressure. This force is able to adjust the viral pressure and the thermal energy, while the molecules are passing from one region to another.

As a result, the thermodynamic force, (1.16), eliminated the effects of the pressure difference on the distribution of molecules in both regions as well as artifacts (large density fluctuations) that appeared due to the change of the resolution.

1.2.4 Dissipative Particle Dynamics

Other popular technique, which was introduced by Hoogerbrugge and Koelman, is the so called Dissipative Particle Dynamics (DPD) [29], which allows to relate the macroscopic properties of the fluid to its microscopic structure.

DPD is an off-lattice method, where particles represent whole molecules or fluid regions. This method does not consider atomistic details, thus, the main benefit of DPD is that it allows to use longer time and length scales, than the conventional MD method. Today it has become a popular tool for modelling complex systems [30, 31].

Summarizing, computational methods presented here demonstrate an effort to account for the microstructure influence on the macroscale behaviour of the system and vice versa. However, accuracy of these methods and effectiveness in providing desired results is rather mixed.

1.2.5 Hybrid Molecular Dynamics and Hydrodynamics methods

In the hybrid Molecular Dynamic and Hydrodynamics simulation, the domain is decomposed into the meso- and micro- scale subdomains joined by a hybrid interface. Based on the flux balance, at every fixed time interval both domains receive equal but opposite mass and momentum fluxes across the hybrid interface.

The earliest examples of this type of method includes [32, 33], followed by more recent work, namely, [34, 35, 36, 37].

Fabritis et. al [38] showed that the mean values and the fluctuations across the interface are consistent with hydrodynamics and thermodynamics, when mesoscale Landau Lifshitz - Fluctuating Hydrodynamics (LL-FH) is joined with the microscale Molecular Dynamics (MD) description. Both LL-FH and MD techniques are described in the later sections.

The mass flux was calculated from the MD system and the momentum flux was obtained with two different approaches, that showed the same result. The first was based on the velocity gradients next to the interface, for the second, the pressure gradient was used.

Similarly, the information exchange between the domains with different representations can also be accomplished using Schwarz alternating method. For instance, this approach was used by Nie et. al [39] to simulate Couette flow and channel flow with nano-scale rough walls. They split the simulation domain in two subdomains, with the region where both subdomains overlap. In one subdomain the continuum Navier-Stokes equations [14] were solved and in the other Molecular Dynamics was used.

Other authors, [32, 40] also established coupling between MD and hydrodynamics by ensuring the conservation of the mass and momentum fluxes through a finite-size overlap-region. In the overlap-region Schwarz alternating method was applied.

The Schwarz method is an iterative method, which approximates the solutions for each subdomain as the boundary conditions. In other words, in the region where two subdomains are connected for one subdomain as a boundary condition is chosen solution of the other subdomain and vice versa [41].

There is a number of efficient approaches developed to couple MD and hydrodynamics, that employ the Schwarz technique [42, 43].

In the recent years there were successful attempts to implement the multiscale models, from modelling micro and nanofluidic devices to physical, chemical, biological and other objects [44, 45, 46, 47, 48, 9, 49].

The main limitation in the multiscale methods is the accuracy of the communication between the two different representations, if the computational effort is not considered. So far, the methods presented here do not maintain the communication without approximations, or introduction of fictitious potentials or molecules.

Thus, a new self-consistent method is proposed, which solves the communication problems between the two different descriptions without artificial approximations and leads to a smooth transition between them.

1.3 The main idea of our approach

In the present work **coupling method** or **coupling** denotes a method, which is able to communicate the large and small scales, provides an information exchange between the disparate scales.

We assume that matter is described by a mixture of two different phases.

The first phase is represented using Molecular Dynamics simulations and the other by Landau Lifshitz- Fluctuating Hydrodynamics simulation. Both these techniques are discussed in details in Chapter 2.

The description of the matter changes gradually from the region where mostly large scales are present Fig. 1.3 (left hand side), to the region where mostly small scales are present (right hand side).

In the transition or overlap-region a mixture of these two representations is considered. The communication or information exchange between them is conducted using coupling methods investigated in this work. A multiphase modelling concept is used to couple both scales in the overlap-region. In the current implementation, large and small scales coexist with the different concentrations s. On the right hand side of the domain Fig. 1.3 concentration of the large scales is zero, that means that only the small scales are accounted. The large scales are also present in this region, however, they are not visible by the small scales.

On the left hand side Fig. 1.3 it is assumed, that only the large scales are present, although there still exist small scales that are not visible by the large scales.

In other words, the large and small scales are present in the simulation domain simultaneously,

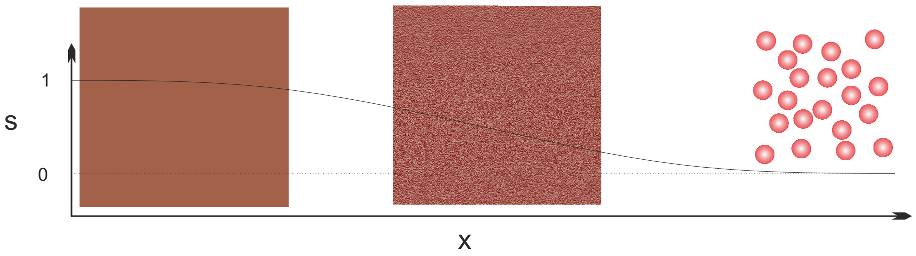

Figure 1.3: The visibility of matter description is controlled by the parameter s. If $s = 1$ the matter is fully described by continuum phase, in the transition zone $0 < s < 1$ matter is represented by a mixture of both continuum and atomistic descriptions, if $s = 0$ fully atomistic description is considered

however, the contribution of each scale to the matter description changes with the concentration s, that is a priori known for the whole system.

The presence of the two descriptions all over the simulation domain maintains the continuity and the conservation in the Molecular Dynamics and Landau Lifshitz - Fluctuating Hydrodynamics simulations.

1.4 Thesis outline

In the present work we demonstrate a self-consistent communication between the large and small scales. We also show that dynamical properties are different in the regions with various concentrations of the phases. While structural properties, such as the close order of the liquid do not change.

Second chapter is devoted to the development of the coupling method as well as the study of two-dimensional liquid argon in the framework of proposed coupling method. The analysis of close order, dynamics and statistical properties is undertaken. The analysis confirmed that the communication between the large and the small scales was successfully established.

Third chapter is focused on two-dimensional ‘Mercedes Benz’ or BN2D [50] and SPC/E [51] water models implementation in the context of the coupling method.

We start with the study of BN2D water model. Where for the first time we derived formulas for the thermodynamic properties of the model when microcanonical (NVE) ensemble is used. Also we derived the equations of motion for the BN2D water model for isothermal-isobaric (NPT) ensemble and discussed the rotational degree of freedom representation in both NVE and NPT ensembles.

Then we report recent developments of the coupling method, especially its integration into the well known software GROMACS [52] by our collaborating colleagues from Cambridge University and Queen Mary University of London.

The development of the coupling method was split into two stages: ‘one way’ and ‘two way’ communications between the scales. Where in the first, the small scales are affected by the large scales and in the second both scales affect each other. Currently, only the ‘one way’ communication is integrated into the GROMACS as add-on.

And finally, a three-dimensional liquid argon as well as SPC/E water models were simulated using this add-on, which provided the same trends as were obtained for the simpler BN2D water model.

Also we discuss and demonstrate the effect of the advanced mapping technique form the small scales to the large scales (‘blob’ filter) [1] in the context of our coupling method.

2

Bridging large and small scales

CONTENTS

2.1 Conservation equations **29**
  2.1.1 Mass conservation 31
  2.1.2 Momentum conservation 34
  2.1.3 Energy conservation 36
2.2 Implementation **37**
  2.2.1 MD simulation 37
  2.2.2 Landau Lifshitz-Fluctuating Hydrodynamics 40
  2.2.3 Interpolation in between the scales 42
  2.2.4 Communicating large and small scales 43
2.3 ‘One way’ coupling **45**
  2.3.1 FH phase 45
  2.3.2 LL-FH simulation 46
  2.3.3 MD phase 48
  2.3.4 MD simulation 49
  2.3.5 Stability analysis 52
  2.3.6 Structure and Dynamics of the liquid 59
2.4 ‘Two way’ coupling **60**
  2.4.1 FH phase 62
  2.4.2 MD phase 63
  2.4.3 Simulation 64
  2.4.4 Stability analysis 64
  2.4.5 Structure and Dynamics of the liquid 70
2.5 Total energy rescaling **72**
  2.5.1 Implementation 74
2.6 Conclusions **77**

2.1 Conservation equations

In the introduction the importance of a realistic size simulation of biological objects was emphasised. As we noted, an effective simulation, that involves concurrent continuum and atomistic descriptions of matter, is a challenging task. That in most cases ends with the approximations and simplifications of the matter or processes studied. Sometimes surrounding conditions can be idealized in order to reduce the computation costs, for instance biological objects are considered with the surrounding medium at rest, that is not true in a real experiment.

We also noted, that a well known methods of Computational Fluid Dynamics (CFD), such as Navier-Stokes equations proved to be effective for the vast majority of the flow problems, although they lack accuracy, when atomistic resolution is needed. Thus, an effort is made to tailor CFD methods to the atomistic description. For instance, mesoscale method proposed by Landau and Lifshitz, entails atomistic scale fluctuations in the hydrodynamics equations. This extension was substantial despite the fact, that the communication between the continuum and atomistic scales is incomplete, since changes in the continuum do not affect the atomistic processes (small scales).

On the other hand, the whole system can be considered at atomistic level, for instance Molecular Dynamics can be used to describe medium in which biological objects are immersed. Unfortunately, the demand for the computational resources in this case cannot be satisfied.

Nevertheless, large biological systems were under scrutiny of scientists for many years, but only in the last few decades this area of research had achieved certain success.

Nowadays, accurate simulation of the large systems, such as virus in the water is not possible, regardless the increasing computing power. Efficiently, this means that the methods that are able to resolve the physical phenomena over a wide range of scales and reduce the computational costs for the complex systems simulations are not accurate enough.

The approximations made often reduce accuracy of the simulation of the phenomena studied. For example in the case of DPD method unphysical potentials are introduced between conglomerates of molecules. In some cases artificial boundaries (Schwartz alternating method) appear in the regions where the large and small scales are present (so called overlap-region), that results in unnatural behaviour. An approach that doesn't have these drawbacks would be beneficial.

A coupling method studied here does not introduce fictitious boundaries and treats overlap-region as a mixture of two miscible liquids. In other words, following the standard approach in two-phase modelling, a mixture of two completely miscible liquids in the system [53] is considered. One phase corresponds to the Lagrangian phase (atomistic description) and the other is the Eulerian phase (FH continuum).

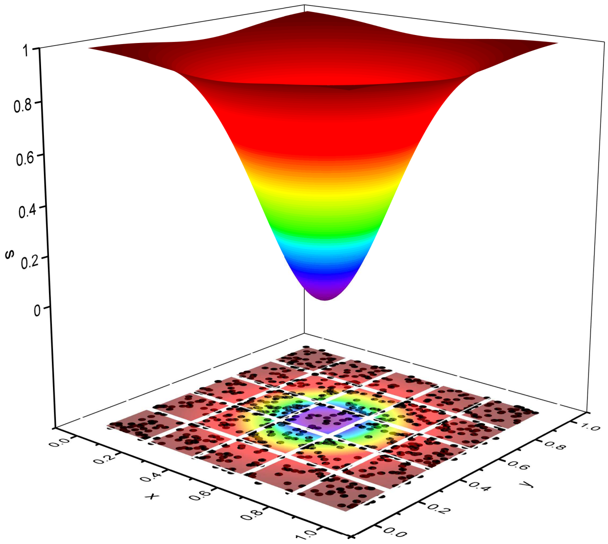

Figure 2.1: In the xy-plane a 2D simulation domain is shown, with the black dots representing MD particles; the FH phase is modelled on a regular grid (white lines); the coupling parameter s has a Gaussian profile in this example and its projection on the xy-plane is shown in colour

For simplicity and associativity reasons the Lagrangian phase is denoted as the MD phase and the Eulerian phase as the FH phase, due to the methods used to obtain properties, such as densities and momentum, for each phase. Effectively it means Molecular Dynamics is used for the MD phase and Landau Lifshitz- Fluctuating Hydrodynamics for the FH phase.

This multiphase approach, together with the MD and LL-FH frameworks allows to establish communication between these phases in the overlap-region. Here communication is considered as an inheritance of the large scale (FH phase) properties by the small scales (MD phase) and vice versa. The strength of this inheritance is estimated by the concentration of the phases and implemented though a set of parameters as well as imbalance between the phase densities and momenta. Furthermore, the coupling method allows to exchange mass and momentum between the phases, such that the differences between them are driven to a prescribed value.

A parameter s is reintroduced, which represents the concentration of the FH phase. This parameter shows if the mixture properties are dominated by one phase or another. In mathematical terms, s is a smoothly changing function in space (and possibly time). The value of s varies from 0 to 1, as shown in Fig. 2.1. We assume that the centre of the system has mostly MD description ($s \approx 0$) and on the edges it is mostly FH ($s \approx 1$), while in the middle region there is a mixture of the MD and FH phases.

In general, the MD phase is a continuum entity, which consists of many MD particles. For this reason all simulation domain is split into subdomains (cells) Fig. 2.1, as it is commonly done for the LL-FH simulation. Further, each cell has prescribed parameters, such as density and velocity (momentum), that are obtained differently for each phase. For the FH phase these parameters are evaluated using the conservation equations, while for the MD phase MD particles and their velocities are counted in each cell.

This provides us with the MD phase density $\sum_p \rho_p$ and momentum $\sum_p \rho_p u_{ip}$, in which $\rho_p = \frac{m_p}{V_{cell}}$ and u_{ip} are MD particle's density and velocity respectively, where p stands for the 'particle', i denotes the spatial component (x, y or z), m_p is the particle's mass, and V_{cell} is the volume of the subdomain (cell) over which summation $\sum_p$ is performed. The obtained values are prescribed to the cells centres, in which the particles were summed. The FH phase density ρ and momentum ρu_i are defined for the same cell centres as the MD phase density and momentum.

According to the multiphase approach, density of the MD and FH phase mixture is given by

$$\tilde{\rho} = s\rho + (1-s)\sum_p \rho_p \tag{2.1}$$

and the momentum is expressed as

$$\tilde{u}_i\tilde{\rho} = su_i\rho + (1-s)\sum_p \rho_p u_{ip}. \tag{2.2}$$

The equations above indicate that at the limits, when $s \to 0$ density and momentum of the mixture are determined by the MD phase, and, contrary, when $s \to 1$ the mixture properties are specified by the FH phase.

The phase conservation equations are obtained, if the following philosophy is followed:

- mass is conserved;
- Newton's second law is applied (momentum conservation);
- energy is conserved.

The following definitions from CFD are used: $control\ volume$ is a closed volume drawn within a finite region of the flow, it is a reasonably large and finite region of the flow; $control\ surface$ is a surface of the $control\ volume$ [54].

In the following sections, fundamental physical principles listed above are applied to the fluid crossing the control volume's surface and to the fluid inside the control volume.

2.1.1 Mass conservation

As was noted in the previous section a model of a finite control volume fixed in space is considered. A vector $\vec{u}$ denotes the velocity on the control surface, where vector elemental surface area is $d\vec{S}$. Let dV be an elemental volume inside the finite control volume.

The mass conservation principle is applied to this control volume, that means 'net mass flow out of the control volume through the surface S' is equal to the 'time rate of decrease of mass inside the control volume'. Then, the mass conservation for the mixture, with density $\tilde{\rho}$ is given by the expression:

$$\frac{\partial\tilde{\rho}}{\partial t}+\frac{\partial}{\partial x_i}(\tilde{u}_i\tilde{\rho})=0, \tag{2.3}$$

where i denotes the spatial component (x, y or z) and the derivative with respect to the coordinate $\frac{\partial}{\partial x_i}=\left(\frac{\partial}{\partial x},\frac{\partial}{\partial y},\frac{\partial}{\partial z}\right)$.

An assumption is made that the phases are able to convert from one to another, such that the total mass of the mixture is constant. The same assumption is applicable to momentum.

The mass conservation equation of the mixture is not of a great importance, although it can be used to extract mass conservation equations of the phases.

Equation (2.3) can be decoupled in the mass conservation laws of each phase. For example, the FH phase mass conservation equation is given by

$$\frac{\partial}{\partial t}s\rho+\frac{\partial}{\partial x_i}\tilde{u}_i s\rho=J^{\rho}, \tag{2.4}$$

and the MD phase mass conservation equation can be written as

$$\frac{\partial}{\partial t}(1-s)\sum_p\rho_p+\frac{\partial}{\partial x_i}(1-s)\sum_p u_{ip}\rho_p=-J^{\rho}, \tag{2.5}$$

where J^{ρ} is a phase mass sink/source, here the transport velocity of the FH phase is replaced by the conservation velocity of a mixture $\tilde{u}_i$ in order to produce well-defined equations of motion. Thus, (2.3) is not entirely correct and following derivations will be based on the (2.4) and (2.5).

Throughout this work coupling method implies that imbalance between the FH and MD phase is driven to a particular value. In the case of mass it can be specified in the following manner

$$\frac{D}{Dt_0}\left(\tilde{\rho}-\sum_p\rho_p\right)=L^{\rho}\cdot\left(\tilde{\rho}-\sum_p\rho_p\right), \tag{2.6}$$

where $\frac{D}{Dt_0}=\frac{\partial}{\partial t}\cdot+\frac{\partial}{\partial x_i}\tilde{u}_i\cdot$, the L^{ρ} operator drives the corresponding deviation to the prescribed value within the zone $0<s<1$ and returns zero at the $s=0$ and $s=1$.

This assumption or dynamic law provides an ability to adjust the density of the MD phase $\sum_p\rho$ to the density of the mixture $\tilde{\rho}$. The nature of the L^{ρ} operator is a matter of preferences/ convenience and will be discussed in the Section 2.3 and Section 2.4).

First, the FH phase contribution to the mass conservation is estimated.

Using the notation of the D/Dt_0, (2.6) can be expanded to

$$\frac{\partial}{\partial t}\left(\tilde{\rho}-\sum_p\rho_p\right)+\frac{\partial}{\partial x_i}\tilde{u}_i\left(\tilde{\rho}-\sum_p\rho_p\right)=L^{\rho}\cdot\left(\tilde{\rho}-\sum_p\rho_p\right), \tag{2.7}$$

if $\tilde{\rho}$ from the (2.1) is substituted in the (2.7), then dynamical law, (2.6), can be expressed as

$$\frac{\partial}{\partial t}s\left(\rho-\sum_p\rho_p\right)+\frac{\partial}{\partial x_i}\tilde{u}_i s\left(\rho-\sum_p\rho_p\right)=L^{\rho}\cdot\left(\tilde{\rho}-\sum_p\rho_p\right). \tag{2.8}$$

Equation (2.8) together with the FH phase mass conservation, (2.4), yields the mass sink/source equal to

$$J^{\rho} = \frac{\partial}{\partial t} s \sum_p \rho_p + \frac{\partial}{\partial x_i} \tilde{u}_i s \sum_p \rho_p + L^{\rho} \cdot \left(\tilde{\rho} - \sum_p \rho_p \right), \tag{2.9}$$

we keep $\tilde{\rho}$ on the right hand side in order to obtain modified equations of motion, that contain the mixture ('tilde') and MD variables.

Once J^{ρ} is known, the FH phase mass conservation (2.4) can be used.

Secondly, the MD phase contribution to the mass conservation is estimated. The mass sink/source J^{ρ} can be substituted in the MD phase mass conservation (2.5) that gives the following relationship

$$\frac{\partial}{\partial t}(1-s) \sum_p \rho_p + \frac{\partial}{\partial x_i}(1-s) \sum_p \rho_p u_{ip} = -\frac{\partial}{\partial t} s \sum_p \rho_p - \frac{\partial}{\partial x_i} \tilde{u}_i s \sum_p \rho_p - L^{\rho} \cdot \left(\tilde{\rho} - \sum_p \rho_p \right),$$

which can be reordered to

$$\frac{\partial}{\partial t} \sum_p \rho_p + \frac{\partial}{\partial x_i} s \tilde{u}_i \sum_p \rho_p + \frac{\partial}{\partial x_i}(1-s) \sum_p \rho_p u_{ip} = -L^{\rho} \cdot \left(\tilde{\rho} - \sum_p \rho_p \right). \tag{2.10}$$

The mass conservation equation of the MD phase must be considered in the context of Molecular Dynamics simulation. For this purpose it is convenient to use the mass conservation equation in the following form

$$\frac{\partial}{\partial t} \sum_p \rho_p + \frac{\partial}{\partial x_i} \sum_p \frac{dx_{ip}}{dt} \rho_p = 0, \tag{2.11}$$

where the modified velocities $\frac{dx_{ip}}{dt}$ of the MD particles are introduced. These velocities include the mass source/sink J^{ρ}.

Equation (2.10) together with (2.11) give

$$\frac{\partial}{\partial x_i} \sum_p \frac{dx_{ip}}{dt} \rho_p = \frac{\partial}{\partial x_i} \tilde{u}_i \sum_p \rho_p + \frac{\partial}{\partial x_i}(1-s) \sum_p \rho_p u_{ip} + L^{\rho} \cdot \left(\tilde{\rho} - \sum_p \rho_p \right), \tag{2.12}$$

that is further integrated yielding the mass conservation equation of the MD phase, that is applied to the entire cell

$$\sum_p \frac{dx_{ip}}{dt} \rho_p = \tilde{u}_i \sum_p \rho_p + (1-s) \sum_p \rho_p u_{ip} + \int L^{\rho} \cdot \left(\tilde{\rho} - \sum_p \rho_p \right) dx.$$

From the equation above the single particle velocity can be derived by eliminating the summation

$$\frac{dx_{ip}}{dt} = u_{ip} + s(\tilde{u}_i - u_{ip}) + \frac{1}{\rho_p N(t)} \int L^{\rho} \cdot \left(\tilde{\rho} - \sum_p \rho_p \right) dx, \tag{2.13}$$

where $N(t)$ is the number of particles in the cell.

As a result, new MD particles velocities/coordinates, (2.13), were obtained. The mass source/sink J^{ρ} defined in (2.9) is used in the mass conservation equation for the FH phase (2.4). This set of equations ensures that the total mass of the mixture is conserved.

2.1.2 Momentum conservation

In addition to the conservation of mass, it is appropriate to assume that the momentum is also conserved.

Thus, another fundamental physical principle is applied to the control volume, that is the Newton's second law

$$\vec{F} = m\vec{a}, \tag{2.14}$$

where the net force $\vec{F}$ is proportional to the acceleration $\vec{a}$. It is assumed that the control volume is exposed to the surface forces, while the body forces are set to zero for convenience.

These assumptions lead to the momentum conservation equation of the mixture, that is consequently decoupled into the FH phase momentum conservation equation

$$\frac{\partial}{\partial t} s\rho u_j + \frac{\partial}{\partial x_i} \tilde{u}_i u_j s\rho = sF_j + J^u, \tag{2.15}$$

and the MD phase momentum conservation equation

$$\frac{\partial}{\partial t}(1-s)\sum_p \rho_p u_{jp} + \frac{\partial}{\partial x_i}(1-s)\sum_p u_{ip} u_{jp} \rho_p = \frac{(1-s)}{V_{cell}} \sum_p F_{jp} - J^u, \tag{2.16}$$

where F_j is the FH force (per volume), F_{jp} is the MD force and J^u is a momentum exchange rate.

Similar procedure as for the mass conservation equation is used here. That means that the difference between the MD phase and the mixture momentum is driven to a prescribed value. This assumption is expressed as

$$\frac{D}{Dt_0}\left(\tilde{u}_j\tilde{\rho} - \sum_p \rho_p u_{jp}\right) = L^u \cdot \left(\tilde{u}_j\tilde{\rho} - \sum_p \rho_p u_{jp}\right), \tag{2.17}$$

where L^u is the forcing operator, which will be defined in Section 2.3 and Section 2.4 for different coupling approaches (cases).

A procedure similar to the mass sink/source evaluation is applied to the momentum exchange rate, which is later used in the FH phase momentum conservation, (2.15).

Equation (2.17) can be expanded to

$$\frac{\partial}{\partial t}\left(\tilde{u}_j\tilde{\rho} - \sum_p \rho_p u_{jp}\right) + \frac{\partial}{\partial x_i}\tilde{u}_i\left(\tilde{u}_j\tilde{\rho} - \sum_p \rho_p u_{jp}\right) = L^u \cdot \left(\tilde{u}_j\tilde{\rho} - \sum_p \rho_p u_{jp}\right),$$

where $\tilde{u}_i\tilde{\rho}$ is substituted from the (2.2) yielding

$$\frac{\partial}{\partial t} s\left(u_j\rho - \sum_p \rho_p u_{jp}\right) + \frac{\partial}{\partial x_i} s\tilde{u}_i\left(u_j\rho - \sum_p \rho_p u_{jp}\right) = L^u \cdot \left(\tilde{u}_j\tilde{\rho} - \sum_p \rho_p u_{jp}\right),$$

similar to the mass conservation case we keep $\tilde{u}_j\tilde{\rho}$ on the right hand side in order to obtain modified equations of motion, that contain the mixture ('tilde') and MD variables.

The equation above together with the (2.15) gives the momentum exchange rate

$$J^u = \frac{\partial}{\partial t} s \sum_p \rho_p u_{jp} + \frac{\partial}{\partial x_i} s\tilde{u}_i \sum_p \rho_p u_{jp} - sF_j + L^u \cdot \left(\tilde{u}_j \tilde{\rho} - \sum_p \rho_p u_{jp} \right). \tag{2.18}$$

The definition of J^u completes the FH phase momentum conservation (2.15).

Therefore, the momentum exchange rate J^u can be substituted in the MD phase momentum conservation, (2.16), and produce

$$\frac{\partial}{\partial t}(1-s) \sum_p \rho_p u_{jp} + \frac{\partial}{\partial x_i}(1-s) \sum_p u_{ip} u_{jp} \rho_p = \tag{2.19}$$

$$= \frac{(1-s)}{V_{cell}} \sum_p F_{jp} + sF_j - \frac{\partial}{\partial t} s \sum_p \rho_p u_{jp} - \frac{\partial}{\partial x_i} s\tilde{u}_i \sum_p \rho_p u_{jp} - L^u \cdot \left(\tilde{u}_j \tilde{\rho} - \sum_p \rho_p u_{jp} \right),$$

that is further simplified to

$$\frac{\partial}{\partial t} \sum_p \rho_p u_{jp} + \frac{\partial}{\partial x_i}(1-s) \sum_p u_{ip} u_{jp} \rho_p = \tag{2.20}$$

$$= \frac{(1-s)}{V_{cell}} \sum_p F_{jp} + sF_j - \frac{\partial}{\partial x_i} s\tilde{u}_i \sum_p \rho_p u_{jp} - L^u \cdot \left(\tilde{u}_j \tilde{\rho} - \sum_p \rho_p u_{jp} \right).$$

Effectively, the same analogy with the MD phase mass conservation is used for the momentum. It is convenient to use the momentum conservation equation in the following form

$$\frac{\partial}{\partial t} \sum_p \rho_p u_{jp} + \frac{\partial}{\partial x_i} \sum_p \frac{dx_{ip}}{dt} u_{jp} \rho_p = \sum_p \rho_p \frac{du^N_{jp}}{dt}, \tag{2.21}$$

that leads to the modified force of the MD phase $\frac{du^N_{jp}}{dt}$, which includes the momentum exchange rate J^u.

Consequently, a series of rearrangements and substitutions are made to obtain the MD phase forces. Equation (2.21) in combination with (2.20) yield

$$-\frac{\partial}{\partial x_i} \sum_p \frac{dx_{ip}}{dt} u_{jp} \rho_p + \sum_p \rho_p \frac{du^N_{jp}}{dt} + \frac{\partial}{\partial x_i}(1-s) \sum_p u_{ip} u_{jp} \rho_p = \tag{2.22}$$

$$= \frac{(1-s)}{V_{cell}} \sum_p F_{jp} + sF_j - \frac{\partial}{\partial x_i} s\tilde{u}_i \sum_p \rho_p u_{jp} - L^u \cdot \left(\tilde{u}_j \tilde{\rho} - \sum_p \rho_p u_{jp} \right),$$

using (2.12) we can obtain following relationship

$$\frac{\partial}{\partial x_i} \sum_p \frac{dx_{ip}}{dt} u_{jp} \rho_p = \frac{\partial}{\partial x_i} s\tilde{u}_i \sum_p u_{jp} \rho_p + \frac{\partial}{\partial x_i}(1-s) \sum_p u_{jp} \rho_p u_{ip} + L^\rho \cdot \left(\tilde{\rho} - \sum_p \rho_p \right) \frac{\sum_p u_{jp}}{N(t)},$$

the modified force/acceleration acting on the molecules in each cell is

$$\sum_p \rho_p \frac{du^N_{jp}}{dt} = (1-s) \frac{\sum_p F_{jp}}{V_{cell}} + sF_j + L^\rho \cdot \left(\tilde{\rho} - \sum_p \rho_p \right) \frac{\sum_p u_{jp}}{N(t)} - L^u \cdot \left(\tilde{u}_j \tilde{\rho} - \sum_p \rho_p u_{jp} \right).$$

The individual particle's force/acceleration becomes

$$\frac{du_{jp}^{N}}{dt} = (1-s)\frac{F_{jp}}{\rho_p V_{cell}} + \frac{1}{\rho_p N(t)}\left[sF_j + L^{\rho}\cdot\left(\tilde{\rho}-\sum_p \rho_p\right)\frac{\sum_p u_{jp}}{N(t)} - L^{u}\cdot\left(\tilde{u_j}\tilde{\rho}-\sum_p \rho_p u_{jp}\right)\right]. \tag{2.23}$$

The new equations of motion include terms $\tilde{\rho}-\sum_p \rho_p$ and $\tilde{u_j}\tilde{\rho}-\sum_p \rho_p u_{jp}$ that force MD particles to minimize the difference between the density and momentum of the mixture and MD phase.

As a result, a full set of equations of motion is obtained. Where we evaluate MD particles accelerations /velocities using (2.23), that are consistent with the MD phase momentum conservation, (2.16), as well as the FH phase momentum conservation, (2.15), and the momentum exchange rate, (2.18).

2.1.3 Energy conservation

Consistent mass and momentum conservation equations for the FH and MD phases were derived. These conservation equations are similar to the Navier-Stokes equations, since the same fundamental principles were applied.

Notably [55], in the case of liquids at isothermal conditions for which the adiabatic heat ratio approaches unity, the macroscopic conservation laws for mass and momentum are sufficient to consider, because the energy equation decouples from the governing Navier-Stokes equations.

However, for the non-equilibrium simulations the total energy control method can be considered. The effect of this method is demonstrated in Section 2.5. Which also showed that the balance of the total energy between both phases is consistent for all concentrations s.

Summarising, we have derived the conservation equations for both phases alongside with the equations of motion for the MD particles, (2.13) and (2.23). The conservation equations are used only for the FH phase. Thus, the FH phase is determined using (2.4) and (2.15), where the mass source/sink J^{ρ} is defined as (2.9) and the momentum exchange rate J^{u}, (2.18). The operators L^{ρ} and L^{u} will be defined in Section 2.3 and Section 2.4 for different coupling approaches (cases).

Originally, the FH force (per volume) F_j, according to the Navier-Stokes equations, is defined as a gradient of the stress tensor. However, in this work, a Landau Lifshitz - Fluctuating Hydrodynamics framework is used. Which extends the applicability range of the Navier-Stokes equations to smaller scales. Practically it means that the stochastic stress tensor is used additionally to the normal stress tensor. The details and implementation of the LL-FH framework together with the derived equations is discussed in the following sections.

2.2 Implementation

2.2.1 MD simulation

The first principles in the present work are shifted from the quantum N-body (QM) to Molecular Dynamics framework. This is due to the complexity of mathematics involved in QM for the large systems and over detailed solution. Molecular Dynamics can be assumed as the most likely method and accurate enough to study atomistic processes.

Here the basics of MD simulation are explained, for practical simulations more advanced techniques are commonly used.

As it was noted before, the MD phase is obtained using new equations of motion, (2.13) and (2.23), in the Molecular Dynamics framework. In other words, physical movements of MD particles are simulated in the context of N-body system using newly derived equations of motion. These MD particles interact for a certain period of time and the path of the particles (trajectory) is determined by the numerical solution of (2.13) and (2.23).

Usually the interaction force $\vec{F}_{jp}$ between the particles in the (2.23) is obtained by taking minus gradient of the interaction potential

$$\vec{F}_{jp} = -\frac{\partial \Phi}{\partial x_j},$$

if the interaction potential Φ is conservative.

A type of the potential depends on the complexity of the interaction between particles. One of the simplest representations of the interaction is in noble gases.

Noble gases have weak interatomic forces due to the ‘full’ outer shell of the valence electrons, and they are all monoatomic gases under normal conditions. Thus, no complex or long range interactions are involved, that eventually saves computational costs.

The interacting potential, originally proposed for noble gases such as liquid argon, is called Lennard-Jones potential (LJ) or $6-12$ potential. It is a simple mathematical model that approximates the interaction between a pair of neutral atoms or molecules.

In mathematical terms LJ potential is given by

$$\Phi_{LJ}(r_{ij}) = \varepsilon_{LJ}\left(\left(\frac{\sigma_{LJ}}{r_{ij}}\right)^{12} - \left(\frac{\sigma_{LJ}}{r_{ij}}\right)^{6}\right), \tag{2.24}$$

where $\sigma_{LJ}, \varepsilon_{LJ}$ are the model’s parameters describing the length and depth of the potential and r_{ij} is the distance between the interacting particles. This potential is widely used in MD simulations.

Water, which is more often used in experiments and is much more complex liquid than liquid argon, is not a good choice to start with. Since the complexity of the water molecules interaction requires more computational efforts.

For that reason we gradually increase the complexity of the solvent, that is the interaction potential, starting with the LJ potential switching to BN2D and, finally, the SPC/E water model.

The BN2D water model is discussed in details in Chapter 3. The SPC/E model detailed explanation can be found in [51] and a brief description in Section 3.3.

It should be noted, that the BN2D water model developed by Ben -Naim gives atomic structural details and three-dimensionality, although it is a two-dimensional model. This model uses only few parameters and is computationally simple enough, and eventually mimics anomalous water properties.

In application to large systems, the dimensionality (2 or 3) makes critical difference in terms of computational effort. Other benefit of BN2D water model is that it treats hydrogen bonding geometrically, that does not require to calculate long range Coulomb interactions, which are computationally expensive [56].

Thus, the most computationally expensive are three-dimensional model/cases. For which there are many realistic water models, such as standard TIP3P, TIP4P, SPC/E, etc., [57] as well as 3D 'Mercedes Benz' water model [58].

Algorithms and methods

Numerically Molecular Dynamics simulations are ill-conditioned, creating cumulative errors in numerical integration, that cannot be eliminated. However they can be minimized by a proper selection of algorithms and parameters.

A simple numerical scheme which is widely used in MD is known as Leapfrog or Verlet method. This method yields coordinates that are accurate to third order in time dt, and, from the point of view of energy conservation when Lennard - Jones type potentials are used, tend to be considerably better than the higher-order methods. The storage requirements are also minimal [25, 59].

In the Verlet scheme, the velocity $\dot{x}$ evolution is calculated at each half timestep, while the coordinates x are calculated only once. These steps are presented as

$$\begin{gathered}\dot{x}(t+\frac{h}{2})=\dot{x}(t)+\frac{h}{2}\cdot\ddot{x}(t), \\ x(t+h)=x(t)+h\cdot\dot{x}(t+\frac{h}{2})\end{gathered} \tag{2.25}$$

followed by

$$\dot{x}(t+h)=\dot{x}(t+\frac{h}{2})+\frac{h}{2}\cdot\ddot{x}(t+h),$$

where $\ddot{x}$ is the acceleration, that from the Newton's second law is related to force. When the coupling is used the conventional velocities and accelerations are replaced with the ones defined in (2.42) and (2.43).

From a computational point of view substantial improvement can be made if interaction between particles is evaluated over a small range, slightly bigger than r_{cut}, that is the distance, after which the contribution to the force acting on the particle is negligible. For that reason the search of interacting (neighbouring) particles must be improved. One of the methods that can be used in this case is called *cell list* method [59].

The *cell list* method used here can be described as the following procedure: all simulation domain is subdivided into the lattice of small cells, such that the cell length is slightly bigger than r_{cut}. All atoms are assigned to the relevant cells based on their location. The interaction between the particles can be only with the particles located in the same or neighbouring cells. Due to the symmetry only half of these cells must be evaluated. This technique is proved to be very useful in the reduction of the computational effort during the force evaluation.

This method is improved even further and is called *neighbouring list*, more information regarding these methods can be found in [59].

Other technical aspect is related to the systems, that are considered as infinite, in this case periodic boundaries are introduced. This technique allows the atoms that leave the simulation domain through a boundary face and instantly return through the opposite face.

During the MD simulation, there is a gradual energy drift due to cumulative numerical errors, that depend on the integration method, potential function, etc. In order to eliminate this energy drift velocity adjustment is required during the simulation. A procedure called *velocity rescaling* can infrequently adjust the particles velocities to an average velocity that is defined by the temperature set for the particular simulation.

Other feature of the Verlet algorithm/method is that it naturally produces the NVE ensemble, that dictates the conditions of the simulation.

Statistical ensembles were defined by Gibbs [60]:

- “Microcanonical ensemble or NVE ensemble — a statistical ensemble where the total energy of the system and the number of particles in the system are each fixed to particular values; each of the members of the ensemble are required to have the same total energy and particle number. The system must remain totally isolated (unable to exchange energy or particles with its environment) in order to stay in statistical equilibrium.”

- “Isothermal–isobaric ensemble (constant temperature and constant pressure ensemble) is a statistical mechanical ensemble that maintains constant temperature T, and constant pressure P, applied. It is also called the NPT - ensemble, where the number of particles N, is also kept as a constant. This ensemble plays an important role in chemistry as chemical reactions are usually carried out under constant pressure condition.”

We do not present a full list of ensembles, since only two of them were used in this work.

Throughout this work the NVE ensemble is used, however the NPT ensemble is also implemented, when BN2D water model properties were compared between the ensembles and with the real water.

2.2.2 Landau Lifshitz-Fluctuating Hydrodynamics

Here a concise review of Landau Lifshitz-Fluctuating Hydrodynamics (LL-FH) equations is undertaken. These LL-FH conservation equations proved to be effective for the mesoscopic scales simulations [61].

The LL-FH method, which was initially proposed by Landau and Lifshitz, accounts for the microstructure influence on the macroscale behaviour of the system. They suggested that the mesoscopic scales can be described by Navier-Stokes hydrodynamic equations with added stochastic forcing terms which ensure that the fluctuation-dissipation balance principle is satisfied and essentially account for the thermal fluctuations, that originate from the microscopic molecular motion [25]. This assumption is also consistent with the MD phase microscopic nature.

Considerations above can be expressed in the full set of equations

$$\begin{gathered}
\frac{\partial \rho}{\partial t}+\frac{\partial}{\partial x_j}(\rho u_j)=0, \qquad (2.26)\\
\frac{\partial \rho u_i}{\partial t}+\frac{\partial}{\partial x_j}(\rho u_i u_j)=\frac{\partial}{\partial x_j}\left(\Pi_{ij}+\tilde{\Pi}_{ij}\right),\ i=1,2,3,\\
\frac{\partial \rho E}{\partial t}+\frac{\partial}{\partial x_j}(\rho E u_j)=\frac{\partial}{\partial x_j}\left(\left(\Pi_{ij}+\tilde{\Pi}_{ij}\right)\cdot u_i\right)+\frac{\partial}{\partial x_j}(q_j+\tilde{q}_j),
\end{gathered}$$

where ρ is the fluid density, $\vec{u}$ is the fluid velocity, Π_{ij} is the stress tensor, the stochastic stress tensor is $\tilde{\Pi}_{ij}$, the stochastic energy flux is $\tilde{\vec{q}}$, t denotes time and i, j are spatial coordinates (x, y or z).

The dissipative stress tensor is defined as

$$\Pi_{ij}=-\left(p-\xi\frac{\partial u_j}{\partial x_j}\right)\delta_{ij}+\eta\left(\frac{\partial u_j}{\partial x_i}+\frac{\partial u_i}{\partial x_j}-2D^{-1}\frac{\partial u_j}{\partial x_j}\cdot\delta_{ij}\right), \qquad (2.27)$$

with ξ and η are the shear and bulk viscosities, D is the dimension of the system, p is the pressure and δ_{ij} is the Kronecker delta function.

In order to estimate the stochastic stress tensor fluctuation-dissipation theorem (FDT) [62] is used, which predicts the behaviour of non-equilibrium thermodynamical systems.

The theorem provides the balance between the fluctuations in the system and its dissipative properties. If the balance is violated then system's behaviour can be either dominated by the fluctuations or become too dissipative. In the first case we get instabilities, while in the second case very small fluctuations. Thus it is important to maintain the balance between these two properties.

The FDT provides us with the covariance of stochastic stress tensor

$$\langle \tilde{\Pi}_{ij}(r,t) \cdot \tilde{\Pi}_{kl}(r',t') \rangle = 2k_B T \left[\eta \left(\delta_{ik}\delta_{jl} + \delta_{il}\delta_{jk} \right) + \left(\xi - \frac{2}{3}\eta \right) \delta_{ij}\delta_{kl} \right] \times \delta(r-r')\delta(t-t') \tag{2.28}$$

that yields stochastic stress [61] expressed as

$$\tilde{\Pi}_{ij} = \sqrt{\frac{2k_B T}{\delta t \delta V}} \left(\sqrt{2}\sqrt{\eta} \cdot \mathbf{G}^s_{ij} + \sqrt{D}\sqrt{\xi}\frac{tr[\mathbf{G}]}{D}\mathbf{E}_{ij} \right), \tag{2.29}$$

where $\mathbf{G}$ is Gaussian random matrix, $\mathbf{G}^s_{ij} = \frac{\mathbf{G}_{ij}+\mathbf{G}^T_{ij}}{2} - \frac{tr[\mathbf{G}]}{D}\mathbf{E}_{ij}$, $\mathbf{E}$ is the unity matrix and $tr[\mathbf{G}] = G_{11} + G_{22} + G_{33}$, which stands for the matrix trace, k_B is Boltzmann constant, T is the temperature. The Gaussian random matrix $\mathbf{G}$ is a matrix which elements are randomly generated with the Gaussian distribution [63].

The first equation in (2.26) is the standard Navier-Stokes mass conservation equation, the second equation is the momentum conservation equations with the stochastic forcing terms, and the last is the energy equation with the stochastic energy flux term.

As was mentioned before, the FH phase is modelled using a generalisation of the deterministic Navier-Stokes equations for microscopic flows, that is LL-FH.

The main benefit of LL-FH model is that it allows accurate modelling of statistical properties of the atomistic fluctuations. On the other hand, in the limit of large volumes, the LL-FH model tends to the conventional Navier-Stokes equations. Most notably, when the space and time scales become small, the LL-FH equations are able to account for the thermal motion of molecules.

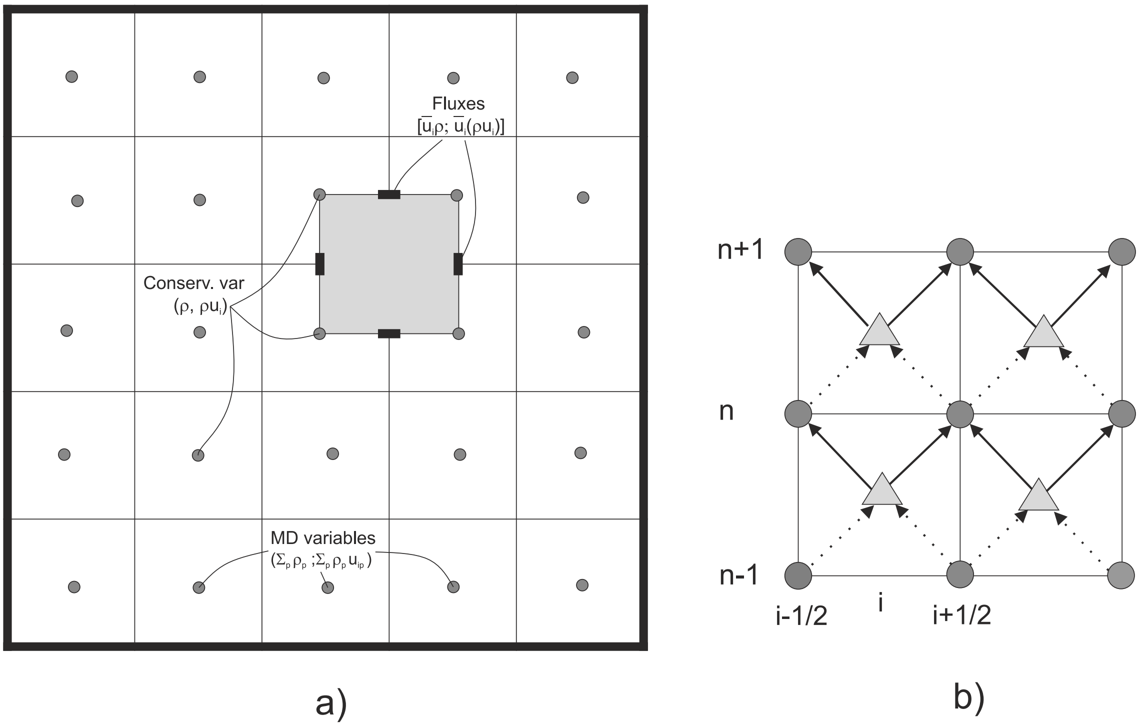

Figure 2.2: Schematic representation of the numerical schemes. a) Conserved variables of the MD and FH phase, such as density and momentum are defined at the cell's centre on the regular grid, while the mass and momentum fluxes are located on the cell faces. b) The CABARET numerical scheme evaluates conservative variables (circles) every half timestep, while the fluxes (triangles) are obtained every timestep between the conservative variables evaluation

The modified FH phase conservation equations, (2.4) and (2.15), together with (2.9) and (2.18) are solved numerically with the Eulerian methods which have reached mature state in Computational Fluid Dynamics. In the current implementation, the governing partial differential equations of the FH phase are discretised using a Central Leapfrog finite-difference scheme for the left hand side advection terms and the central finite differences for the right hand side source terms. The total order of approximation is two in space and time. For enhanced numerical stability, a staggered formulation of the Central Leapfrog scheme is used by introducing separate variables for the cell centres and the cell faces, Fig. 2.2a, together with a low-dissipative non-linear flux correction. The details of the staggered nonlinear Central Leapfrog scheme for advection equation as well as its implementation for the classical Landau Lifshitz-Fluctuating Hydrodynamics equations can be found in [64, 65].

In this work two different approaches of communication between disparate scales are considered, where the LL-FH simulation is different for each case.

2.2.3 Interpolation in between the scales

An interpolation is used since the LL-FH method provides data only for the grid points while MD particles can be located anywhere in the simulation domain.

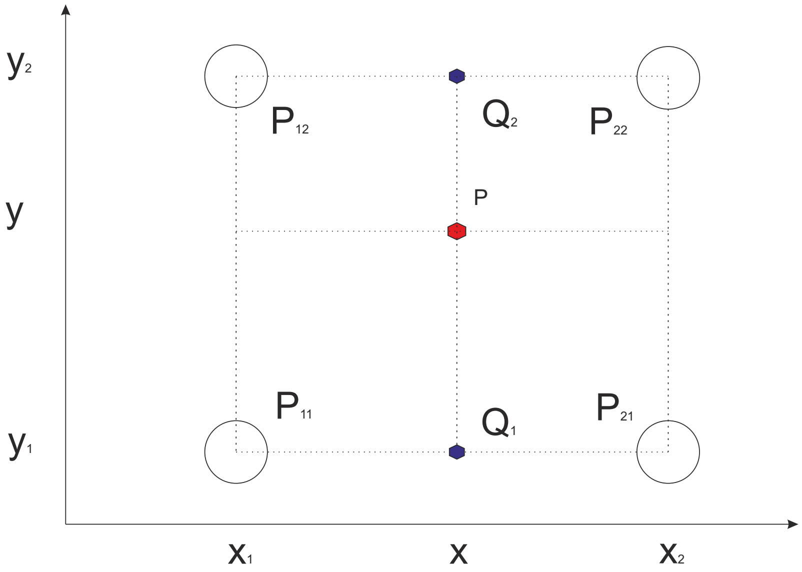

Figure 2.3: Linear interpolation illustration in 2D space (x and y)

In this work linear interpolation is implemented, Fig. 2.3, where P is the location of a particle and $P_{11}, P_{12}, P_{21}, P_{22}$ are the grid points, where the MD and FH phase densities and momentum are available.

Linear interpolation for location P is performed as subsequent steps of linear interpolation for the positions Q_1 and Q_2 using the following relationships

$$f(Q_1) \approx \frac{x_2 - x}{x_2 - x_1} f(P_{11}) + \frac{x - x_1}{x_2 - x_1} f(P_{21}) \tag{2.30}$$

and

$$f(Q_2) \approx \frac{x_2 - x}{x_2 - x_1} f(P_{12}) + \frac{x - x_1}{x_2 - x_1} f(P_{22}) \tag{2.31}$$

followed by the linear interpolation between Q_1 and Q_2 for the location P

$$f(P) \approx \frac{y_2 - y}{y_2 - y_1} f(P1) + \frac{y - y_1}{y_2 - y_1} f(P_2). \tag{2.32}$$

Note, that this procedure is applied to each MD particle.

2.2.4 Communicating large and small scales

The subject of this subsection is the communication between the FH and MD phases. According to the previous assumptions, it is known, that each phase properties have dual nature.

First, the continuum properties of each phase, such as the MD phase density $\sum_p \rho_p$ and momentum $\sum_p \rho_p u_{ip}$ and the FH phase density ρ and momentum u_i are situated at the cell centres of the regular grid Fig. 2.2a, and the FH phase density flux $\tilde{u}_i \rho$ and momentum flux $\tilde{u}_i(\rho u_i)$ at the cell faces.

Second, atomistic properties, where the FH phase density and momentum are considered by means of stochastic terms and the MD phase density and momentum are obtained using MD particles positions and velocities. Note, that the density of particles ρ_p is the same regardless the values of the coupling parameter s. Thus scaling of the interaction potential between MD particles is not required.

Successful communication between the phases requires information from both MD and LL-FH simulations, thus an update/exchange of the MD phase density $\sum_p \rho_p$ and momentum $\sum_p \rho_p u_{ip}$ with the FH phase density $\tilde{\rho}$ and momentum $\tilde{\rho}\tilde{u}_i$ is handled simultaneously.

An essential criteria is that the time lapse in both simulations is the same. It means that if the ratio between the timesteps in LL-FH and MD simulations is $n = dt_{FH}/dt_{MD}$, then every n^{th} MD iteration the MD phase was advanced to the one timestep of the FH phase. At this point the data between the phases can be exchanged.

It is also important to note, that the periodic boundary conditions were used to avoid surface tension and rigid boundary effect during the simulations. Additionally, a linear interpolation was used, since the FH and MD phase densities and momentum are available only at the cell centres, whereas MD particles can be located anywhere in the simulation domain.

The coupling framework encompasses multiple approaches joined together in a consistent manner. It is composed of different techniques and, obviously, requires an assessment of credibility and accuracy. Otherwise a lack of validity and effectiveness will undermine the applicability of coupling method itself. Thus, we used a set of conditions and combination of techniques to determine whether the method works as it was originally expected.

If our assertions prove to be valid, the consequent step would be to apply this method to water models. Such application would be favourable and encouraging in a sense of computation effort minimization, when protein folding and other important biomolecular processes or large systems, such as virus in water are studied.

Also we would have a mapping technique from the large to small scales, which is based on the physical analogy.

We suggest two approaches, each of which uses different combinations of equations obtained in previous sections as well as a set of conditions.

According to the first coupling approach, denoted as ‘one way’ coupling, we employ new equations of motion (2.13) and (2.23) for the MD particles, and a standard LL-FH simulation for the FH phase. Therefore, if $s \neq 0$, we expect that these new equations of motion will alter trajectories of the MD particles. The change of the trajectories will result in the MD phase resemblance with the FH phase. That means that the fluctuations of the densities and momenta of the MD phase become correlated with the FH phase, but not the other way around, since the FH phase fluctuations were obtained from a stand-alone LL-FH simulation. As a consequence, when s is gradually increased the resemblance between the MD and FH phase gets more pronounced.

The second coupling approach, denoted as ‘two way’ coupling, utilizes (2.4) and (2.15) for the FH phase simultaneously with the equations of the MD phase (2.13) and (2.23). In this case the MD particles experience similar effect of the coupling as in the ‘one way’ coupling, although the ‘two way’ coupling is different. The difference is in the MD and FH phase communication, since in ‘two way’ coupling MD phase density and momentum fluctuations provide a feedback to the FH phase, thereby amending FH phase fluctuations.

We have studied these two coupling approaches in details and results are presented in the further sections.

Both coupling approaches were considered in the adiabatic systems (energy equation is not integrated).

2.3 ‘One way’ coupling

The ‘one way’ coupling implementation is split into two categories, one corresponds to the FH and the other to the MD phase. In general, the equations that are used in the coupling require information, such as densities and momenta of both phases, however in the ‘one way’ case the FH phase must be know beforehand. For that reason the FH phase fluctuations are obtained in advance with the standard LL-FH simulation. This simulation provides with the values of the densities and momenta at the grid cell centres for a certain period of time. Then these values are used directly in the coupled equations of the MD phase.

2.3.1 FH phase

This subsection is throughout devoted to the standard Landau Lifshitz-Fluctuating Hydrodynamics.

The LL-FH is an extrapolation of the continuum hydrodynamics below the range of applicability. The LL-FH governing equations are the Navier-Stokes equations with the fluctuating flux terms of energy and momentum. The intensity of these fluxes is determined by the temperature and the spatial and temporal scales, such that the fluctuating dissipative theorem is satisfied. In the LL-FH context the spatial scale is meant to be the size of the grid cells, Fig. 2.2a.

The energy conservation decouples from the mass and momentum conservation equations, when no stochastic energy flux is present, that is true for the adiabatic systems.

The standard LL-FH governing equations (without energy conservation equation) are given by

$$\frac{\partial \rho}{\partial t} + \frac{\partial}{\partial x_j}(\rho u_j) = 0, \tag{2.33}$$
$$\frac{\partial \rho u_i}{\partial t} + \frac{\partial}{\partial x_j}(\rho u_i u_j) = \frac{\partial}{\partial x_j}\left(\Pi_{ij} + \tilde{\Pi}_{ij}\right),\ i = 1,2,3,$$

where the first equation corresponds to the mass conservation followed by the momentum conservation equation.

We keep the same considerations and notations as previously, where i, j are the spatial coordinates (x, y or z), ρ is the fluid density, u_j is the fluid velocity i^{th} component, Π_{ij} is the stress tensor, the stochastic stress tensor is $\tilde{\Pi}_{ij}$, the stochastic energy flux is $\tilde{\vec{q}}$, and t denotes time.

The stress tensor is defined as

$$\Pi_{ij} = -\left(p - \xi\frac{\partial u_j}{\partial x_j}\right)\delta_{ij} + \eta\left(\frac{\partial u_j}{\partial x_i} + \frac{\partial u_i}{\partial x_j} - 2D^{-1}\frac{\partial u_j}{\partial x_j}\cdot\delta_{ij}\right), \tag{2.34}$$

with ξ and η are the shear and bulk viscosities, D is the dimension of the system, p is the pressure and δ_{ij} is the Kronecker delta function.

The stochastic stress [61] is expressed as

$$\tilde{\Pi}_{ij} = \sqrt{\frac{2k_B T}{\delta t \delta V}}\left(\sqrt{2}\sqrt{\eta}\cdot\mathbf{G}^s_{ij} + \sqrt{D}\sqrt{\xi}\frac{tr[\mathbf{G}]}{D}\mathbf{E}_{ij}\right), \tag{2.35}$$

where $\mathbf{G}$ is Gaussian random matrix, $\mathbf{G}^s_{ij} = \frac{\mathbf{G}_{ij}+\mathbf{G}^T_{ij}}{2} - \frac{tr[\mathbf{G}]}{D}\mathbf{E}_{ij}$, $\mathbf{E}$ is the unity matrix and $tr[\mathbf{G}] = G_{11} + G_{22} + G_{33}$, which stands for the matrix trace, k_B is Boltzmann constant, T is the temperature.

2.3.2 LL-FH simulation

Following standard approaches in CFD, the partial differential equations of the LL-FH are solved using numerical methods. There are many different numerical schemes available in CFD, although every scheme has its limitations and benefits [23].

Here, for instance, the CABARET scheme [64, 65] was used for the LL-FH simulations. This numerical scheme possesses improved dispersion and dissipative properties in comparison with the other approaches. In distinction from the schemes based on the central differences, the CABARET scheme does not yield spurious reflected waves travelling in the opposite direction even on a very coarse grids, that is common for other schemes [64].

In Fig. 2.2b the numerical scheme for the solution of the set of LL-FH governing equations is shown. The solution is constructed using an explicit predictor-corrector algorithm (Verlet) which consists of the three consecutive stages presented in Algorithm. 1.

Algorithm 1: Pseudo-code for the standard LL-FH simulation

```
Result: Fluctuations of the velocities and densities of the FH phase
for $n \leq$ simulation time do
    Predictor: Calculate the intermediate conservative variables $\rho_{i+1/2}^{n+1/2}$ and $(\rho u)_{i+1/2}^{n+1/2}$ at the half timestep;
    Extrapolation: Calculate the flux variables for the next time layer $n+1$ using characteristic decomposition method;
    Corrector: Calculate the conservative variables $\rho_{i+1/2}^{n+1}$ and $(\rho u)_{i+1/2}^{n+1}$ for the next timestep;
    Post processing: Collect statistics;
end
```

In terms of finite differences the mass conservation equation of the LL-FH using CABARET scheme is written as [64]

$$\frac{\rho_{i+1/2}^{n+1/2}-\rho_{i+1/2}^{n}}{0.5\cdot\tau^{n+1/2}}+\frac{\rho_{i+1}^{n}u_{i+1}^{n}-\rho_{i}^{n}u_{i}^{n}}{x_{i+1}-x_{i}}=0, \tag{2.36}$$

and the momentum equation is expressed as

$$\frac{\rho_{i+1/2}^{n+1/2}u_{i+1/2}^{n+1/2}-\rho_{i+1/2}^{n}u_{i+1/2}^{n}}{0.5\cdot\tau^{n+1/2}}+\frac{\rho_{i+1}^{n}u_{i+1}^{n}u_{i+1}^{n}-\rho_{i}^{n}u_{i}^{n}u_{i}^{n}}{x_{i+1}-x_{i}}+\frac{p_{i+1}^{n}-p_{i}^{n}}{x_{i+1}-x_{i}}= \tag{2.37}$$
$$=\frac{\Pi_{i+1}^{n+1/2}-\Pi_{i}^{n+1/2}}{x_{i+1}-x_{i}}+\frac{\tilde{\Pi}_{i+1}^{n+1/2}-\tilde{\Pi}_{i}^{n+1/2}}{x_{i+1}-x_{i}}.$$

The flux variables are calculated using characteristic decomposition method, where Riemann invariants for the set of equations (2.33) are $R=u+c\ln\rho$ and $Q=u-c\ln\rho$, with the characteristic speeds $\lambda_{1,2}=u\pm c$, where c is the speed of sound (derivations can be found in Appendix A.2).

The extrapolation of the fluxes is accomplished in several steps

- Update of invariants

  $$X_{i}^{n+1}=X_{i+1/2}^{n+1/2}+X_{i-1/2}^{n+1/2}-X_{i}^{n},$$

  where $X=(R,Q)$.

- Correct invariants according to the maximum principle

$$\phi_{i}^{n+1}=\phi_{i}^{n+1},\ \min(\phi_{i}^{n})\leq\phi_{i}^{n+1}\leq\max(\phi_{i}^{n}), \tag{2.38}$$
$$\phi_{i}^{n+1}=\min(\phi_{i}^{n}),\ \phi_{i}^{n+1}<\min(\phi_{i}^{n}),$$
$$\phi_{i}^{n+1}=\max(\phi_{i}^{n}),\ \phi_{i}^{n+1}>\max(\phi_{i}^{n}),$$

where

$$\min(\phi_i^n) = \Big(\min(R_{i-1}^n, R_{i-1/2}^n, R_i^n) + \min(R_i^n, R_{i+1/2}^n, R_{i+1}^n)\Big)/2 + \Big((F_1)_{i-1/2}^n + (F_1)_{i+1/2}^n\Big)/2$$

and

$$\max(\phi_i^n) = \Big(\max(R_{i-1}^n, R_{i-1/2}^n, R_i^n) + \max(R_i^n, R_{i+1/2}^n, R_{i+1}^n)\Big)/2 + \Big((F_1)_{i-1/2}^n + (F_1)_{i+1/2}^n\Big)/2,$$

here sources are evaluated as

$$(F_1)_{i-1/2}^n = \frac{R_{i-1/2}^{n+1/2} - R_{i-1/2}^n}{0.5 \cdot \tau^{n+1/2}} + (\lambda_1)_{i-1/2}^{n+1/2} \frac{R_i^n - R_{i-1}^n}{x_i - x_{i-1}},$$

$$(F_1)_{i+1/2}^n = \frac{R_{i+1/2}^{n+1/2} - R_{i+1/2}^n}{0.5 \cdot \tau^{n+1/2}} + (\lambda_1)_{i+1/2}^{n+1/2} \frac{R_{i+1}^n - R_i^n}{x_{i+1} - x_i}.$$

The same procedure is applied to the Q invariant.

The fluxes at the time layer $n+1$ are used to calculate the conservative variables ρ^{n+1} and u^{n+1} for the next time layer

$$\frac{\rho_{i+1/2}^{n+1} - \rho_{i+1/2}^{n+1/2}}{0.5 \cdot \tau^{n+1/2}} + \frac{\rho_{i+1}^{n+1} u_{i+1}^{n+1} - \rho_i^{n+1} u_i^{n+1}}{x_{i+1} - x_i} = 0$$

and

$$\frac{\rho_{i+1/2}^{n+1} u_{i+1/2}^{n+1} - \rho_{i+1/2}^{n+1/2} u_{i+1/2}^{n+1/2}}{0.5 \cdot \tau^{n+1/2}} + \frac{\rho_{i+1}^{n+1} u_{i+1}^{n+1} u_{i+1}^{n+1} - \rho_i^{n+1} u_i^{n+1} u_i^{n+1}}{x_{i+1} - x_i} + \frac{p_{i+1}^{n+1} - p_i^{n+1}}{x_{i+1} - x_i} = \tag{2.39}$$

$$= \frac{\tau_{i+1}^{n+1/2} - \tau_i^{n+1/2}}{x_{i+1} - x_i} + \frac{\tau^{s}{}_{i+1}^{n+1/2} - \tau^{s}{}_{i}^{n+1/2}}{x_{i+1} - x_i}.$$

The LL-FH simulation provides us with the set of data, that consists of the fluctuating variables such as density ρ and momentum ρu_i in each grid cell. This data is denoted as the FH phase fluctuations and is used in the new equations of motion of the MD particles .

2.3.3 MD phase

In this subsection the MD phase equations are completed with the definitions of the coupling operators L^{ρ} and L^{u}.

The MD phase should follow the fluctuations of the FH phase, when $s \rightarrow 1$, because the new equations of motion of the MD phase involve terms that drive the differences of the densities and the momenta between the phases to a prescribed value. From the physical point of view, this is due to the external force created by the coupling, that impose the FH phase fluctuations on the MD phase, leading to the new particles trajectories.

The difference between the MD and FH phase densities and momenta play essential role in the coupling, while the strength of coupling is characterized by adjustable parameters, such as s, α, β

and the chosen type of the forcing. It is recommended to use 'mild' L^{ρ} and L^{u} operators, that do not impose substantial constraints on the MD particles movements, when the effect of coupling is expected to be small. Additionally, we choose L^{u} operator, such that at the limit $s = 1$ we recover standard LL-FH model for the FH phase. Here we consider diffusive type of operators L^{ρ} and L^{u}.

An operator L^{ρ} for the mass conservation is assumed to be

$$L^{\rho} \cdot \left(\tilde{\rho} - \sum_{p} \rho_p \right) = \frac{\partial}{\partial x_i} \left[s\,(1-s)\,\alpha \frac{\partial}{\partial x_i} \left(\tilde{\rho} - \sum_{p} \rho_p \right) \right] \tag{2.40}$$

and for the momentum conservation L^{u} was chosen as

$$L^{u} \cdot \left(\tilde{u_j}\tilde{\rho} - \sum_{p} \rho_p u_{jp} \right) = \frac{\partial}{\partial x_j} \left[s\,(1-s)\,\beta \frac{\partial}{\partial x_j} \left(\tilde{u_j}\tilde{\rho} - \sum_{p} \rho_p u_{jp} \right) \right]. \tag{2.41}$$

Here, new parameters α and β were introduced. These parameters allow to adjust the strength of the forcing operators. In this case α and β can be regarded as a diffusion coefficients, although the diffusion is unphysical, since we consider phases that do not exist in real life. From the technical point of view, α and β parameters are chosen for the numerical stability. The requirement for the parameters is that $\alpha, \beta > 0$, that will sustain the convergence between the densities and momenta of the two phases. The magnitude of the parameters controls the stability of simulations. Criteria for choosing α and β will be discussed in the following sections.

The new equations of motion of MD particles according to the definitions of the L^{ρ} operator, (2.40), yields the following velocities for each MD particle

$$\frac{dx_{ip}}{dt} = u_{ip} + s(\tilde{u}_i - u_{ip}) + s(1-s)\alpha(x)\frac{1}{\rho_p N(t)}\frac{\partial}{\partial x_i}\left(\tilde{\rho} - \sum_{p} \rho_p \right), \tag{2.42}$$

and according to the L^{u} definition (2.41) following acceleration of a single particle is obtained

$$\frac{\partial u^{N}_{jp}}{\partial t} = (1-s)\frac{F_{jp}}{\rho_p V_{cell}} + \frac{1}{\rho_p N(t)} \times \tag{2.43}$$

$$\times \left[sF_j + \frac{\partial}{\partial x_i}\left(s(1-s)\alpha(x)\frac{\partial}{\partial x_i}\left(\tilde{\rho} - \sum_{p} \rho_p \right) \right) \frac{\sum_p u_{jp}}{N(t)} - \frac{\partial}{\partial x_i}\left(s(1-s)\beta(x)\frac{\partial}{\partial x_i}\left(\tilde{u_j}\tilde{\rho} - \sum_{p} \rho_p u_{jp} \right) \right) \right].$$

Equation above shows, that when $s = 0$ we recover pure MD equations of motion. When $s = 1$ MD particles experience FH force, which alters their velocities. Later, these velocities are disregarded when particles positions are updated (2.42). Thus, a 'static structure' of MD particles is moving with the FH phase flow velocity. At the limit $s = 0$ or $s = 1$ contribution from the terms $\tilde{\rho} - \sum_p \rho_p$ and $\tilde{u_j}\tilde{\rho} - \sum_p \rho_p u_{jp}$ becomes zero, that means either the MD or FH phase does not exist and there is no reference for the MD phase to be driven to.

2.3.4 MD simulation

The MD phase simulation details are described in this subsection. The 2D Lennard- Jones liquid is used for testing the coupling method. This interaction potential gives a good approximation for the study of argon and is given by

$$\Phi_{LJ}(r_{ij}) = \varepsilon_{LJ}\left(\left(\frac{\sigma_{LJ}}{r_{ij}}\right)^{12} - \left(\frac{\sigma_{LJ}}{r_{ij}}\right)^{6}\right), \tag{2.44}$$

where $\sigma_{LJ}, \varepsilon_{LJ}$ are the model's parameters describing the length and depth of the potential and r_{ij} is the distance between the interacting particles. This potential is widely used in MD simulations, and is accurate enough for illustrating the application of the coupling method to realistic liquid.

At this point dimensionless units are introduced, they provide various benefits, starting from the ability to solve a whole class of problems, that can be consequently scaled to the physical units, ending with the reduction of the computational effort and storage requirement, since the most of the variables and parameters are close to unity.

The dimensionless units are defined by choosing σ , m and ε to be the units of length, mass, and energy, respectively, and making the replacements

- length: $r \to r^*\sigma$;
- energy: $e \to e^*\varepsilon$;
- time: $t \to t^*\sqrt{\frac{m\sigma^2}{\varepsilon}}$;

that provide us with the dimensionless length r^*, energy e^* and time t^*.

From now on, all variables involved in the computation and presented on the figures are expressed in the dimensionless units, unless it is said otherwise. Thus, we denote dimensionless density of the FH phase as ρ, of the MD phase as $\sum_p \rho_p$ and of the mixture as $\tilde{\rho}$. The dimensionless velocity of the FH phase is u_i, of the MD phase is $\sum_p u_{ip}$ and of the mixture is $\tilde{u}_i$, where i is the spatial component (x, y or z).

As was mentioned in the previous sections, the simulation of the MD phase coupled with the FH phase is carried out using Molecular Dynamics methods, specifically, the Verlet algorithm and the new equations of motion (2.42) and (2.43).

MD particles coordinates and velocities are obtained according to the procedure explained in Algorithm. 2.

Algorithm 2: Pseudo code for the ‘one way’ coupling

```
Result: Obtain MD particles coordinates and velocities
for $n \leq$ simulation time do
    if $n = dt_{HD}/dt_{MD}$ then
        assign the FH phase $\rho$ and $\rho u_i$ to the cell centres from the LL-FH simulation;
    else
        calculate $\sum_p \rho_p$ and $\sum_p \rho_p u_{ip}$ for each cell;
        update coordinates and velocities using modified equations of motion (2.42) and (2.43) at the half timestep ;
        calculate interaction forces and $\sum_p \rho_p u_{ip}$ for each cell;
        update velocities using modified equations of motion (2.43) at the half timestep ;
    end
    use $\sum_p \rho_p$ and $\sum_p \rho_p u_{ip}$ for analysis;
end
```

Since the FH phase density and momentum were obtained from the stand-alone LL-FH simulation, the terms in (2.42) and (2.43) related to α and β can be calculated. The MD phase density is calculated in the following way: all particles inside the cell are summed and divided over the volume of the cell, thus, the density $\sum_p \rho_p$ is obtained for each cell. The momentum is obtained in a similar way: multiply the density ρ_p and velocity u_{ip} of a particle and sum them over the cell, this will yield the MD phase momentum $\sum_p \rho_p u_{ip}$.

Now the FH and MD phase properties are known, and the new equations of motion can be evaluated. It must be noted, that the linear interpolation is used, since the MD and FH phase properties are available only at the cell centres, however they are required in the whole domain.

According to the Verlet algorithm, the velocities are updated every half timestep and the coordinates every timestep between the velocity evaluation procedure. Hence, the MD phase density $\sum_p \rho_p$ and momentum $\sum_p \rho_p u_{ip}$ are estimated at every half timestep.

All simulations were conducted in the dimensionless units, that were obtained using the Lennard-Jones model parameters from Table. 2.1, yielding dimensionless values for the simulation conditions listed in Table. 2.2.

Rounding and cut-off errors were minimized at every 100^{th} MD iteration using the velocity rescaling technique.

A sets of coupling coefficients $\alpha^*, \beta^* = 2/1000/20000$ and $s = 0.1/0.5/0.8/0.95$ were used and considered to be sufficient enough to test the coupling method.

Parameter	Value
ε_{LJ}	122.4 [K]
σ_{LJ}	3.432 [Å]
m	$39.948/N_A\ [\frac{gr}{mol}]$

Table 2.1: Lennard-Jones potential parameters, where N_A is Avagadro number [4]

Parameter	Dimensionless value
T^*	2.45
ρ^*	0.607
N	10 000
dt^*_{MD}	0.005
dt^*_{FH}	0.05
η^*	1.011
ξ^*	0.337
ε^*_{LJ}	1
σ^*_{LJ}	1
Number of cells (N_{cell})	5 x 5 (25)

Table 2.2: ‘One way’ coupling simulation conditions in dimensionless units (LJ potential)

2.3.5 Stability analysis

This subsection is devoted to the stability analysis and the simulation results that we obtained using the ‘one way’ coupling. We perform the analysis using densities and momenta of the FH and MD phase, that were available from 25 cells. The 10000 MD particles were used for the study of the velocity autocorrelation and radial distribution functions.

Here we introduce the relative density difference between the FH and MD phase which is given by

$$\Theta^\rho = \frac{\rho - \sum_p \rho_p}{\rho_{avg}} \tag{2.45}$$

and the relative velocity difference between the FH and MD phase

$$\Theta_i^u = \frac{u_i - \sum_p u_{ip}}{u_{avg}}, \tag{2.46}$$

where ρ_{avg} is the average density (denoted by ρ^* in Table 2.2), $u_{avg} = \sqrt{\frac{N_{cell} \cdot T}{N}}$ denotes average velocity which corresponds to the set temperature T, N_{cell} is the number of cells, N is the number of MD particles in simulation, $\sum_p$ is performed over all MD particles in the current cell and i stands for the velocity component (x, y or z).

As expected the MD particles followed new rules of motion when coupling was used. These rules are described by (2.42) and (2.43), which are able to minimize the difference between the MD and FH phase densities and momenta fluctuations. The MD particles coordinates are slightly adjusted to produce the desired value of the MD phase density. This adjustment gets more pronounced when parameters s and α^*, β^* are increased.

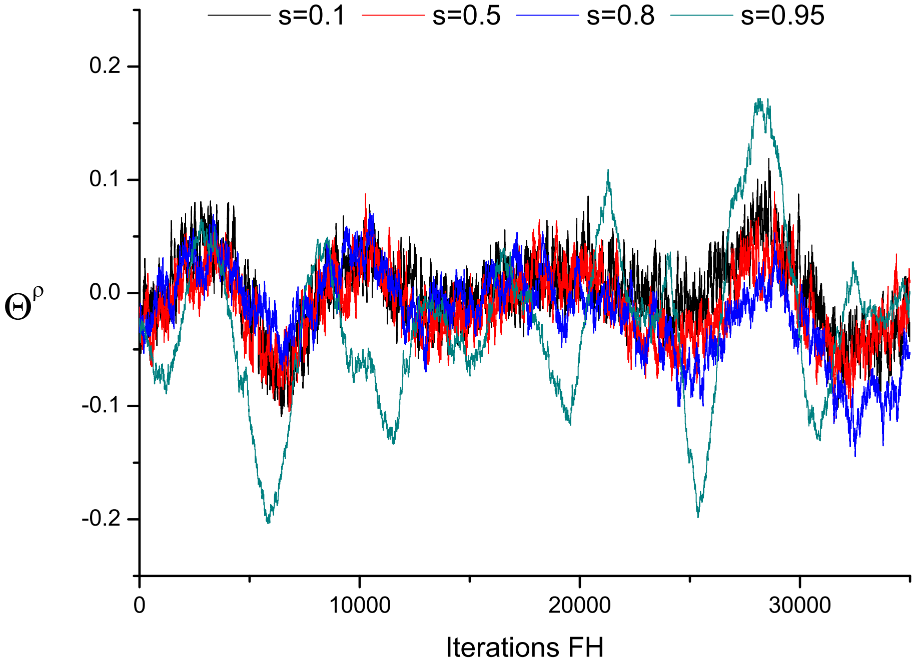

Figure 2.4: The relative difference between the FH and MD phase densities at one of the cells, when $\alpha^*, \beta^* = 2$

Graphs in Fig. 2.4, Fig. 2.5, and Fig. 2.6 demonstrate different trends when the parameters α^* and β^* are increased. That means α^* and β^* values cannot be ignored and must be assessed every time when applied to a different interaction potential.

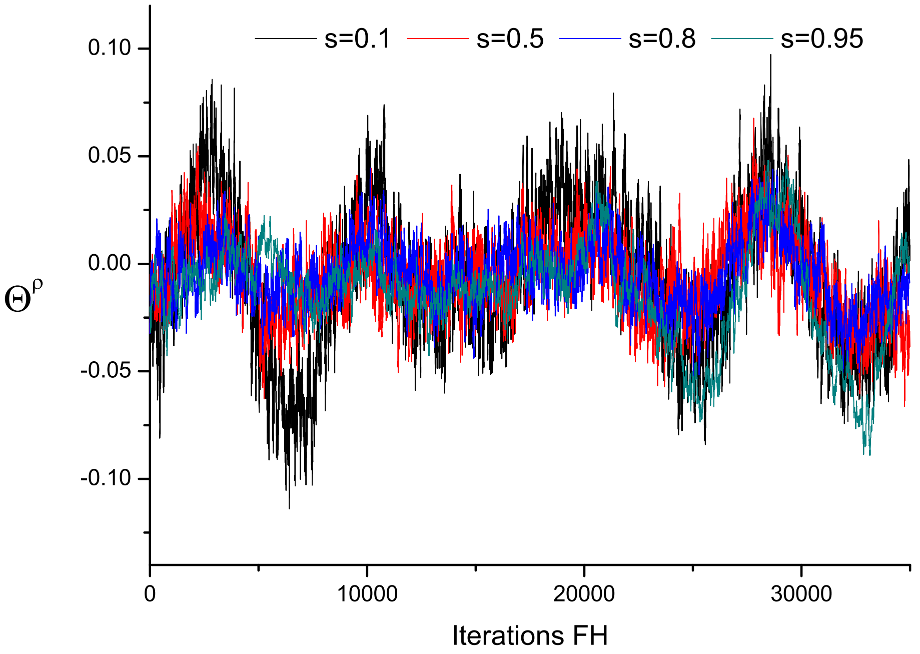

Figure 2.5: The relative difference between the FH and MD phase densities at one of the cells, when $\alpha^*, \beta^* = 1000$

Fig. 2.4 and Fig. 2.7 show that stability of simulation for $\alpha^*, \beta^* = 2$ is jeopardised, when $s = 0.95$.

In this case interaction between the MD particles is scaled with the $(1-s)$ and the main contribution to (2.42) and (2.43) is form the FH phase. The time lapse in the FH and MD phase is different, hence the FH phase terms in (2.42) and (2.43) are constant for a certain period of time (dt_{FH}/dt_{MD} timesteps). Consequently, the MD particles can get accumulated in some cells, regardless the difference between the phase densities and momentum, which are not the dominant terms when α^*, β^* are small. Due to the constant number of MD particles some cells become empty. This inconsistency leads to the high MD phase fluctuations and at some point MD particles can get too close to each other to result in the strong repulsion, which jeopardises stability of the simulation.

When values of α^*, β^* are small the expected behaviour of the MD phase is not observed. That means that the MD phase fluctuations were not able to mimic the FH phase. Even when α^*, β^* were increased to 1000, Fig. 2.5 and Fig. 2.8 show that the correlation between the MD and FH phase density and velocity fluctuations was not substantially enhanced.

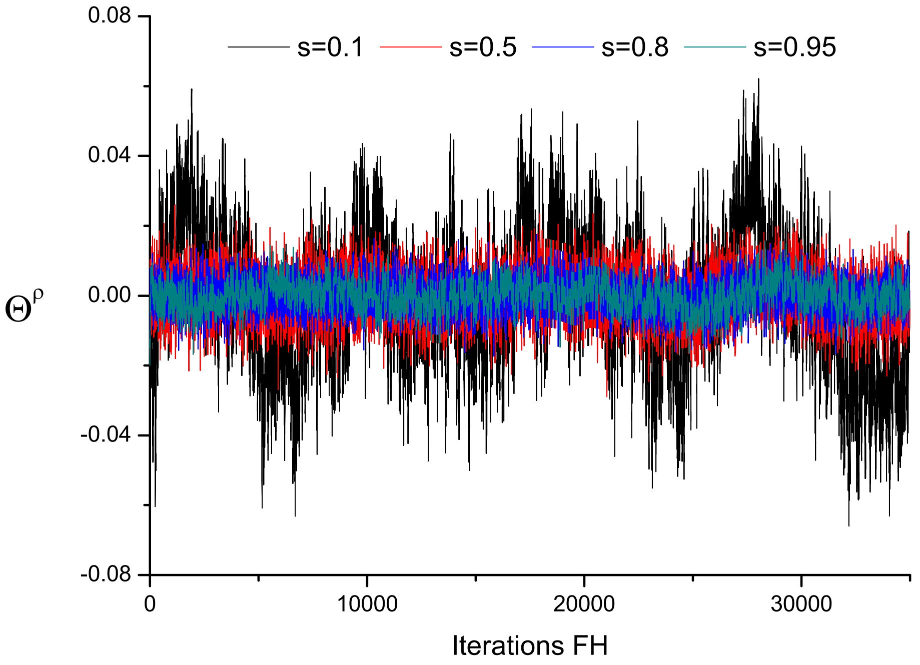

Figure 2.6: The relative difference between the FH and MD phase densities at one of the cells, when $\alpha^*, \beta^* = 20000$

Further increase of α^*, β^* demonstrates better results, especially for the higher s values. In this case the MD phase density fluctuations more and more resemble the FH phase density fluctuations, the same conclusion is made for the velocities.

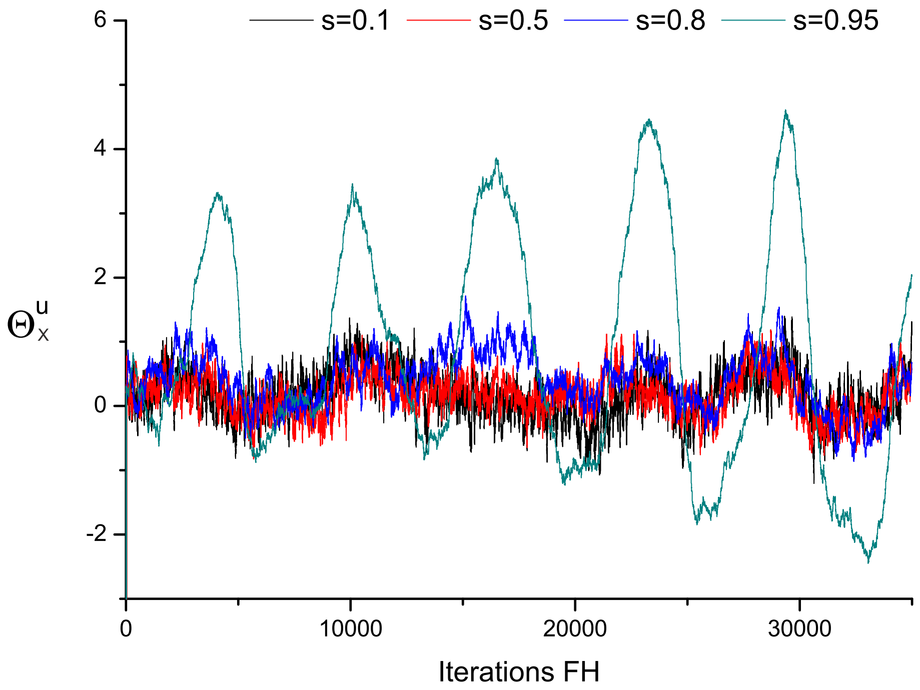

Figure 2.7: The relative difference between the FH and MD phase velocities (x component) at one of the cells, when $\alpha^*, \beta^* = 2$

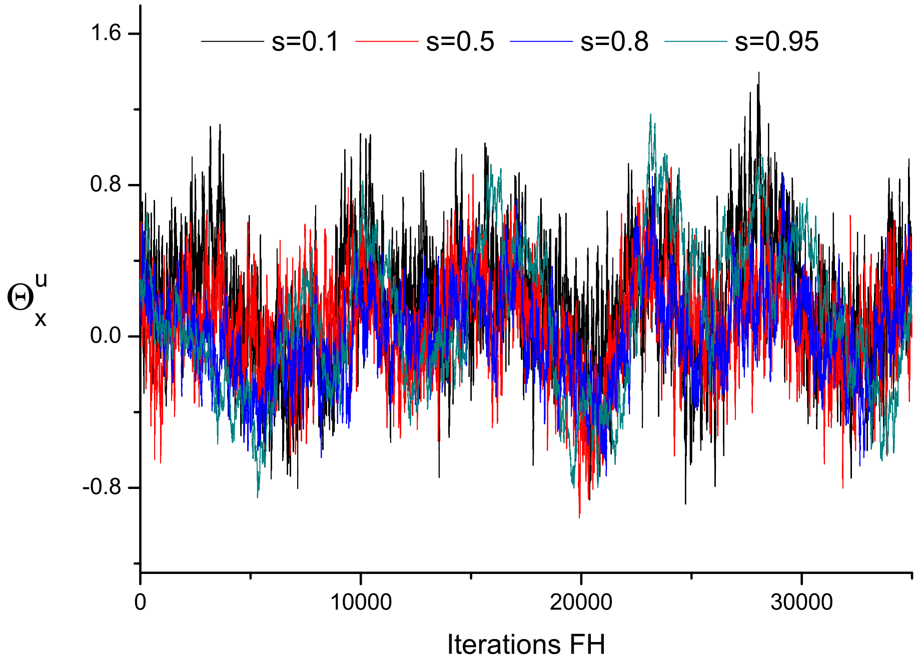

Figure 2.8: The relative difference between the FH and MD phase velocities (x component) at one of the cells, when $\alpha^*, \beta^* = 1000$

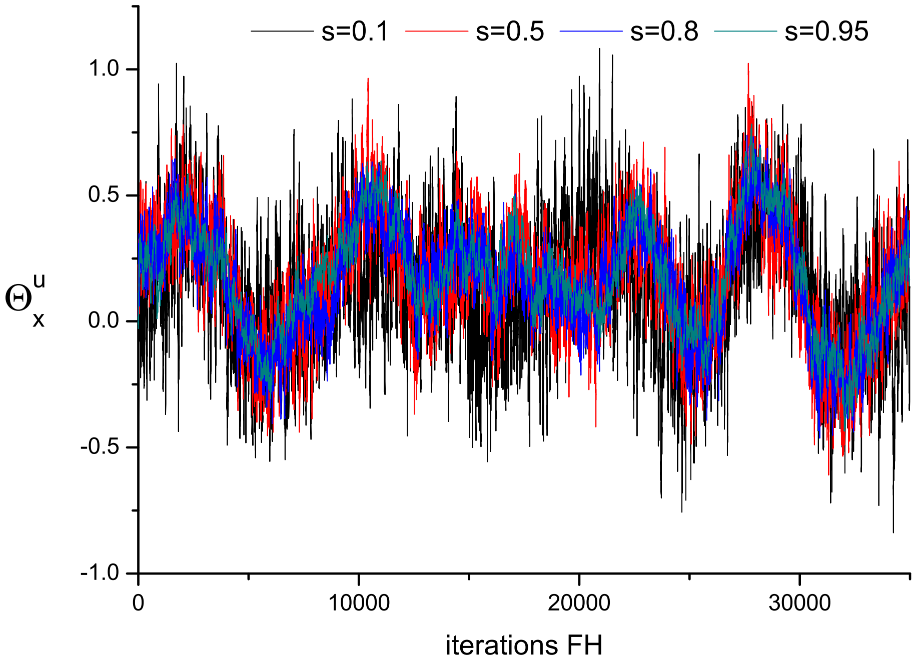

Figure 2.9: The relative difference between the FH and MD phase velocities (x component) at one of the cells, when $\alpha^*, \beta^* = 20000$

Fig. 2.7 illustrates unusually high fluctuations of the MD phase velocities, when $s = 0.95$ ($\alpha^*, \beta^* = 2$) that eventually will cause the simulation to crash. The peaks of these fluctuations coincide with the ones for $s < 0.95$. Furthermore, increase of α^*, β^* to 1000, Fig. 2.8, maintains the stability and expected MD phase fluctuations. Further increase of α^*, β^* to 20000, Fig. 2.9, improves stability and yields desired MD phase fluctuations Fig. 2.10.

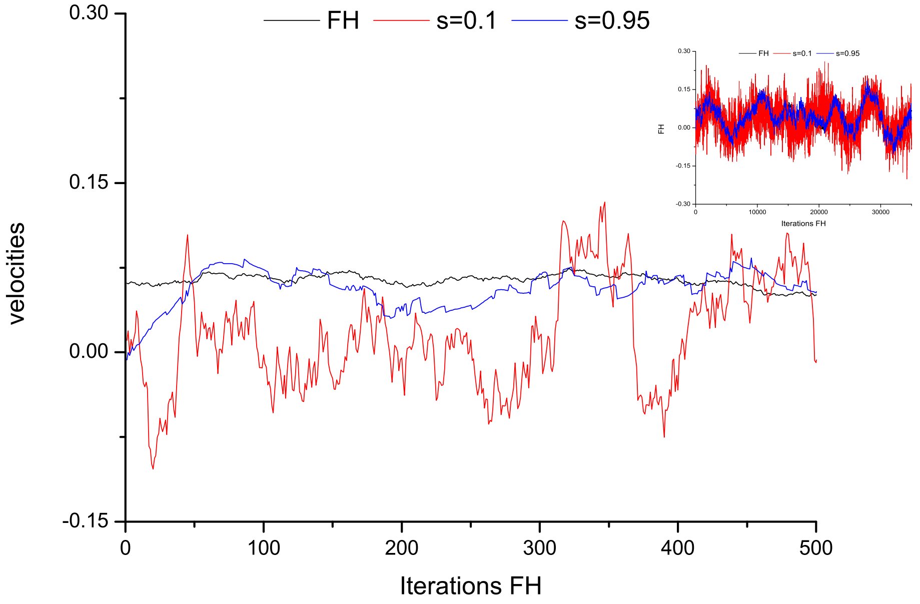

Figure 2.10: Velocity fluctuations of the FH phase u_x and MD phase $\sum_p u_{xp}$, when $\alpha^*, \beta^* = 20000$ and different coupling parameter s values; 'one way' coupling of 2D argon

In order to eliminate conditions that cause the divergence of the velocities and densities, a set of simulations were conducted and presented in Table. 2.3 and Table. 2.4. These tables show how the standard deviation of the phase differences $\rho - \sum_p \rho_p$ and $u_x - \sum_p u_{xp}$ are changing with α^*, β^* and parameter s.

α^*	β^*	**s = 0.1**	**s = 0.5**	**s = 0.8**	**s = 0.95**
2	**2**	0.021	0.019	0.024	0.045
1000	**2**	0.018	0.012	0.011	0.015
20000	**2**	0.012	0.004	0.003	0.003
2	**1000**	0.021	0.021	0.035	0.076
1000	**1000**	0.020	0.011	0.009	0.014
20000	**1000**	0.012	0.004	0.003	0.003
2	**20000**	0.020	0.065	–	–
1000	**20000**	0.019	0.011	0.010	0.017
20000	**20000**	0.012	0.004	0.003	0.003

Table 2.3: The standard deviations of $\rho - \sum_p \rho_p$, for different α^*, β^* and s, ("-" unstable simulation); The standard deviation was calculated using 34000 FH iterations

α^*	β^*	**s = 0.1**	**s = 0.5**	**s = 0.8**	**s = 0.95**
2	**2**	0.090	0.077	0.103	0.431
1000	**2**	0.088	0.085	0.103	0.185
20000	**2**	0.088	0.125	0.175	0.214
2	**1000**	0.080	0.060	0.074	0.194
1000	**1000**	0.077	0.061	0.059	0.095
20000	**1000**	0.086	0.089	0.075	0.125
2	**20000**	0.059	0.032	–	–
1000	**20000**	0.059	0.027	0.022	0.021
20000	**20000**	0.062	0.033	0.022	0.021

Table 2.4: The standard deviations of $u_x - \sum_p u_{xp}$ for different α^*, β^* and s, ("-" unstable simulation); The standard deviation was calculated using 34000 FH iterations

One can argue, that the fluctuations of pure FH and MD phases as well as coupled systems are not compatible, hence the figures above are not representable. Thus we obtained the standard deviations for the pure MD and FH phases as well as coupled systems MD phase, Fig. 2.11 and Fig. 2.12.

Fig. 2.11 and Fig. 2.12 show that the standard deviations (std) even after a short simulation time are close for all systems. For a longer time *std* values are expected to converge to the same value. It is also believed that for the pure MD phase *std* has higher values due to the pulsations of the MD phase, which appear when particle migrates from one cell to another. This effect can be eliminated if 'blob' filter is used [1]. At this moment these pulsations are not critical and their elimination using 'blob' is presented in Section 3.3, where SPC/E water model is considered.

Overall the fluctuations are believed to be correct and compatible for all systems.

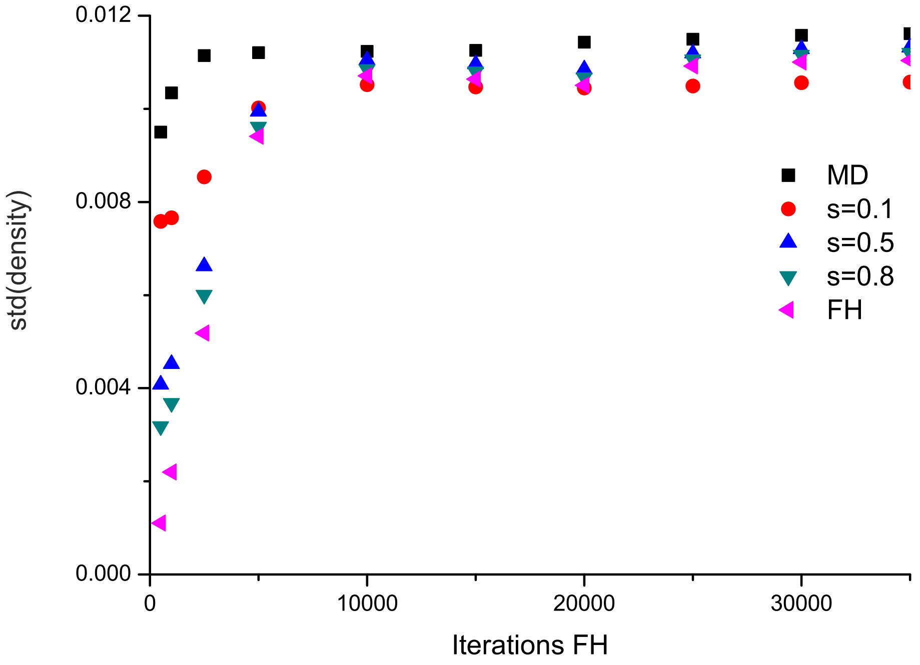

Figure 2.11: The standard deviation of density of the coupled system $\tilde{\rho}$, when $\alpha^*, \beta^* = 20000$, pure FH phase ρ and MD phase $\sum_p \rho_p$

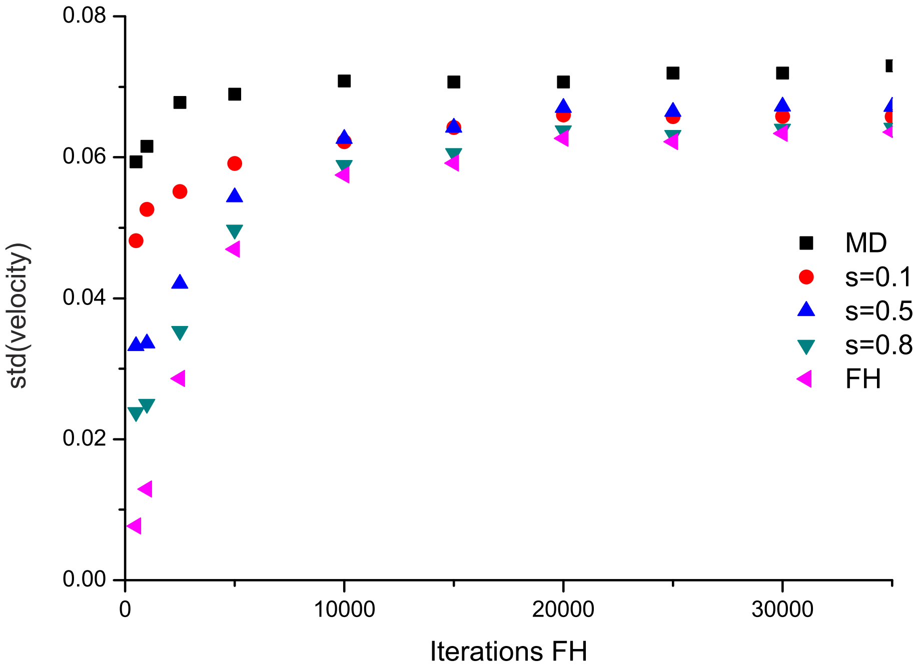

Figure 2.12: The standard deviation of the velocity's x component of the coupled system $\tilde{u}$, when $\alpha^*, \beta^* = 20000$, pure FH phase u_x and MD phase $\sum_p u_{xp}$

Standard deviations presented in Table. 2.3 and Table. 2.4 show that the coupling effect is recovered if α^* exceeds 1000, and β^* is in the region of 20000. Since the contribution of the terms with α^*, β^* become sufficient enough to match densities and momentum between phases.

When α^* is less than 1000, regardless the value of β^* the simulation becomes unstable, although the effect of coupling is more prominent, if β^* is in the region of 20000.

Other observation of the standard deviations dependence on the parameters α^*, β^*, Table.2.3 and Table.2.4 shows, that α^* mostly affects density fluctuations, while β^* is largely involved in the momentum fluctuations.

2.3.6 Structure and Dynamics of the liquid

Structural peculiarities or close order change due to the coupling was not observed Fig. 2.13. For all simulations the Radial Distribution Function (RDF) is the same.

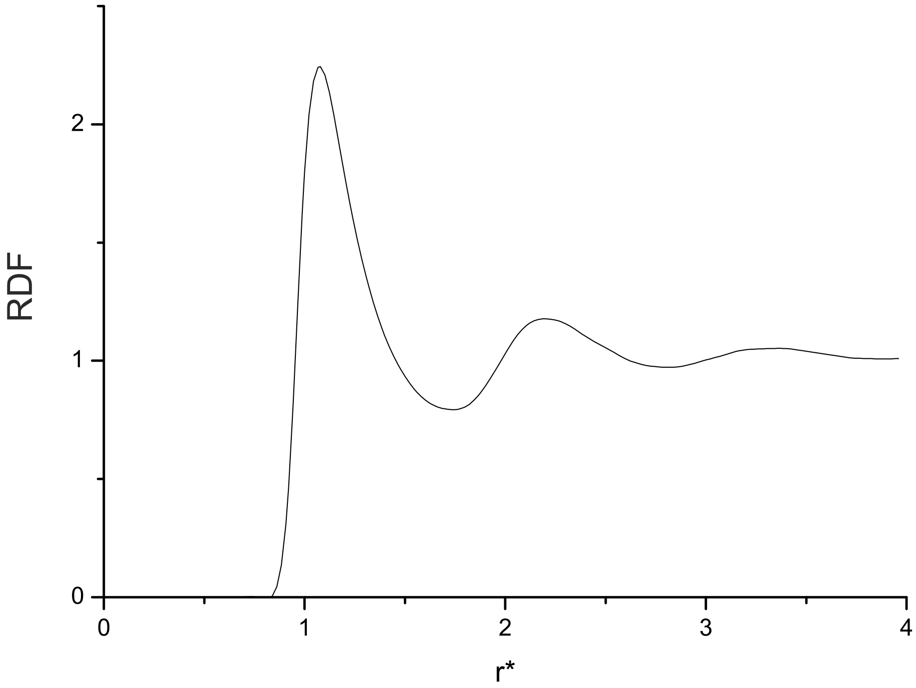

Figure 2.13: The radial distribution functions of 2D liquid argon in the case of 'one way' coupling are the same for all *s*, α^* and β^*

Contrary, the velocity autocorrelation functions (VACF) showed substantial difference when coupling was used. We calculated VACFs using MD particles velocities (2.42) and for the FH phase data from 25 cells was evaluated.

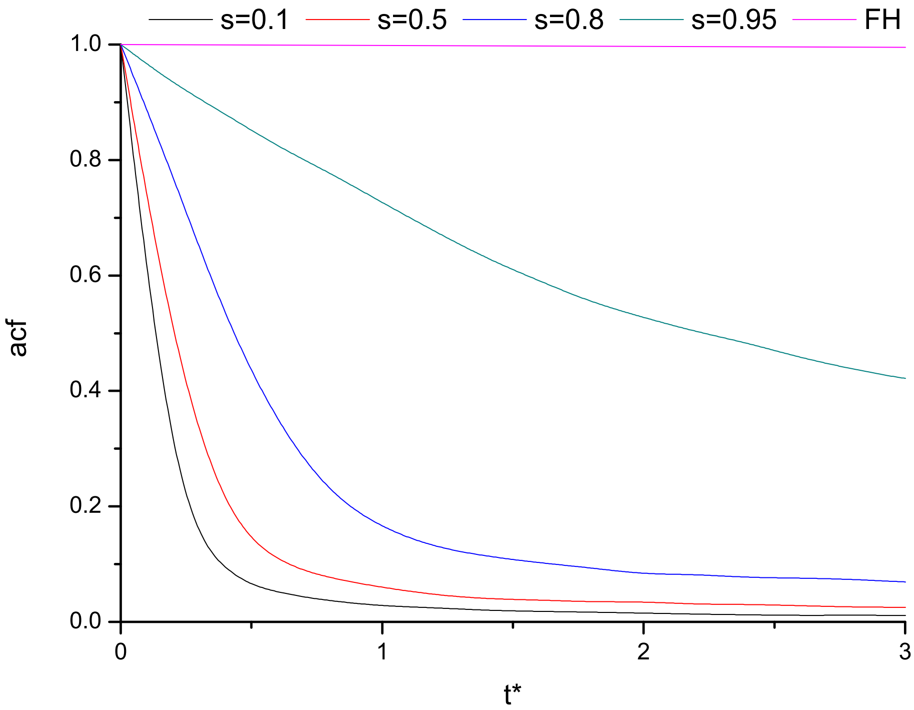

Figure 2.14: MD particles velocity autocorrelation functions for $\alpha^*, \beta^* = 20000$

The estimation of VACF, when simulation lacks stability or does not provide with the expected coupling effect is not of great interest, hence VACF of the most meaningful case ($\alpha^*, \beta^* = 20000$) is shown in Fig. 2.14. Normally VACF in the case of LJ potential would rapidly fall to zero, however here with the increase of the parameter s the correlation functions are stretched along the time axis. That means that the correlation between MD particles exists for a longer time period. These trends are possible if particles are in commotion, that could be caused by an external force field. Thus, the coupling method creates the external forcefield, that affects MD particles motion. On the other hand, the linear interpolation used between the cell centres can also impose additional correlation between MD particles. Unfortunately, the interpolation cannot be eliminated, since the MD and FH phase properties are available only at the cell centers.

Summarizing, we have successfully tested the new equations of motion and demonstrated the coupling effect between the MD and FH phases. We established the one way communication between phases as well as calibrated α^* and β^* parameters for the 2D Lennard-Jones potential.

2.4 ‘Two way’ coupling

In the previous section we demonstrated, that (2.42) and (2.43) impose the FH phase fluctuations on the MD phase, when the communication between these phases is accomplished in the ‘one way’ coupling, no feedback is given to the FH phase. No both way communication was implemented before, hence MD phase was unable to affect the FH phase, leading to an incomplete communication. The next step is to use a feedback routine, from the MD to the FH phase, that is essential for the successful communication between the phases.

This communication can be applied through (2.4) and (2.15), instead of using the equations of the standard LL-FH simulation for the FH phase. Hence, the coupling parameters such as α^*, β^* obtained in the 'one way' coupling may not be applicable now, therefore re-evaluations of these parameters is required.

Apart from the different equation sets for the FH and MD phases, information exchange between them must be described in details as well. The exchange of information or fluctuations between the FH and MD phase was partially solved in the 'one way' coupling, although the effect of the MD phase on the FH phase fluctuations must be considered now.

The information exchange between the phases is illustrated in Algorithm. 3. First, the standard LL-FH and MD simulations are implemented, thus, each phase is equilibrated for the same conditions, Table. 2.2. Then, like in the 'one way' coupling, as time in the MD simulation is not equal to the time passed in the FH simulation, the FH phase fluctuations are imposed on the MD particles. In other words, if the timestep in modified LL-FH simulation is, for example, $dt^*_{FH} = 0.05$ and in the MD simulation, $dt^*_{MD} = 0.005$, then the MD particles are advanced using (2.42) and (2.54) for 10 iterations before the exchange of the data between the phases in undertaken.

When the 10th MD iteration is reached the modified LL-FH equations (2.4) and (2.15) are solved using the definitions in (2.9), (2.18), where L^ρ is defined as (2.40) and L^u as (2.53). This will amend the FH phase density and momentum fluctuations, compared to the standard LL-FH simulation. Essentially, this procedure updates the FH phase fluctuations for the next time layer, that will be used in the MD simulation.

Algorithm 3: Pseudo code for the ‘two way’ coupling

```
Data: equilibrate the FH and MD phases (standard LL-FH and MD simulations);
calculate $\sum_p \rho_p$ and $\sum_p \rho_p u_{ip}$ in the cell centres;
for $n \leq$ simulation time do
    if $n = dt_{HD}/dt_{MD}$ then
        run LL-FH simulation using modified equations (2.4) and (2.15) for the FH phase;
    else
        run MD simulation using modified equations of motion (2.42) and (2.43);
        calculate $\sum_p \rho_p$ and $\sum_p \rho_p u_{ip}$ in the cell centres;
    end
    exchange data;
end
```

2.4.1 FH phase

According to Algorithm. 3, the MD phase density $\sum_p \rho_p$ and momentum $\sum_p \rho_p u_{ip}$ are known from the MD simulation. The FH phase is obtained with the modified LL-FH simulation, where the following notations are used

$$\rho' = \tilde{\rho} - \sum_p \rho_p, \tag{2.47}$$

$$\rho' u'_j = \tilde{\rho}\tilde{u}_j - \sum_p \rho_p u_{jp}, \tag{2.48}$$

where ρ' and $\rho' u'_j$ are the differences between the mixture (the MD and FH phase mixture in the overlap-region) and the MD phase density and momentum respectively. These new variables can also be denoted as perturbations of density and momentum.

Modified LL-FH equations are given by the new mass conservation equation

$$\frac{\partial}{\partial t}\rho' + \frac{\partial}{\partial x_i}\tilde{u}_i\rho' = Q_\rho, \tag{2.49}$$

where

$$Q_\rho = \frac{\partial}{\partial x_i}\left[s\,(1-s)\,\alpha\frac{\partial \rho'}{\partial x_i}\right], \tag{2.50}$$

followed by a new momentum conservation equation

$$\frac{\partial}{\partial t}u'_j\rho' + \frac{\partial}{\partial x_i}\tilde{u}_i u'_j\rho' = sF_j + Q_u, \tag{2.51}$$

where

$$Q_u = \frac{\partial}{\partial x_j}\left[s(1-s)\beta\frac{\partial}{\partial x_j}\left(u'_j\rho'\right)\right]. \tag{2.52}$$

The FH force (per volume) F_j is defined in the same manner as in the standard LL-FH simulation

$$F_j = \nabla_j\left(\Pi_{ij}+\tilde{\Pi}_{ij}\right).$$

In distinction from the 'one way' coupling, the 'two way' coupling instead of the standard LL-FH simulation uses the modified equations (2.49) and (2.51). These equations are solved using the operator splitting technique and second-order centred finite-difference scheme CABARET, that already was successfully implemented for the standard LL-FH simulation.

According to the operator splitting technique, equations (2.49) and (2.51) yield Riemann invariants ρ' and $\rho'u'$ with the characteristic speeds $\lambda_{1,2} = \tilde{u}$. (for detailed derivations see Appendix A.3).

An additional step in the CABARET numerical scheme is introduced, such that Q_0 and Q_u are applied at the corrector step, when the next time layer $n+1$ is evaluated in Algorithm. 1.

2.4.2 MD phase

The MD phase is obtained in the similar way, using the same L^ρ operator type

$$L^\rho\cdot\left(\tilde{\rho}-\sum_p\rho_p\right) = \frac{\partial}{\partial x_i}\left[s(1-s)\alpha\frac{\partial}{\partial x_i}\left(\tilde{\rho}-\sum_p\rho_p\right)\right],$$

although for the momentum exchange rate operator is different:

$$L^u\cdot\left(\tilde{u_j}\tilde{\rho}-\sum_p\rho_p u_{jp}\right) = \frac{\partial}{\partial x_j}\left[s(1-s)\beta\frac{\partial}{\partial x_j}\left(\tilde{u_j}\tilde{\rho}-\sum_p\rho_p u_{jp}\right)\right]+sF_j. \tag{2.53}$$

The presence of the FH force (per volume) F_j in the definition of the operator L^u is a matter of convenience, leading to the FH force to remain in the momentum conservation equation of the FH phase, (2.15). Thus, at the limit $s = 1$ we recover standard LL-FH model/simulation. Notably, in the 'one way' coupling case the F_j force was incorporated in the MD particles equations of motion (2.43).

According to (2.13) and (2.23) as well as the definitions of the L^ρ and L^u operators above, the new velocities of the MD particles are given by

$$\frac{dx_{ip}}{dt} = u_{ip}+s(\tilde{u}_i-u_{ip})+s(1-s)\alpha(x)\frac{1}{\rho_p N(t)}\frac{\partial}{\partial x_i}\left(\tilde{\rho}-\sum_p\rho_p\right),$$

and the new accelerations of the individual particle become

$$\frac{\partial u^N_{jp}}{\partial t} = (1-s)\frac{F_{jp}}{\rho_p V_{cell}} + \frac{1}{\rho_p N(t)} \times \tag{2.54}$$

$$\times \left[\frac{\partial}{\partial x_i}\left(s(1-s)\alpha(x)\frac{\partial}{\partial x_i}\left(\tilde{\rho} - \sum_p \rho_p\right)\right)\frac{\sum_p u_{jp}}{N(t)} - \frac{\partial}{\partial x_i}\left(s(1-s)\beta(x)\frac{\partial}{\partial x_i}\left(\tilde{u_j}\tilde{\rho} - \sum_p \rho_p u_{jp}\right)\right)\right].$$

Equations above show that, we recover pure MD equations of motion when $s = 0$. When $s = 1$ MD particles accelerations become zero and their velocities are equal to the FH phase velocity. Thus, in the case $s = 1$ 'static structure' of MD particles is moving with the FH phase flow. At the limit $s = 0$ or $s = 1$ contribution from the terms $\tilde{\rho} - \sum_p \rho_p$ and $\tilde{u_j}\tilde{\rho} - \sum_p \rho_p u_{jp}$ becomes zero, that means either the MD or FH phase does not exist and there is no reference for the MD phase to be driven to. The same behaviour is in the case of the 'one way' coupling, where accelerations are proportional to the FH phase force which alters MD particles velocities, that are later disregarded in the particles position update.

2.4.3 Simulation

Summarizing, the equations of motion of the MD phase are similar to the 'one way' coupling, (2.42) and (2.43), with the only difference that the FH force term F_j is absent in (2.54).

For the FH phase, instead of the standard LL-FH simulation equations (2.4) and (2.15) are used. We expect that the new equations for the FH phase will impose changes on the FH phase fluctuations due to the presence of the MD phase. The strength of this effect is partially defined by the parameters α^* and β^*, that must be re-evaluated, since they were not calibrated for this particular case.

Overall, we expect the 'two way' coupling to be more effective comparing to the 'one way' coupling, considering that the effectiveness is measured as an ability to communicate between the phases.

The simulations were conducted using the same LJ model parameters, Table. 2.1, and conditions, Table. 2.2, as in the 'one way' coupling , although the coupling parameters α^*, β^* were set to $2/50/1000$.

2.4.4 Stability analysis

The 'two way' coupling analysis is slightly different, because now the FH phase is affected by the MD phase fluctuations.

Like in the 'one way' coupling we encountered stability issues when, $\alpha^*, \beta^* = 2$, leading to the unusually hight fluctuations of densities and velocities. These fluctuations could not be avoided even with the velocity rescaling, that was used in simulations to reduce the effect of rounding and cut-off errors for a long run.

The standard deviations of all sets of simulations, when the stability was maintained ($\alpha^*, \beta^* > 2$), produced similar magnitudes of fluctuating variable as in Fig. 2.12. This observation shows the consistency between the phase fluctuations, from the statistical point of view.

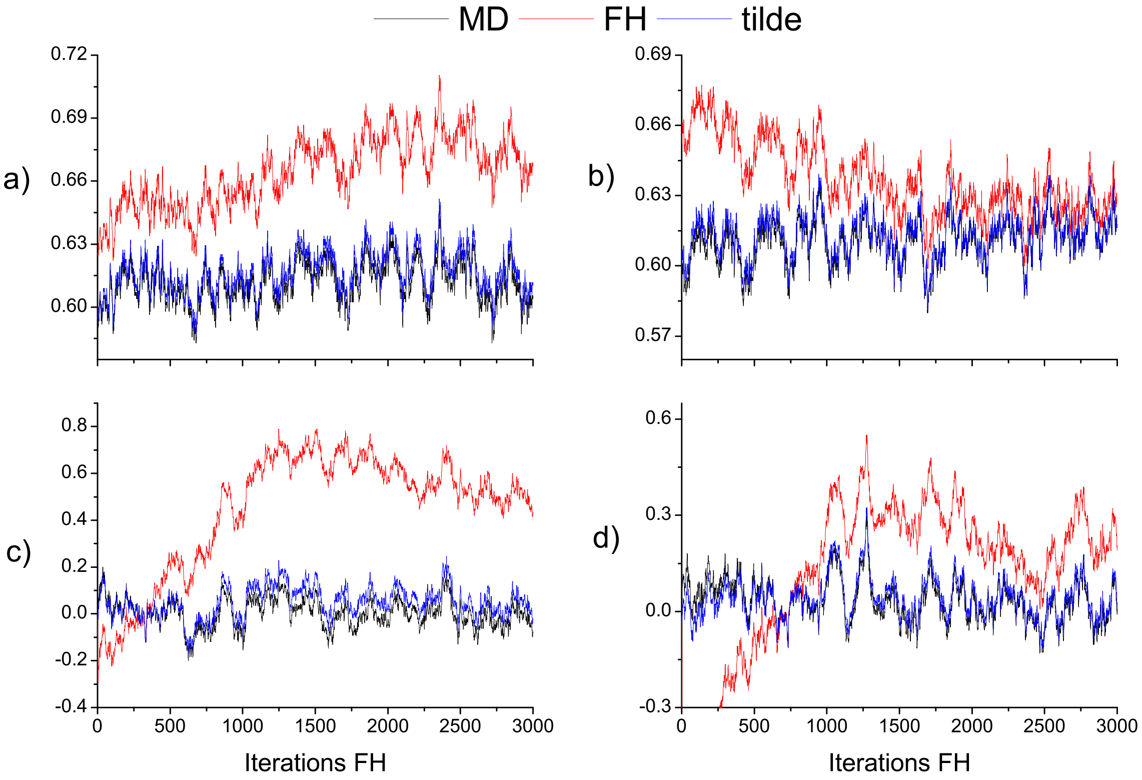

Figure 2.15: The density and velocity fluctuations of the mixture (denoted by tilde), of the MD and FH phases in a random cell; the case of 'two way' coupling of 2D liquid argon; parameter $s = 0.1$; a) corresponds to the density and c) velocity x component, when $\alpha^* = 2$, $\beta^* = 50$; b) corresponds to the density and d) velocity x component, when $\alpha^* = 50$, $\beta^* = 50$

Furthermore, regardless the values of α^*, β^* or parameter s Fig. 2.15 and Fig. 2.16, the densities of each phase as well as the velocities are always correlated. As if both phases were in commotion in each cell.

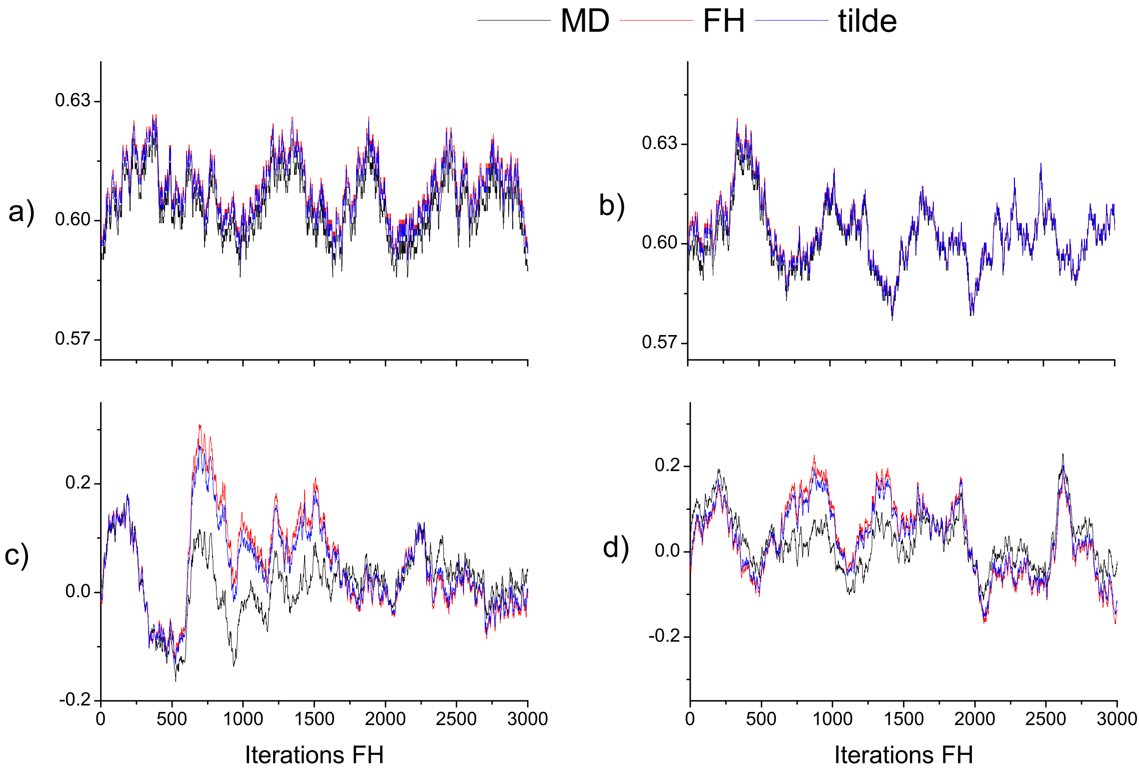

Figure 2.16: The density and velocity fluctuations of the mixture (denoted by tilde), of the MD and FH phases in a random cell; the case of ‘two way’ coupling of 2D liquid argon; parameter $s = 0.8$; a) corresponds to the density and c) velocity x component, when $\alpha^* = 2$, $\beta^* = 50$; b) corresponds to the density and d) velocity x component, when $\alpha^* = 50$, $\beta^* = 50$

When s is large ($s = 0.8$), Fig. 2.16, it can be seen that the density and velocity fluctuations of the MD phase are almost the same as of the FH phase. Contrary, when s is small ($s = 0.1$), Fig. 2.15, these fluctuations are not close, this observation leads to the conclusion that the FH phase is more inert (heavy) than the MD phase, thus less effort is needed to get the MD phase into the FH phase state, rather than the FH phase into the MD phase state.

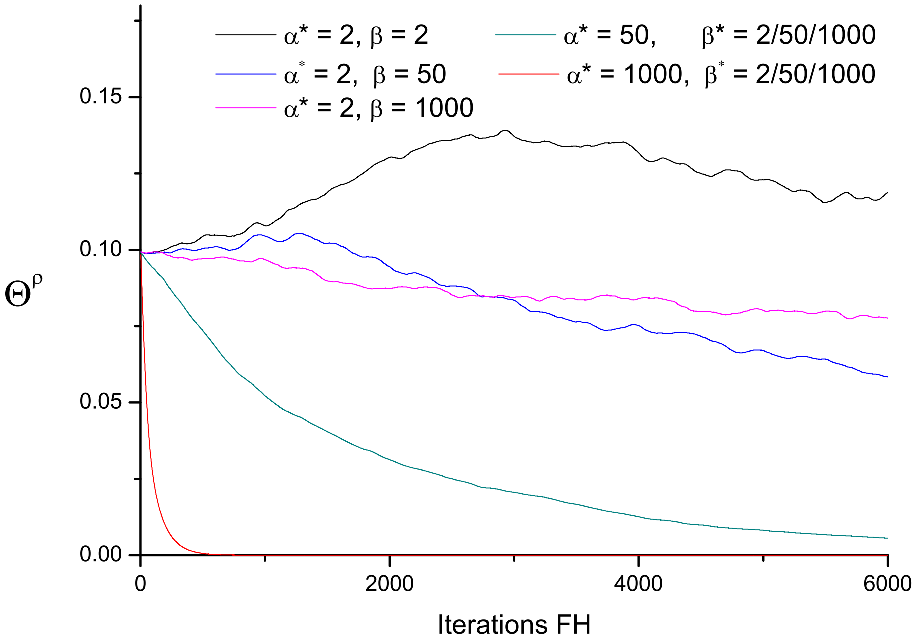

Figure 2.17: The relative difference between the FH and MD phase densities if $s = 0.1$ in the case of 'two way' coupling of 2D liquid argon; single plots are depicted for all sets of β^*, when $\alpha^* = 50$ and $\alpha^* = 1000$, due to the negligible difference between plots;

The choice of the parameters α^* and β^* defines the stability of simulation. Fig. 2.17 shows that with the increase of α^* the difference (relative) between the densities is driven to zero quicker. If α^* is chosen large, the phase densities will be rapidly equalized, when α^* is in a middle region ($\alpha^* = 50$), the difference (relative) between the phase densities gradually diminishes, though slower. For the small α^* values the stability issues are encountered, especially when $\alpha^*, \beta^* = 2$ the simulation crashes after certain period of time, hence for the rest sets of α^*, β^* stability was maintained.

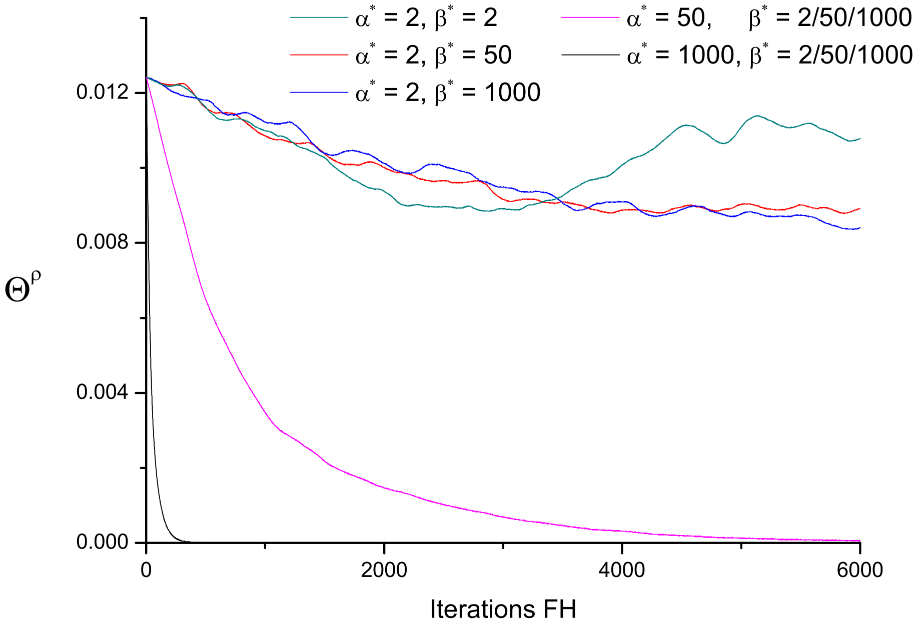

Figure 2.18: The relative difference between the FH and MD phase densities if $s = 0.8$ in the case of 'two way' coupling of 2D liquid argon; single plots are depicted for all sets of β^*, when $\alpha^* = 50$ and $\alpha^* = 1000$, due to the negligible difference between plots;

The effect of β^* on the density differences is negligible if $\alpha^* \geq 2$, thus we assume that α^* is an essential parameters for the communication between the phase densities. From the numerical perspective Fig. 2.17 and Fig. 2.18 show that one phase densities relax to another, and the rate of relaxation is mostly determined by the α^* parameter.

The choice of α^* must be such that the density relative difference Θ^ρ is monotonically decreasing function. For this particular case $\alpha^* \geq 50$.

Fig. 2.18 leads to the same conclusions, although in contrast with Fig. 2.17, the density difference (relative) magnitudes are smaller by an order, that is in agreement with our previous suggestion, that the MD phase is less inert, than the FH phase.

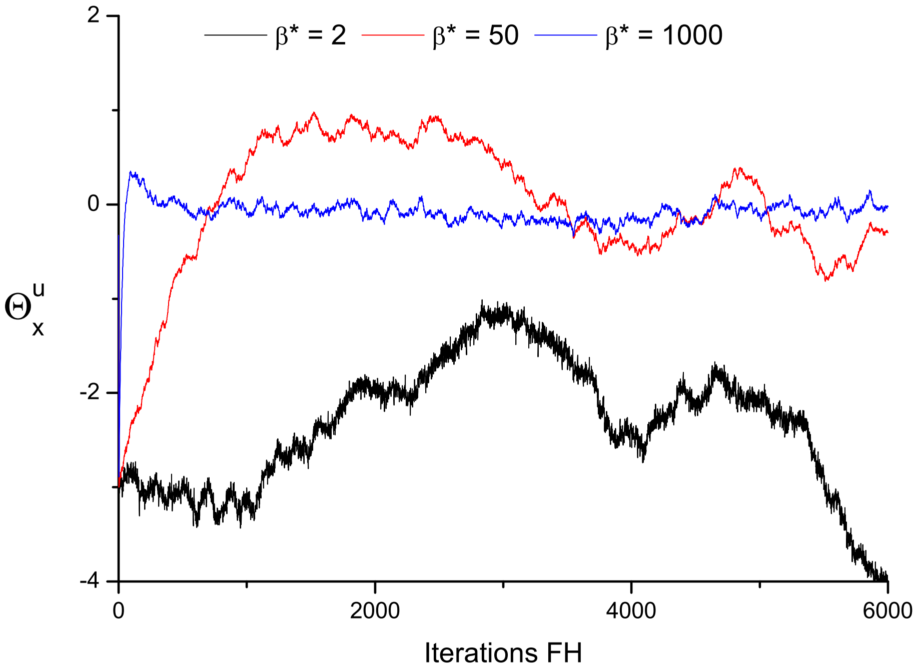

Figure 2.19: The relative difference between the FH and MD phase velocities when $s = 0.1$ and $\alpha^* = 2$; in the case of 'two way' coupling of 2D liquid argon

In the 'one way' coupling case we suggested that α^* and β^* mostly affect densities and velocities respectively. We carried out a set of tests to verify if this is also true for the 'two way' coupling.

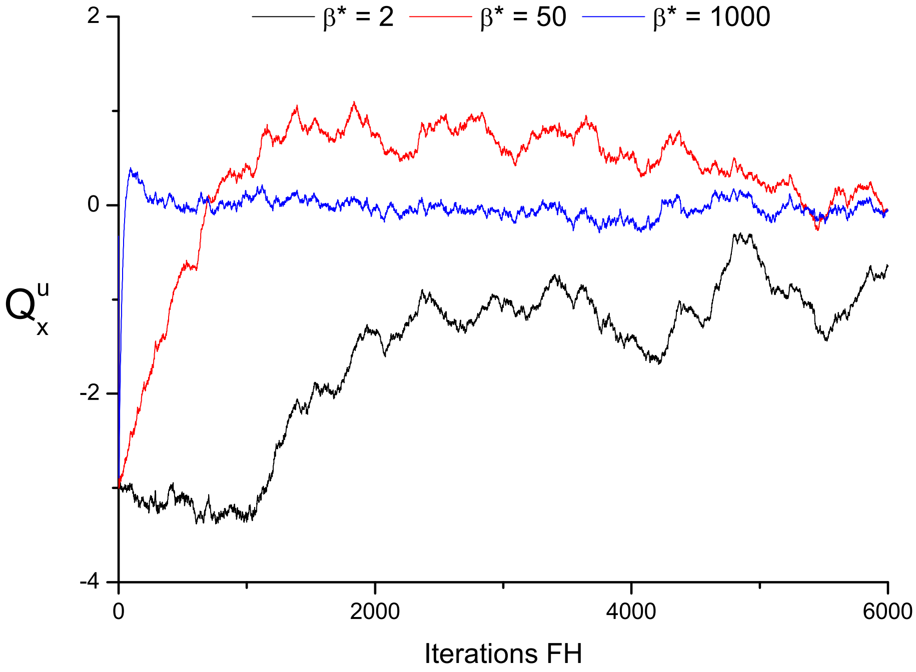

Figure 2.20: The relative difference between the FH and MD phase velocities when $s = 0.1$ and $\alpha^* = 1000$; in the case of 'two way' coupling of 2D liquid argon

Fig. 2.17, Fig. 2.18, Fig. 2.19, Fig. 2.21, Fig. 2.20 and Fig. 2.22 show that β^* parameter contribution to the density fluctuations must be considered when α^* values are small. And parameter

α^* contribution to the velocity fluctuations should not be accounted for large β^* values, regardless the value of s.

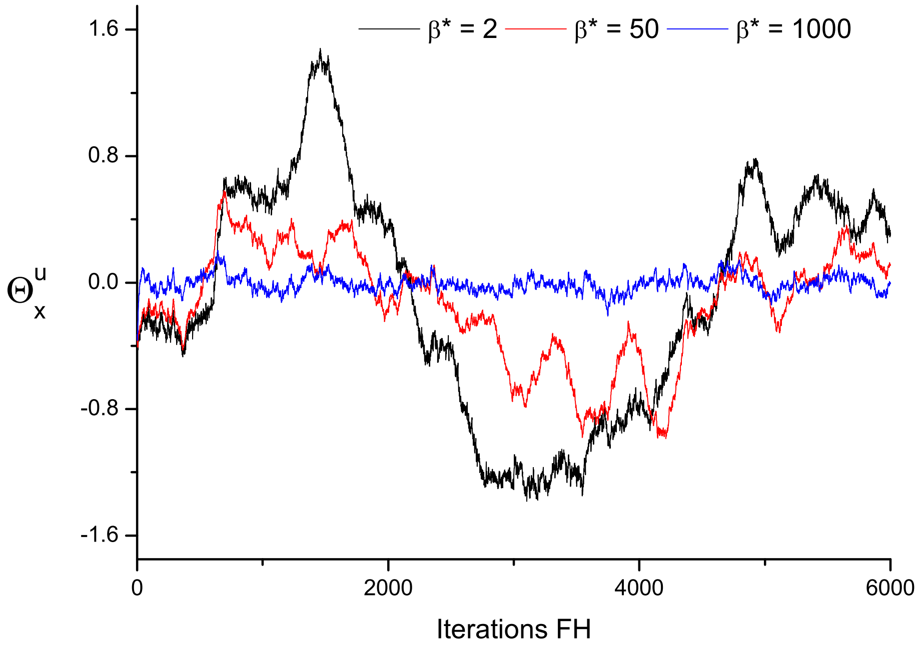

Figure 2.21: The relative difference between the FH and MD phase velocities when $s = 0.8$ and $\alpha^* = 2$; in the case of 'two way' coupling of 2D liquid argon

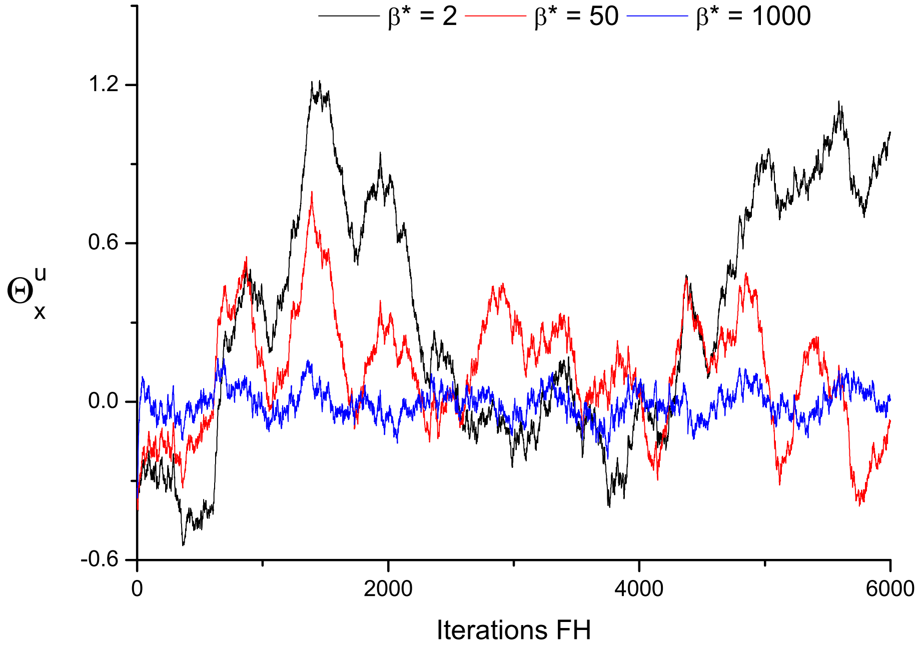

Figure 2.22: The relative difference between the FH and MD phase velocities when $s = 0.8$ and $\alpha^* = 1000$; in the case of 'two way' coupling of 2D liquid argon

2.4.5 Structure and Dynamics of the liquid

We investigated the dynamical and structural properties in order to detect artifacts or other undesirable effects.

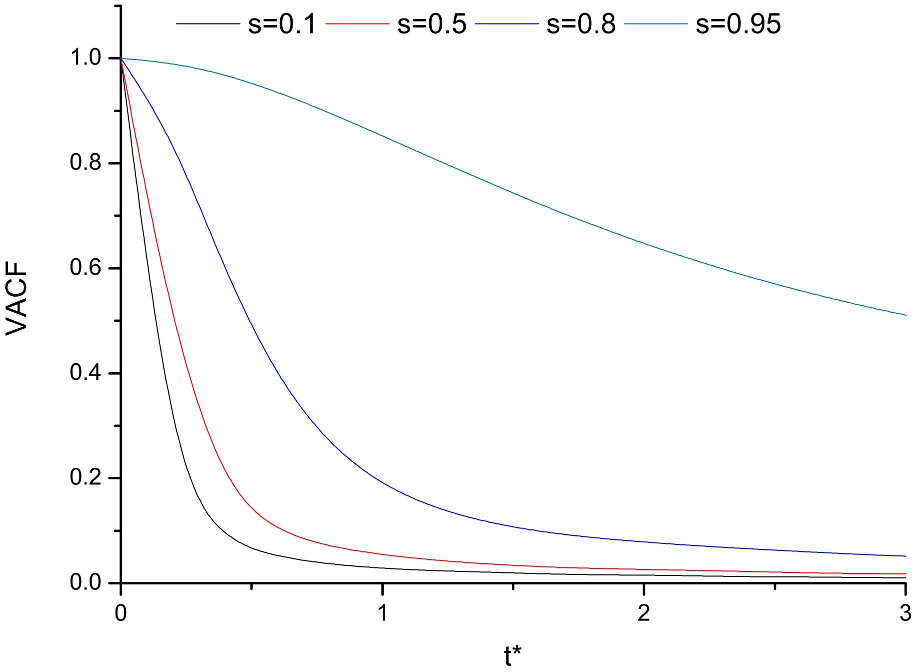

Figure 2.23: MD particles velocity autocorrelation functions for $\alpha^*, \beta^* = 50$; in the case of ‘two way’ coupling of 2D liquid argon

Fig. 2.23 shows that VACF trends are similar to the ‘one way’ coupling, with the increase of the parameter s VACF curve stretches, that can be explained as MD particles are experiencing collective motion in the external force field, that drags particles in a certain direction. Notably, the stretching effect is not related to the time rate difference in MD and LL-FH simulation, since temperature remains close to the set value. All VACFs for a particular s value are the same, Fig. 2.23, regardless the value of α^* and β^*.

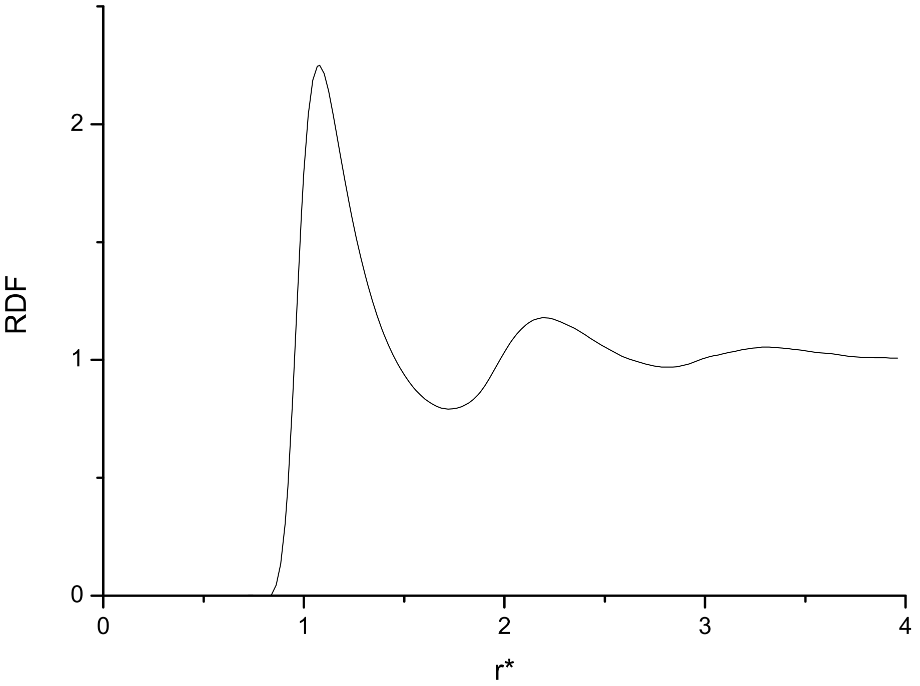

Figure 2.24: Radial distribution function of 2D liquid argon is in the case of ‘two way’ coupling

We obtained the same RDF for all sets of α^* and β^*. Fig. 2.24 illustrates that close order between MD particles is not affected by the ‘two way’ coupling and in both coupling cases is the same as for the 2D liquid argon, when coupling is not used.

Summarizing, for large values of the parameter s the MD phase fluctuations resemble the FH phase and, opposite, when s is small the FH phase fluctuates similarly to the MD phase. Thus, the communication between the FH and MD phases was successfully established, if $\alpha^*, \beta^* \geq 50$, when 2D Lennard-Jones potential is used.

2.5 Total energy rescaling

We assumed that the coupled system’s energy conservation equation decouples from the mass and momentum conservation equations, since adiabatic systems are studied. It is important to verify if only numerical errors (such as rounding and cut-off errors) were eliminated using velocity rescaling algorithm and no fundamental issues arise from the MD and FH phase coupling, that could lead to divergence of the total energy.

The energy conservation equation for the MD phase is not available, because energy in the MD simulations is conserved by definition, if the NVE ensemble is used.

Also for the FH phase simulation energy conservation equation was not solved due to the absence of the external sink/source of energy and adiabatic conditions of the system. Thus, the estimation of the balance between the total energies of the FH and MD phases is required.

This can be achieved by introducing a function $f(s(\vec{r}))$ which scales the total energy of the MD phase in the balance equation:

$$H_0 = (1-s)f(s(\vec{r}))(E_k^{MD} + \Phi^{MD}(\vec{r})) + s(E_k^{FH} + U^{FH}(V)), \tag{2.55}$$

where H_0 is the Hamiltonian of the coupled system, E_k is the kinetic energy with the superscript denoting the phase, $\Phi^{MD}(\vec{r})$ is the potential energy of the MD phase, $U^{FH}(V)$ is the internal energy of the FH phase and $f(s(\vec{r}))$ is assumed to be a linear function

$$f(s(\vec{r})) = 1 + \alpha_E(s(\vec{r})), \tag{2.56}$$

for simplicity the notation $\alpha_E = \alpha_E(s(\vec{r}))$ is used.

Note, that the MD phase density in the coupled system is close to the pure MD density and the MD phase contribution to the total energy of the coupled system is calculated according to the concentration $(1-s)$.

Equation (2.55) can be expressed in terms of the variables used in the previous simulations

$$H_0 = \sum_i (1-s(\vec{r}_i)) f(s(\vec{r})) \frac{\vec{p}_i^2}{2m_p} + \sum_i (1-s(\vec{r}_i)) f(s(\vec{r})) \sum_j \Phi_{ij}^{MD}(|\vec{r}_i - \vec{r}_j|) \tag{2.57}$$

$$+ \int_V s(\vec{r}) \frac{\rho^{FH}(\vec{r}) u^{FH}(\vec{r})^2}{2} d\vec{r} + \int_V s(\vec{r}) U^{FH}(\vec{r}) d\vec{r}, \tag{2.58}$$

where $\vec{p}_i = m_p \vec{u}_{ip}$ is the particle's momentum, ρ^{FH} and u^{FH} are the FH phase density and velocity respectively, the summation is taken over all MD particles and the integration is performed over the system's volume V.

The internal energy of the FH phase is assumed to be

$$U^{FH}(\vec{r}) = \frac{\overline{P}(\vec{r})}{(\gamma - 1)}, \tag{2.59}$$

where $\overline{P}(\vec{r})$ is the average pressure and γ is a constant.

The complete relationship between the available variables is obtained, after the substitution of $f(s(\vec{r}))$. The balance equation becomes

$$H_0 = \sum_i (1-s(\vec{r}_i))(1+\alpha_E) \frac{\vec{p}_i^2}{2m_p} + \sum_i (1-s(\vec{r}_i))(1+\alpha_E) \sum_j \Phi_{ij}^{MD}(|\vec{r}_i - \vec{r}_j|) \tag{2.60}$$

$$+ \int_V s(\vec{r}) \left(\frac{P^{FH}(\vec{r})}{\gamma - 1} + \frac{\rho^{FH}(\vec{r}) u^{FH}(\vec{r})^2}{2} \right) d\vec{r}. \tag{2.61}$$

The constant γ is unknown, although is can be determined if the limit case is considered. For example, when $s = 0$, H_0 is equal to the total energy of the pure MD phase, that can be obtained beforehand. H_0 is calculated using the classical formula

$$H_0 = E_{kin}^{MD} + E_{pot}^{MD}. \tag{2.62}$$

On the other hand, when $s = 1$, the Hamiltonian of the system is given by

$$H_0 = \int_V \left(\frac{P^{FH}(\vec{r})}{\gamma - 1} + \frac{\rho^{FH}(\vec{r}) u^{FH}(\vec{r})^2}{2} \right) d\vec{r}. \tag{2.63}$$

Substituting the value of H_0 obtained from the pure MD simulation into the equation above, γ can be recovered

$$\gamma = \frac{\overline{P}^{FH} V}{H_0 - \sum_i^N \left[\frac{\rho^{FH}(\vec{r}_i) v^{FH}(\vec{r}_i)^2}{2} \right] V/N} + 1. \tag{2.64}$$

Since all the necessary variables and constants are known α_E can be obtained using the following expression

$$\alpha_E = \frac{H_0 - \int_V s(\vec{r}) \left(\frac{P^{FH}(\vec{r})}{\gamma - 1} + \frac{\rho^{FH}(\vec{r}) v^{FH}(\vec{r})^2}{2} \right) d\vec{r}}{\sum_i (1 - s(\vec{r}_i)) \sum_j \, \Phi_{ij}^{MD}(|\vec{r}_i - \vec{r}_j|) + \sum_i (1 - s(\vec{r}_i)) \frac{\vec{p}_i^2}{2m_p}} - 1. \tag{2.65}$$

Equation (2.60) shows that the $f(s)$ function scales the MD phase kinetic and potential energy equally. This results in the following scaling of the interaction potential

$$\Phi_{ij}^{MD}(r) = (1 + \alpha_E) \cdot (\Phi_{ij}^{MD}(r))_{old}, \tag{2.66}$$

we assume α_E to be smoothly and slowly changing function, such that α_E scales the interaction forces between the MD particles as

$$F_{ij}^{MD} = -\frac{\partial \Phi_{ij}^{MD}}{\partial q} = (1 + \alpha_E)(F_{ij}^{MD})_{old}, \tag{2.67}$$

where q is the coordinate (x, y or z), subscript old stands for the unaltered/initial variable (value), before the energy rescaling was implemented.

The contribution of the scaling to the kinetic energy yields the following MD particle's velocity

$$u_{ip}^{MD} = \sqrt{1 + \alpha_E} \cdot (u_{ip}^{MD})_{old}. \tag{2.68}$$

Overall, α_E, that we introduced from the principles of total energy balance between the MD and FH phases, rescales the MD forces and velocities. Qualitatively, α_E variable presents moments when velocity rescaling is meant to be used.

2.5.1 Implementation

We implemented (2.65) with (2.67) and (2.68) to both coupling approaches, when liquid argon was studied.

The dimensionless pressure P^{FH} for each FH cell was derived from the Equation of State (EOS), that was obtained from the fitting of the experimental data [66] with a cubic polynomial

$$P^{FH}(\vec{r}) = \left(A(\rho^{FH}(\vec{r}) - B)^3 + C\right), \tag{2.69}$$

where A, B, C and $\rho^{FH}(\vec{r})$ are the dimensionless constants and the density of the FH phase.

We used the same EOS, (2.69), for all Lennard-Jones potential implementation cases.

The main benefit of the total energy rescaling is to specify if the imbalance between the MD and FH phases can be considered as a numerical imprecision.

Note, that when α_E correction is applied the velocity rescaling is not used.

Fig. 2.27 demonstrates that the total energy correction α_E randomly fluctuates around the zero value. Thus, no constant correction is required, that would be the case if fundamental artifacts were present. The magnitude of α_E shows that the correction is in the range of 0.2%. Essentially, the total energy is conserved, although numerical errors are present. The analysis of α_E standard deviations showed the reduction in the *std* value, when s is increased. This can be due to the slight disproportion between the total energy of the MD and FH phase. These deviations can be easily explained.

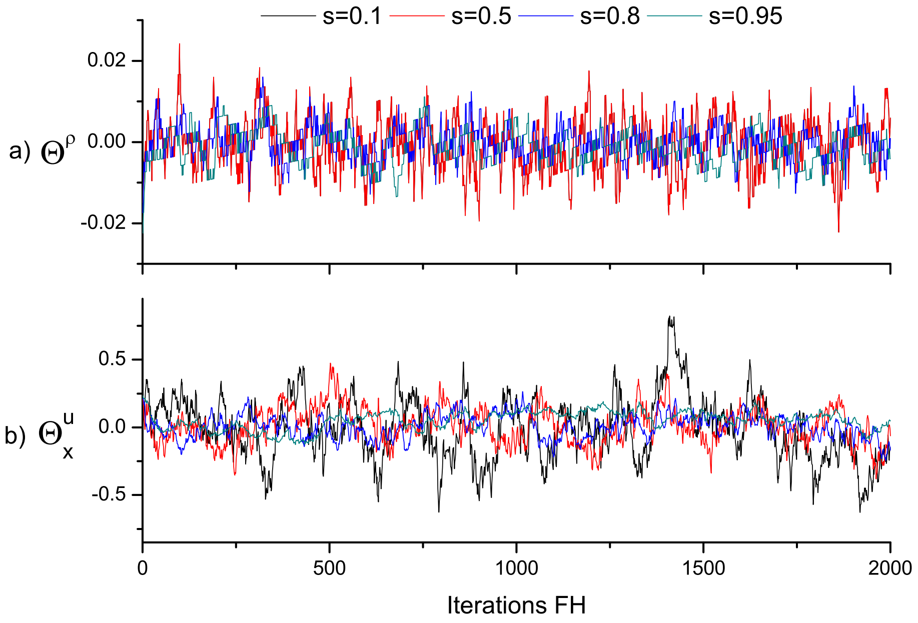

Figure 2.25: The relative difference between the FH and MD phase a) densities and b) velocities; total energy rescaling is used, $\alpha^*, \beta^* = 20000$

In the LL-FH simulation instant values of the total energy are fluctuating, in a way that the averaged over a certain period of time energy is conserved. Hence the total energy of the FH phase must be considered only in terms of averaged in time. Although, for the purpose of this section it is not necessary.

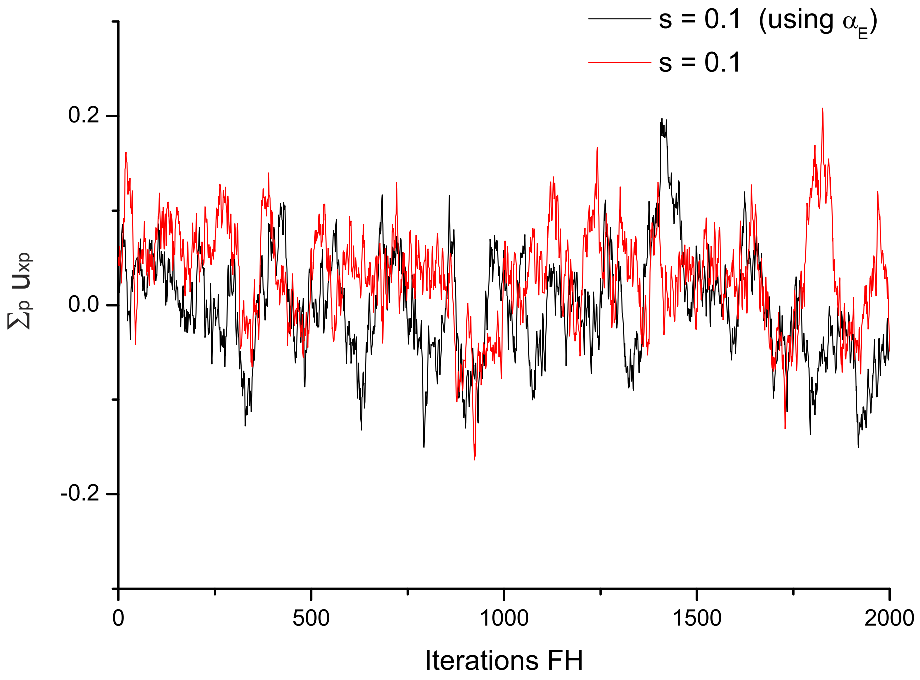

Figure 2.26: MD phase velocities of a random cell for $\alpha^*, \beta^* = 20000$ and $s = 0.1$, with (using α_E, black line) and without energy rescaling

Fig. 2.26 and Fig. 2.28 show that the total energy rescaling do not impose substantial constraints that could disrupt the coupling effect.

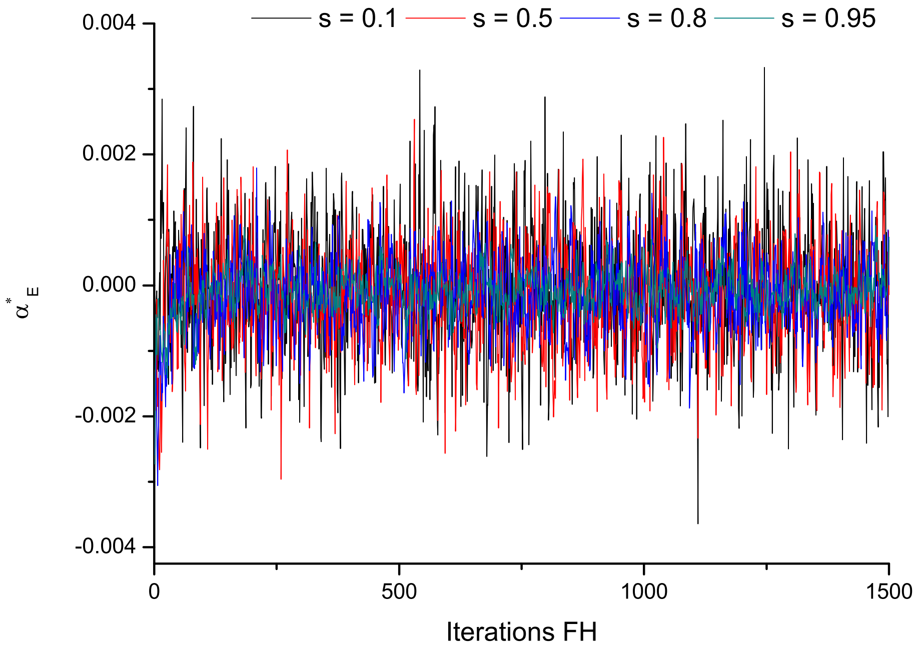

Figure 2.27: α^*_E plots for different s values, $\alpha^*, \beta^* = 20000$, where velocity is rescaled from the total energy scaling concept

Fig. 2.25 demonstrates that the reassessment of α^* and β^* is not required, when total energy rescaling is used.

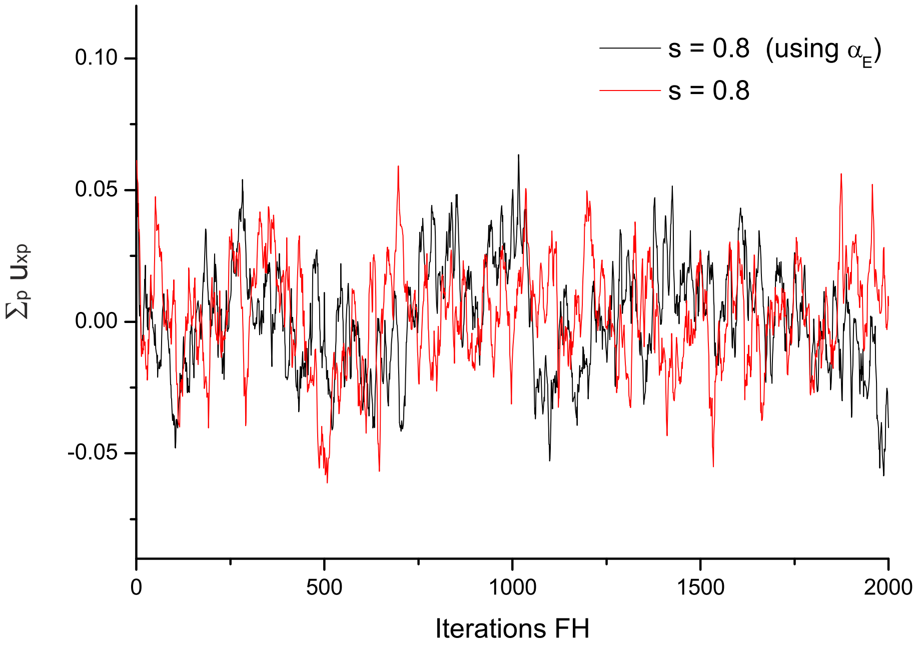

Figure 2.28: MD phase velocities of a random cell for $\alpha^*, \beta^* = 20000$ and $s = 0.8$, with (using α_E, black line) and without energy rescaling

2.6 Conclusions

Summarizing, we have successfully tested the framework of the coupling method between the MD and FH phases. These tests consisted of two parts. The 'one way' coupling and the 'two way' coupling. The first was incomplete in the context of the communications between the phases, while the former showed substantial changes in both phase fluctuations, when the communication is fully implemented. We also estimated and made recommendations for the parameters used in the coupling methods. Especially regarding the lower limit of the parameters, when Lennard-Jones type potential is used. We investigated structural and dynamical properties, resulting in a conclusion that for the larger values of the coupling parameter s the MD particles motion is affected by the external field due to the coupling. The same stretch of the autocorrelation functions along time axis was obtained regardless the timestep of the LL-FH simulation dt_{FH}.

However, in all coupling cases a fundamental limitation was considered, that is a constant value of the coupling parameter s in the whole simulation domain. The variable coupling parameter s profile was implemented for 3D liquid argon, although the results are not presented here, since the simulations produced the same trends, more details regarding the variable coupling parameter s profile can be found in Section 3.3.

Different types of the operator L^u was tested, (2.70) in both 'one' and 'two' way coupling

(here presented operator type is for the 'one way' case)

$$L^u \cdot \left(\tilde{u_j}\tilde{\rho} - \sum_p \rho_p u_{jp} \right) = s(1-s)\beta \left(\tilde{u_j}\tilde{\rho} - \sum_p \rho_p u_{jp} \right), \tag{2.70}$$

resulting in the same trends as with the type defined in (2.41), however the α^* and β^* parameters had much smaller values.

Liquid argon, described with the Lennard-Jones potential is not of a great interest. The study of more complex fluids, like water is an advantageous task. Apart from the abnormal properties, water is also a main solvent used in many experiments.

Before the coupling method is applied to real water it is tested on the 2D 'Mercedes Benz' or BN2D water model, which, like the real water, demonstrates abnormal properties, although it is a much simpler model. The next chapter is devoted to the water models in the context of the coupling framework.

3

Water models

CONTENTS

3.1 Two-dimensional ‘Mercedes Benz’ or BN2D water model 80
3.1.1 Molecular model and details of computation 81
3.1.2 Equations of motion 82
3.1.3 Thermodynamics 84
3.1.4 Structural and dynamic properties 87
3.1.5 Simulation 87
3.1.6 Analysis 89
3.1.7 Summary 99
3.2 ‘Two way’ coupling using BN2D water model 101
3.2.1 Simulation 101
3.2.2 Analysis 103
3.2.3 Conclusions 107
3.3 SPC/E water model implementation of the hybrid framework 109
3.3.1 Model and details of computation 109
3.3.2 Cubic spline interpolation 111
3.3.3 Finite size of the water molecules 112
3.3.4 Pure water 115
3.3.5 Variable coupling parameter *s* 119
3.3.6 Peptide in water 121

3.1 Two-dimensional 'Mercedes Benz' or BN2D water model

In Chapter 2 we successfully established communication between the large and small scales. This was demonstrated for 2D liquid argon. In this chapter a step towards realistic water models is undertaken.

The accuracy and efficiency of the simulation of water is defined by the water model. Three dimensional water models (SPC/E, TIP4P, etc. [57]) are in qualitative and often quantitative agreement with the experiment [3] .

Clearly, a large number of molecules is needed to faithfully reproduce physical chemistry of the system. Even though it is usually enough to simulate a few thousands molecules. Computational considerations have become critical recently, when the focus has shifted to large molecular systems, such as biological macromolecules or hydrodynamics at meso- and macro- scales. Robust reproduction of water in this situations require very large number of molecules in the system. The three dimensional (XYZ) models are still too expensive for statistically sound results. In application to large systems, the N^2 scaling makes critical difference compared to N^3. Thus, two dimensional water models attract interest [5, 67, 68, 69, 70, 71, 72]. They require less computational effort but, at the same time, they are proved to be in qualitative agreement with the experiment [3].

In fact there is available a two-dimensional water model, which gives atomic structural details and three-dimensionality. This model uses only few parameters and is computationally simple enough, and eventually mimics anomalous water properties. This model was developed by Ben -Naim and is called 'Mercedes Benz' (MB) or BN2D water model [50].

The BN2D water is described by a fewer parameters, than other sophisticated models, in which case the dominant interaction can be established easier. This allows to trace the connection between the assumptions of driving forces to the observed properties.

Anomalous water properties appears as hydrophobic effect and unusual thermodynamic properties, such as temperature of maximum density over a wide range of pressures, minimum in the isothermal compressibility depending on temperature and large heat capacity. These properties are assumed to emerge from the ability of water molecules to form the tetrahedrally coordinated hydrogen bonds (that are indirectly presented in the BN2D water model, where three 'arms' are introduced, although water molecule is chemically bonded only with two hydrogens) [50]. The related microscopic processes and structure can be elucidated using simplified computer models based on interatomic interaction potentials which are usually phenomenological.

Other benefit of the BN2D water model is that it treats hydrogen bonding geometrically. This geometrical representation can be described as the third degree (an angle) of freedom in the 2D system. Techniques such as Monte Carlo (MC) or Molecular Dynamics (MD) are among the most popular for calculating both microscopic and macroscopic properties of liquid water and its solutions. While the MC produces static structural properties, the MD can probe both static and dynamic properties, also the coupling method can be applied only using MD technique.

The BN2D water model apart from the straightforward benefits of 2*D* also does not include computationally expensive long range Coulomb interactions that have to be calculated using methods such as Ewald summation [25, 56], requiring a large number of operations and sometimes leading to artefacts.

Despite a very detailed study of the model by Ben-Naim and other authors [5, 73, 74, 75, 76, 77], the dynamical properties of this model have not been thoroughly investigated because it has mostly been studied using MC. An investigation of a 3D 'Mercedes Benz' water model by MD has been reported [58]. However, the authors did not provide detailed results on the physical chemistry of the model. Instead, they concentrated on the numerical performance of the model. The implementation of BN2D model using MD was successfully carried out by [71, 72], but the focus of the investigation was on the properties of the protein, only a limited number of the water model properties has been studied. Here, the focus is on the detailed MD implementation of the BN2D water model in the NVE and NPT ensembles, with the emphasis on the physical chemical characteristics of the model.

3.1.1 Molecular model and details of computation

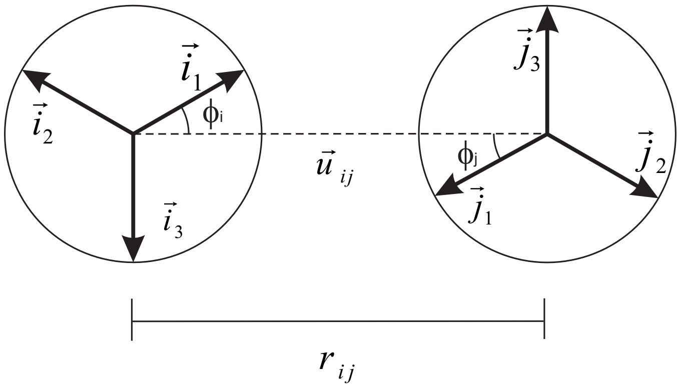

Figure 3.1: Two-dimension 'Mercedes Benz' (MB or BN2D) water model

The 'Mercedes Benz' water model or BN2D [50] water is a simple two-dimensional computational model with three orientation dependent hydrogen bonding arms arranged similar to the Mercedes-Benz logo, Fig. 3.1. Molecules interact pairwise through the Lennard-Jones term and an explicit hydrogen bounding term (which depends on the respective orientation of the arms). The total potential is given as

$$\Phi = \Phi_{LJ} + \Phi_{HB}, \tag{3.1}$$

where the Lennard-Jonnes potential Φ_{LJ} is defined in the usual fashion and the summation is taken over all pairs of interacting particles

$$\Phi_{LJ} = \sum_{ij}^{N} 4\, \varepsilon_{LJ} \left(\left(\frac{\sigma_{LJ}}{r_{ij}} \right)^{12} - \left(\frac{\sigma_{LJ}}{r_{ij}} \right)^{6} \right), \tag{3.2}$$

and Φ_{HB} is the explicit hydrogen bonding term defined as

$$\Phi_{HB} = \sum_{ij}^{N} \varepsilon_{HB} \cdot G[(r_{ij} - r_{HB}), \sigma_r] \times \sum_{k,l=1}^{3} G\left[(\vec{i}_k \cdot \vec{u}_{ij} - 1), \sigma_\phi\right] G\left[(\vec{j}_l \cdot \vec{u}_{ij} + 1), \sigma_\phi\right], \tag{3.3}$$

where G is the Gaussian function

$$G[x, \sigma] = e^{\frac{-x^2}{2\sigma^2}}, \tag{3.4}$$

$\vec{u}_{ij}$ is a unit vector that connects the particle centres, $\vec{i}_k$ and $\vec{j}_l$ are the unit vectors of the orientation of the arms, r_{ij} is the distance between the particles, the angle between a molecule's arms is 120°; $\varepsilon_{LJ}, \varepsilon_{HB}$ and $\sigma_{LJ}, \sigma_{HB} = (\sigma_r, \sigma_\phi)$ are Lennard-Jones and BN2D model well depth and contact parameters respectively Fig. 3.1. Where σ_r is used for the radial part and σ_ϕ for the angular part of the MB potential.

3.1.2 Equations of motion

As was already mentioned in Chapter 2, for conservative potential fields the force acting on the molecule is calculated as the negative gradient of the potential field

$$\vec{f} = -\nabla \Phi. \tag{3.5}$$

For the BN2D model in addition to the translational force a derivative with respect to the angle ϕ describing the molecule's orientation, Fig. 3.1, produces the torque τ:

$$\tau = -\frac{\partial \Phi}{\partial \phi}. \tag{3.6}$$

The additional degree of freedom ϕ gives rise to the angular velocity ω. A corresponding moment of inertia I of the molecule should be introduced in order to characterize the rotation of water molecules (I is an equivalent of mass for rotation).

NVE ensemble

In the case of NVE ensemble, where volume V and energy E are constant, the equation of motion is the Newton's second law, which for the translation is expressed as

$$\ddot{q}_i = \frac{f_i}{m_i}, \tag{3.7}$$

and for the rotation as

$$\ddot{\phi}_i = \frac{\tau_i}{I}, \tag{3.8}$$

where I is the moment of inertia , m_i is the mass, q_i is the spatial coordinate (x or y), ϕ_i is the angle, τ_i is the torque, f_i is the force acting on the i^{th} particle. Afterwords, these equations of motion are implemented numerically using Verlet algorithm, that was described in Chapter 2.

NPT ensemble

In the NVE ensemble the total energy is constant, whereas the kinetic and the potential energies fluctuate. As the kinetic energy is defined by the velocities, the temperature, also defined by the velocities, is not constant. In order to simulate the NPT ensemble, special methods have to be applied to keep the temperature and pressure constant.

The mechanism for feedback regulation of the temperature rests on the idea that the temperature is proportional to the mean-square velocity, which can be varied by adjusting the rate at which time progresses [4]. A new dynamical variable s_t is introduced which rescales the unit of time, and extra terms are added to the equations of motion. There are now two distinct time variables: the real, or physical, time t, and a scaled, or virtual, time t'. The relationship between them is

$$t = \int^{t} \frac{1}{s_t} \cdot dt'. \tag{3.9}$$

While this connection between time and temperature is maintained, pressure can be kept constant by adjusting the container (system) volume. In the MD context this is achieved by a uniform isotropic volume change that eventually rescales particles coordinates:

$$q_i = V^{1/d} q_i', \tag{3.10}$$

where q' is the virtual coordinate changing from 0 to 1, d is the spatial dimensionality and the scaling parameter is V (which corresponds to the volume) [4].

These two transformations result in equations for scaling parameters and modified equations of motion for coordinates.

From the Newton's equations of motions for the i^{th} particle's virtual coordinates q' and virtual time t' the equations of motion for the real coordinates and real time can be obtained:

$$\ddot{q}_i = \frac{f_i}{m_i} - \left[\frac{\dot{s}_t}{s_t}\right]\left[\dot{q}_i - \frac{q_i}{Vd}\dot{V}\right] + \frac{1}{d}\frac{q_i\ddot{V}}{V} + q_i\left(\frac{\dot{V}}{Vd}\right)^2 (1-d), \tag{3.11}$$

$$\ddot{\phi}_i = \frac{\tau_i}{I} - \left[\frac{\dot{s}_t}{s_t}\right] \cdot \dot{\phi}_i, \tag{3.12}$$

$$\ddot{s}_t = \frac{\dot{s}_t{}^2}{s_t} + \frac{s_t}{M_s}\left(\sum_i m_i \left[\dot{q}_i - \frac{q_i}{Vd}\dot{V}\right]^2 + \sum_i I\dot{\phi}_i{}^2 - gkT\right), \tag{3.13}$$

$$\ddot{V} = \frac{\dot{s}_t\dot{V}}{s_t} + \frac{s_t^2}{d\cdot M_V\cdot V}\times\left(\left[\sum_i m_i \left[\dot{q}_i - \frac{q_i}{Vd}\dot{V}\right]^2 + \sum_i F_i\cdot q_i\right] - P_{ex}\cdot d\cdot V\right), \tag{3.14}$$

where P_{ex} is the desired pressure, g is the number of degrees of freedom, M_s and M_V are generalized masses (for derivations see Appendix A.6), k is Boltzmann constant, T is the temperature.

Comparing equations of motion (3.7) and (3.8) for the NVE ensemble with (3.11) - (3.14) for the NPT ensemble, two more equations are available, one for s_t and another for V, as well as modified equations of motion for the coordinates and angles.

3.1.3 Thermodynamics

NVE ensemble

To evaluate the thermodynamic properties from Molecular Dynamics results statistical mechanics should be used. For the NVE ensemble the phase space volume [78, 4] is

$$\Omega(N,V,E) = M\int dp^N \ldots dq^N \delta(E - H(p^N,q^N)) \tag{3.15}$$

and the phase space density is

$$\Sigma(N,V,E) = M\int dp^N \ldots dq^N \Theta(E - H(p^N,q^N)), \tag{3.16}$$

where p and q are the phase space momenta and coordinates, N is the number of particles, V is the volume of the system, E is the total energy, $H(q^N,p^N)$ is the Hamiltonian, M is the normalisation constants, and Θ is the Heaviside step function [79].

The relationship between them is [78]

$$\Omega(N,V,E) = \frac{\partial}{\partial E}\Sigma(N,V,E). \tag{3.17}$$

Assuming the usual separation for the Hamiltonian $H(p^N,q^N) = \Phi(q^N) + K(p^N)$, where $\Phi(q^N)$ is the potential energy and $K(p^N)$ is the kinetic energy, the integrals (3.15) and (3.16) can be partially solved for momenta by applying the Laplace transform, solving for momenta, and calculating the inverse Laplace transform [78] following expressions are obtained

$$\Sigma(N,V,E) = M\int \frac{(E - \Phi(q^N))^{3N/2}}{\Gamma(3N/2+1)} \times \Theta(E - \Phi(q^N))dq^N, \tag{3.18}$$

$$\Omega(N,V,E) = M\int \frac{(E - \Phi(q^N))^{3N/2-1}}{\Gamma(3N/2)} \times \Theta(E - \Phi(q^N))dq^N, \tag{3.19}$$

derivations are available in Appendix A.5.

For a large number of molecules the entropy is [78]

$$S = k_B\ ln\Sigma, \tag{3.20}$$

and the thermodynamic relationships for macroscopic parameters are derived from the entropy definition.

Thus, temperature is given by

$$T = \left(\frac{\partial S}{\partial E}\right)_V^{-1}, \tag{3.21}$$

pressure as

$$P = T\left(\frac{\partial S}{\partial V}\right)_E, \tag{3.22}$$

isochoric heat capacity as

$$C_V = \left[\left(\frac{\partial T}{\partial E}\right)_V\right]^{-1}, \tag{3.23}$$

isothermal compressibility as

$$\frac{1}{\beta_T} = -V\left(\frac{\partial P}{\partial V}\right)_T = -V\left[\left(\frac{\partial P}{\partial V}\right)_S + \frac{T}{C_V}\left(\frac{\partial P}{\partial T}\right)_V^2\right], \tag{3.24}$$

the relationship between the thermal expansion coefficient and the compressibility is

$$\alpha_P = \frac{1}{V}\left(\frac{\partial V}{\partial T}\right)_P = \beta_S\left(\frac{dP}{dT}\right)_V. \tag{3.25}$$

In 2D case the volume $V = dx \cdot dy \cdot dz$ is replaced with the area $A = dx \cdot dy$ (as the third degree of freedom ϕ does not contribute to the 'volume'). The derivatives of the integrals (3.18) and (3.19) with respect to the area (volume) require a substitution $q = A^{\frac{1}{2}}q^*$, since the area (volume) is incorporated into the integration limits [78]. This yields modified equations

$$\Sigma(N,V,E) = M_1 A^N \int \frac{(E - \Phi((A^{\frac{1}{2}}q^*)^N))^{3N/2}}{\Gamma(3N/2+1)} \times \Theta(E - \Phi((A^{\frac{1}{2}}q^*)^N))dq^{*N}, \tag{3.26}$$

$$\Omega(N,V,E) = M_1 A^N \int \frac{(E - \Phi((A^{\frac{1}{2}}q^*)^N))^{3N/2-1}}{\Gamma(3N/2)} \times \Theta(E - \Phi((A^{\frac{1}{2}}q^*)^N))dq^{*N}, \tag{3.27}$$

that can be used for differentiation with respect to the area (volume).

From the definition of the entropy (3.20) and integrals (3.26) and (3.27) the thermodynamic relationships (3.21) - (3.24) are expressed through K, $\frac{\partial\Phi}{\partial A}$, and $\frac{\partial^2\Phi}{\partial A^2}$ only.

Temperature

$$T = \frac{2}{3N}\langle K\rangle, \tag{3.28}$$

pressure

$$P = \rho\, k_B T - \left\langle \frac{\partial\Phi}{\partial A} \right\rangle, \tag{3.29}$$

isochoric heat capacity

$$\frac{C_V}{Nk_B} = \left(\frac{2}{3} \langle K \rangle \left\langle K^{-1} \right\rangle + N(1 - \langle K \rangle \left\langle K^{-1} \right\rangle) \right)^{-1}. \tag{3.30}$$

Following the same approach the first term in (3.24) is obtained as

$$\begin{aligned} -A\left(\frac{\partial P}{\partial A}\right)_S = \frac{2\langle K\rangle}{3A} + \rho A \left\langle \frac{d\Phi}{dA} \right\rangle + A \left\langle \frac{d^2\Phi}{dA^2} \right\rangle + A\left(\frac{3N}{2} - 1\right) \times \\ \times [\left\langle \frac{d\Phi}{dA} \right\rangle \left\langle K^{-1} \frac{d\Phi}{dA} \right\rangle - \rho T \left\langle K^{-1} \frac{d\Phi}{dA} \right\rangle - \left\langle K^{-1} \left(\frac{d\Phi}{dA}\right)^2 \right\rangle], \end{aligned} \tag{3.31}$$

the second term in (3.24), the derivative of the pressure with respect to the temperature, is calculated from the data obtained ($P(T)$). Angular brackets $\langle\ \rangle$ denote ensemble average or, according to the ergodicity hypothesis (see Appendix A.4), time average, $\rho = N/A$ is the number density, k_B is Boltzmann constant, K^{-1} is the reciprocal kinetic energy.

The derivatives of the potential energy with respect to the area are

$$\frac{d\Phi}{dA} = \frac{1}{2A} \sum_{i=1}^{N-1} \sum_{j=i+1}^{N} dx \frac{d\Phi_{ij}}{dx} + dy \frac{d\Phi_{ij}}{dy} \tag{3.32}$$

and

$$\frac{d^2\Phi}{dA^2} = \frac{1}{4A^2} \sum_{i=1}^{N-1} \sum_{j=i+1}^{N} dx^2 \frac{\partial^2\Phi_{ij}}{\partial x^2} + 2 \cdot dxdy \frac{\partial^2\Phi_{ij}}{\partial x \partial y} + dy^2 \frac{\partial^2\Phi_{ij}}{\partial y^2}, \tag{3.33}$$

where Φ_{ij} is the potential between the i^{th} and j^{th} particles, dx and dy are the distances between the particles along x and y respectively.

The technique from [78] was originally used for systems with translational degrees of the freedom only. Our application to the BN2D water model shows that the angular degree of freedom must be treated in the same manner as the translational degrees of freedom when kinetic energy is considered and dismissed when the spatial derivatives are evaluated.

NPT ensemble

Thermodynamic properties in the NPT ensemble were evaluated using the following relationships:

$$C_p = \frac{1}{N} \left(\frac{\partial \langle H \rangle}{\partial T} \right)_p, \tag{3.34}$$

$$\beta_T = \frac{\langle V^2 \rangle - \langle V \rangle^2}{\langle V \rangle T}, \tag{3.35}$$

$$\alpha = \frac{1}{\langle V \rangle} \left(\frac{\partial \langle V \rangle}{\partial T} \right)_p , \tag{3.36}$$

where $\langle H \rangle = \langle K \rangle + \langle \Phi \rangle + P \cdot \langle V \rangle$ is the enthalpy, C_p is the heat capacity, α is the thermal expansion coefficient, β is the isothermal compressibility computed from the fluctuations [4, 59].

3.1.4 Structural and dynamic properties

The structure of the MB water is characterised by the radial distribution function (RDF) and a function quantifying the angular alignment

$$g_r^{(2)}(r) = \frac{2V}{N^2} \left\langle \sum_{i<j} \delta(r - |\vec{r}_{ij}|) \right\rangle , \tag{3.37}$$

and

$$g_\phi^{(2)}(r) = \frac{2V}{N^2 Z_{ij}} \left\langle \sum_{i<j} z_{ij} \delta(r - |\vec{r}_{ij}|) \right\rangle , \tag{3.38}$$

$$z_{ij} = \sum_{k=1}^{3} \sum_{l=1}^{3} G(\vec{i}_k \cdot \vec{u}_{ij} - 1) G(\vec{j}_l \cdot \vec{u}_{ij} + 1), \tag{3.39}$$

$$Z_{ij} = \int_0^\infty \left\langle \sum_{i<j} z_{ij} \delta(r - |\vec{u}_{ij}|) \right\rangle dr, \tag{3.40}$$

where N is the number of molecules in the corresponding solvation shell, Z_{ij} is the normalization factor.

The dynamic characteristics are described by the velocity correlation functions that cannot be obtained using Monte Carlo method.

The velocity autocorrelation function is

$$f_v(\tau) = \langle \vec{v}(t) \cdot \vec{v}(t+\tau) \rangle , \tag{3.41}$$

where $\vec{v}(t)$ and $\vec{v}(t+\tau)$ are the translational velocities at time moments t and $t+\tau$. If processes are stationary f_v is independent of t. The rotation velocity autocorrelation function is defined by the rotational velocity $\omega(t) = \frac{\partial \phi}{\partial t}$:

$$f_\omega(\tau) = \langle \omega(t) \cdot \omega(t+\tau) \rangle . \tag{3.42}$$

3.1.5 Simulation

The system of 2500 particles was simulated in the NVE ensemble using Verlet method with the velocity rescaling algorithm for thermostating [25]. Since the velocity rescaling was applied very infrequently and only to correct the numerical errors, the data calculated between rescaling moments was used for thermodynamic properties evaluation. The simulation domain was chosen as a square box, since structural restrictions were not assumed. The timestep $dt^* = 0.001$ was small enough to account for the rotation of the molecules which was significantly faster than the translation. The timestep can be increased up to $dt^* = 0.01$, which is the largest timestep that maintains stable simulation for the current conditions.

Following the same approach of dimensionless units, in the case of MB water they are given by

$$T = \frac{\varepsilon_{HB}}{k_B} T^*, \tag{3.43}$$

$$r = r_{HB} \cdot r^*, \tag{3.44}$$

$$m = m_{H_2O} \cdot m^*, \tag{3.45}$$

$$t = \sqrt{m \cdot r_{HB}^2 / \varepsilon_{HB}} \cdot t^*, \tag{3.46}$$

$$P \cdot V = \varepsilon_{HB} \cdot P^* \cdot V^*, \tag{3.47}$$

where * denotes the dimensionless variables. The MB model parameters are listed in Table 3.1. The value of σ_{HB}^* should be small, such that only one hydrogen bond is formed [5].

The density was set to $\rho = 1054 \ \frac{kg}{m^3}$ or $\rho^* = 0.9$. In the case of the NPT ensemble instead of the density, pressure was set to $P = 192 \ MPa$ or $P^* = 0.195$.

The NPT ensemble requires to set parameters M_s and M_V, that contribute to the constant temperature and volume. These quantities must be determined empirically and do not affect results when system reaches equilibrium. For this particular case $M_s = 1$ and $M_V = 0.1$.

In the NPT simulation the Verlet integrator is replaced with the Predictor-Corrector as well as different set of equations of motion are used. For more details regarding Predictor-Corrector method see Appendix A.9. The code description can be found in Appendix A.7.

The kinetic energy in MB model is calculated as

$$K = \sum_{i=1}^{N} \frac{m\vec{v}_i^2}{2} + \frac{I\omega_i^2}{2}, \tag{3.48}$$

where I is the moment of inertia, $\vec{v}_i$ and ω_i are the translational and angular velocities.

Variable	Real values	Units	Dimensionless
m_{H_2O}	$18 \cdot 10^{-3}$	$\frac{kg}{mol}$	1
r_{HB}	2.78	Å	1
ε_{HB}	12.742	$\frac{kJ}{mol}$	-1
ε_{LJ}	1.274	$\frac{kJ}{mol}$	0.1
σ_r	0.25	Å	0.085
σ_ϕ	-	-	0.085
σ_{LJ}	2.065	Å	0.7
I	$2.938 \cdot 10^{-47}$	$kg \cdot m^2$	0.0127
k_B	$1.38 \cdot 10^{-23}$	$\frac{J}{K}$	1

Table 3.1: The variables used in MD simulations. r_{HB} is hydrogen bond length, m_{H_2O} is the water molecule mass, I is the moment of inertia [5], ε_{HB} is the hydrogen bond energy, ε_{LJ} is the Lennard-Jones energy, σ^*_{LJ} is 0.7 of the r^*_{HB}

3.1.6 Analysis

Thermodynamics (NVE ensemble)

The macroscopic parameters of water can be obtained from the equation of state that requires pressure, volume, and temperature relationships or using equations (3.21) - (3.24) in the case of NVE ensemble.

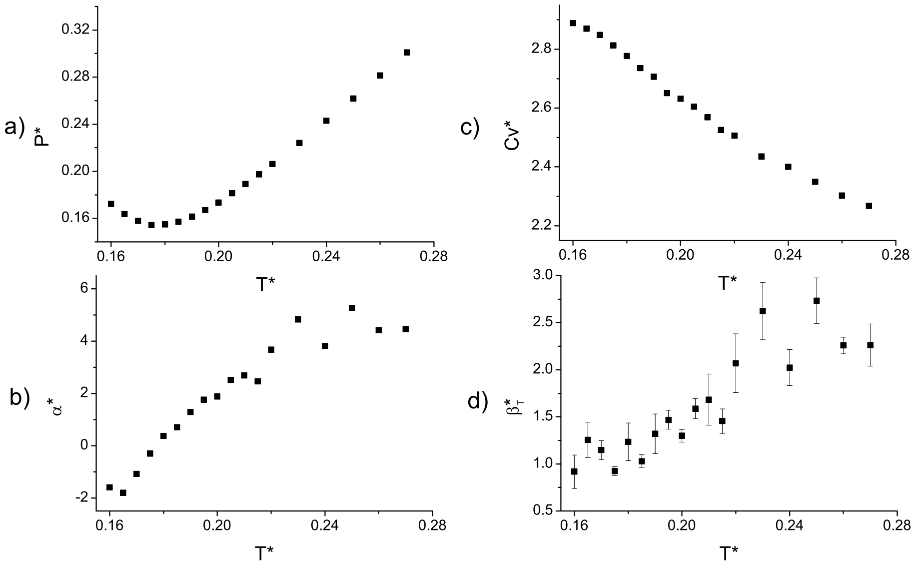

Figure 3.2: Simulated isothermal compressibility β^*_T, pressure P^*, isochoric heat capacity C^*_V, isothermal expansion coefficient α^* in the NVE ensemble, $\rho^* = 0.9$. The error bars for β^*_T are shown to illustrate slow convergence for this parameter

The obtained pressure as a function of temperature, Fig. 3.2a, is qualitatively the same as the experimental values, Fig. 3.3a. It almost linearly increases starting from $T^* \approx 0.18$.

The heat capacity of real water decreases with the temperature, Fig. 3.3c. The BN2D water model mimics the same trend, Fig. 3.2c. This trend is the result of the hydrogen bond rearrangement.

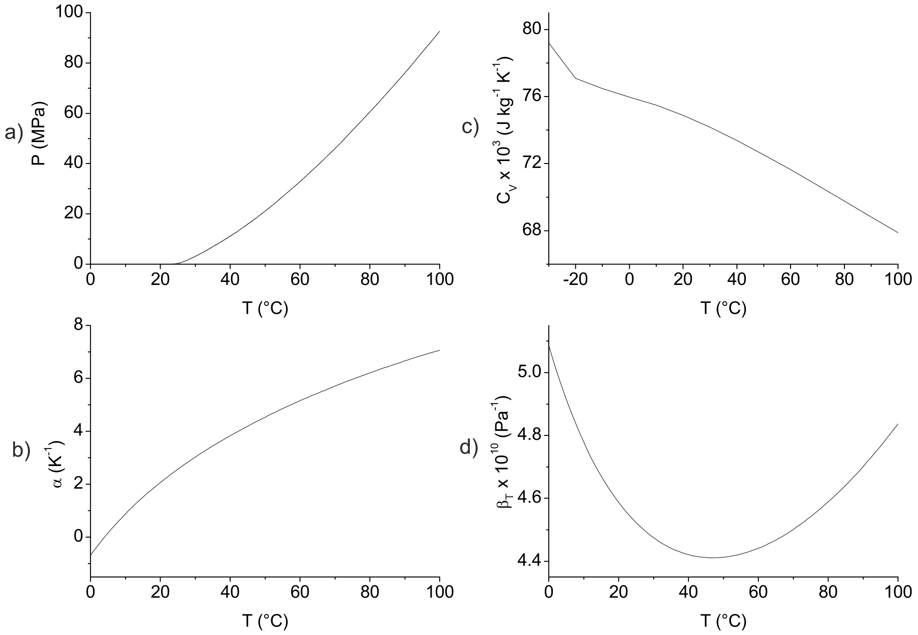

Figure 3.3: Experimental water isothermal compressibility β_T, pressure P, isochoric heat capacity C_V, isothermal expansion coefficient α (taken from [3])

The temperature expansion coefficient, Fig. 3.2b, 3.3b, of water changes sign at $T^* = 0.18$.

If MB water molecule is fully hydrogen-bonded it forms hexagonal ice. If water is in a liquid state, when hydrogen bonds collapse, molecules can approach each other closer. As the temperature of liquid water increases, the hydrogen bonds continue to collapse and allow the non-bonded molecules to approach closer, thus, the number of neighbours increases. This is in contrast with other liquids, when due to the increase of temperature the distance between the molecules increases accounting for the expansion of available space and the increase of kinetic energy.

The compressibility decreases with temperature, Fig. 3.2d, 3.3d, 3.6d. The temperature dependence of β_T^* is similar to the experiment Fig. 3.3d within the large error bars caused by slow convergence of the first term in the equation (3.24). This leads to the slow convergence of the compressibility.

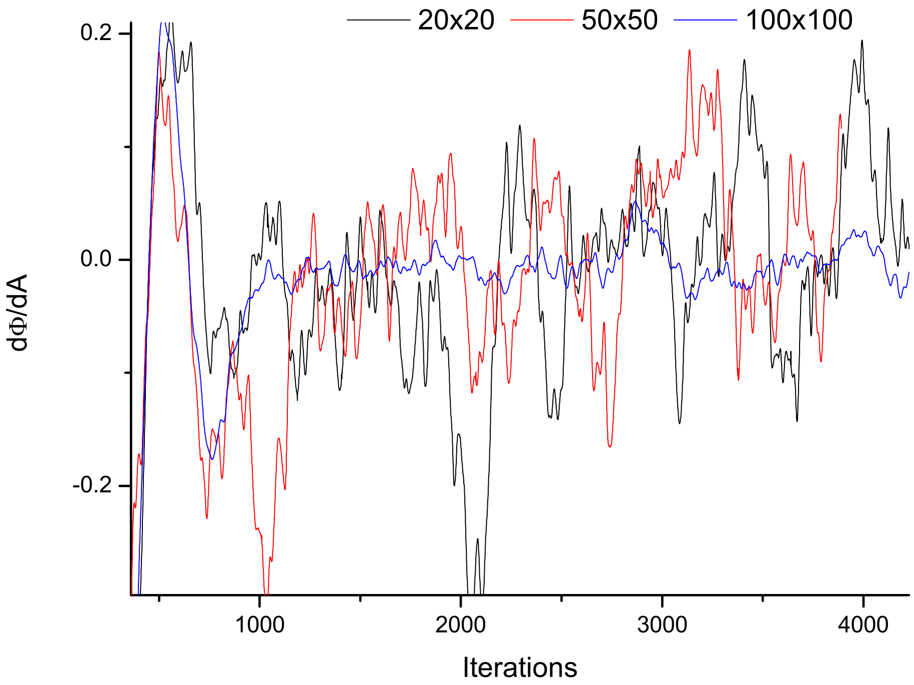

Figure 3.4: The fluctuations of the 1^{st} order derivative with respect to the area for different system sizes (the number of molecules is indicated), $T^* = 0.21$.

Fluctuations of the first order derivative of the potential with respect to the area for different system sizes are demonstrated in Fig. 3.4. It shows that averaging time must be considered long enough to ensure the convergence to the mean value of these fluctuations.

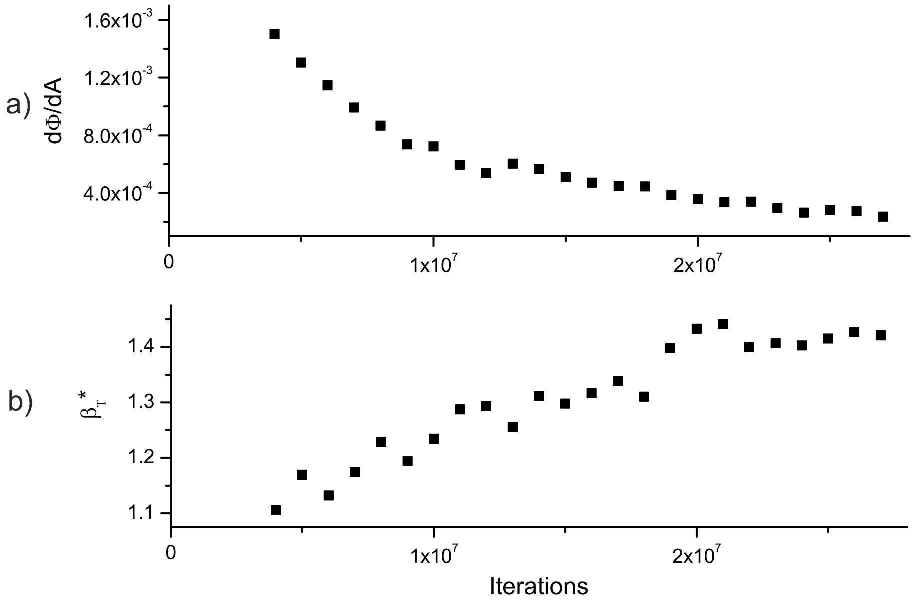

Figure 3.5: a) convergence of the 1^{st} order derivative of the MB potential with respect to area b) isothermal compressibility , $T^* = 0.21$, $N = 2500$

For instance, system of 2500 MB particles shows slow convergence of $\frac{d\Phi}{dA}$ Fig. 3.5.a, which consequently yields slow convergence of the isothermal compressibility Fig. 3.5.b.

In our simulations $11 \cdot 10^6$ iterations were needed to obtain Fig. 3.2d.

Thermodynamics (NPT ensemble)

In the NPT ensemble the macroscopic parameters can be evaluated using equations (3.34) - (3.36).

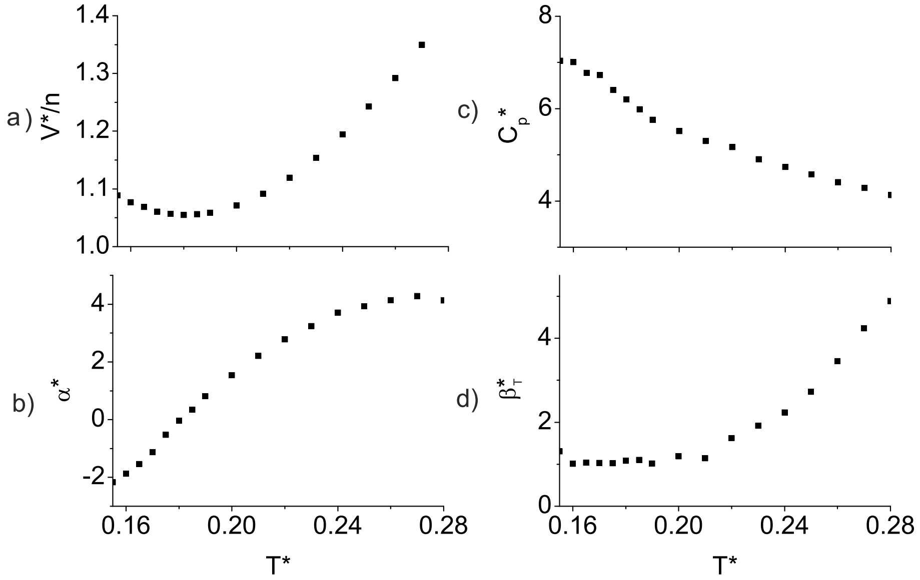

Figure 3.6: Simulated isothermal compressibility β^*_T, volume V^*, isobaric heat capacity C^*_p, isothermal expansion coefficient α^* in the NPT ensemble, $P^* = 0.195$.

The temperature of minimum volume/maximum density Fig. 3.6a, the negative expansion coefficient Fig. 3.6b, the large heat capacity Fig. 3.6c, and the minimum in the isothermal compressibility Fig. 3.6d are consistent with the thermodynamic parameters as in the NVE ensemble, experimental data and other authors who implemented BN2D model using Monte Carlo method, that can be found in [5].

It is important to demonstrate that, despite the different approaches of evaluating the thermodynamic parameters such as pressure in the NVE and NPT ensembles, a consistent state of the system is obtained.

Fig. 3.7 is a combination of two plots, one is the pressure vs temperature at $\rho^* = 0.9$, and the other is the density vs temperature at $P^* = 0.195$. From the pressure curve the value of $P^* = 0.195$ is realised at $T^* = 0.215$. This corresponds to $\rho^* = 0.9$ on the density curve, which is equal to the set density of the pressure curve. The reverse is also true: the $\rho^* = 0.9$ value on the density curve produces $P^* = 0.195$, the correct value for the pressure curve at this temperature.

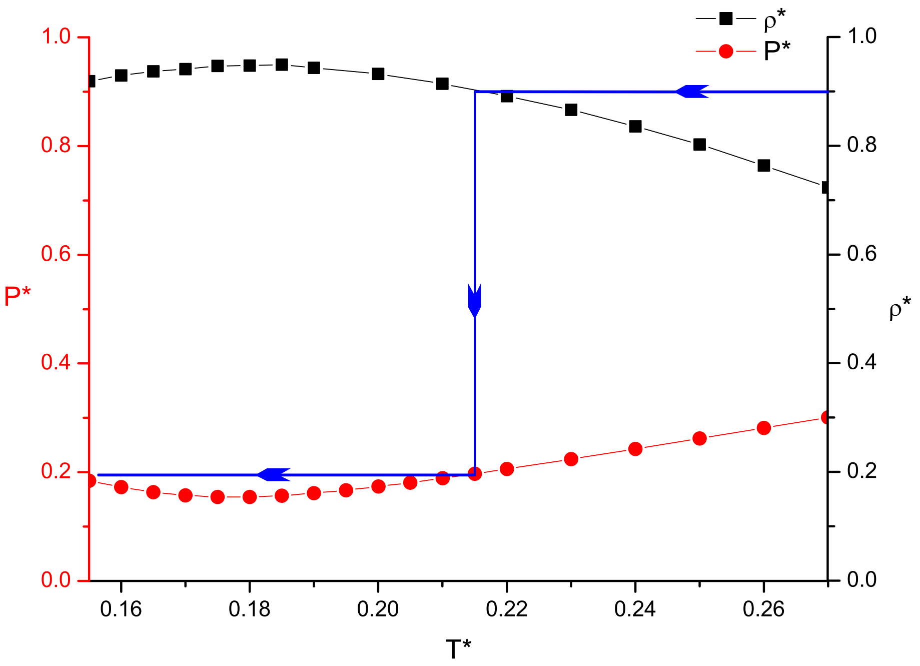

Figure 3.7: The dependence of the pressure for the NVE ensemble and density for the NPT ensemble on temperature. Two different simulations are depicted here, black squares are the density vs temperature in the NPT ensemble and red circles are the pressure vs temperature in the NVE ensemble. The blue arrowed line shows that for the temperature $T^* = 0.215$ and pressure $P^* = 0.195$ in the NPT ensemble density becomes $\rho^* = 0.9$, while in the case of the NVE ensemble with density $\rho^* = 0.9$ and temperature $T^* = 0.215$ pressure becomes $P^* = 0.195$, resulting in the same state of the system regardless the approach used

The analysis of the equations of motion in the NPT ensemble and the equation for pressure (3.22) in the NVE ensemble shows that the pressure is obtained differently. In the NVE ensemble full kinetic energy is used, while in the NPT only translational part is included. Nevertheless, the same thermodynamic state of the system is obtained, Fig. 3.7, proving that the pressure evaluation is consistent in both ensembles.

Dynamics

The dynamical properties of water are characterised by the translational (VACF) and rotational (RVACF) autocorrelation functions.

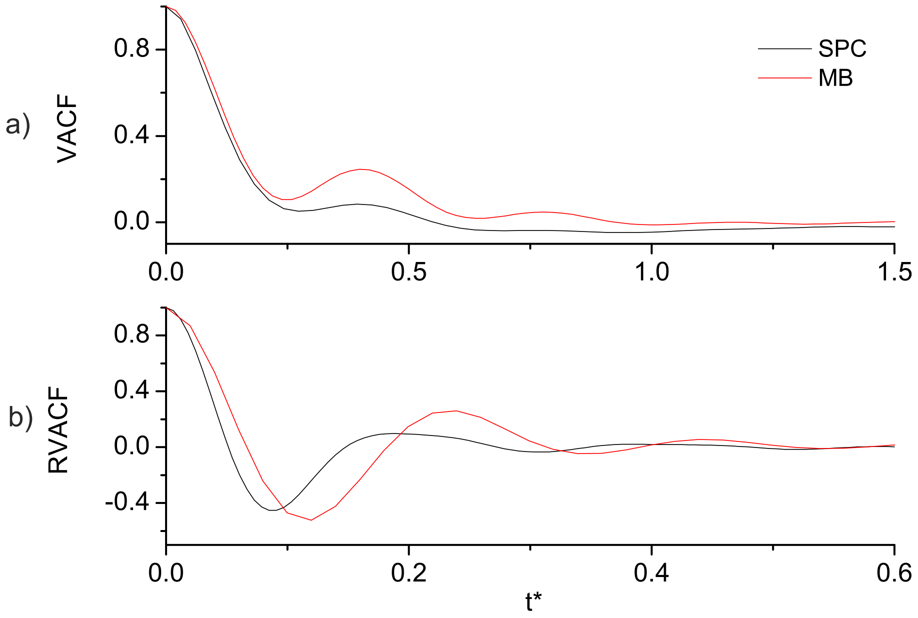

Figure 3.8: Velocity autocorrelation functions at $T^* = 0.195$ for BN2D and SPC water models

The obtained autocorrelation functions, Fig. 3.8, coincide with the ones from 3D realistic models, such as SPC [80]. The minima on VACF and RVACF are located at approximately correct positions, which confirms the correctness of the values of the moment of inertia and mass. The moment of inertia of MB particle can be additionally adjusted such that RVACFs from SPC and MB models coincide even better.

Structure

The structure formed by BN2D water model, Fig. 3.9, is similar to the realistic water model. It also reproduces the results by Ben-Naim [81].

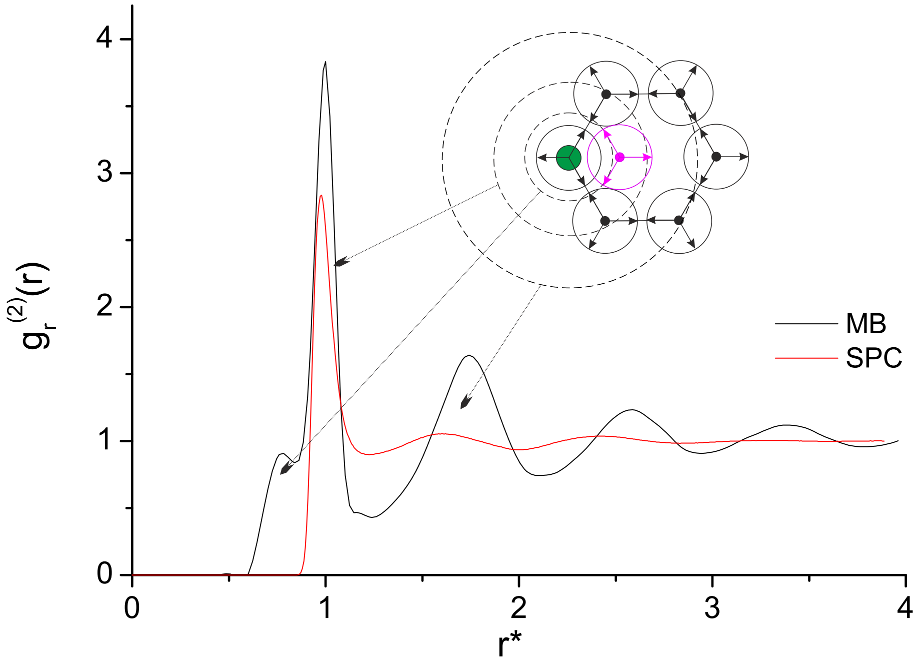

Figure 3.9: Radial distribution function at $T^* = 0.16$. The reference molecule is shown in green. The 'interstitial' water is magenta

The maxima on RDF indicates solvation shells of different order. The maxima roughly corresponds to the hexagonal ice structure of water, while a small maximum at ≈ 0.7 is formed by the 'interstitial' water molecules.

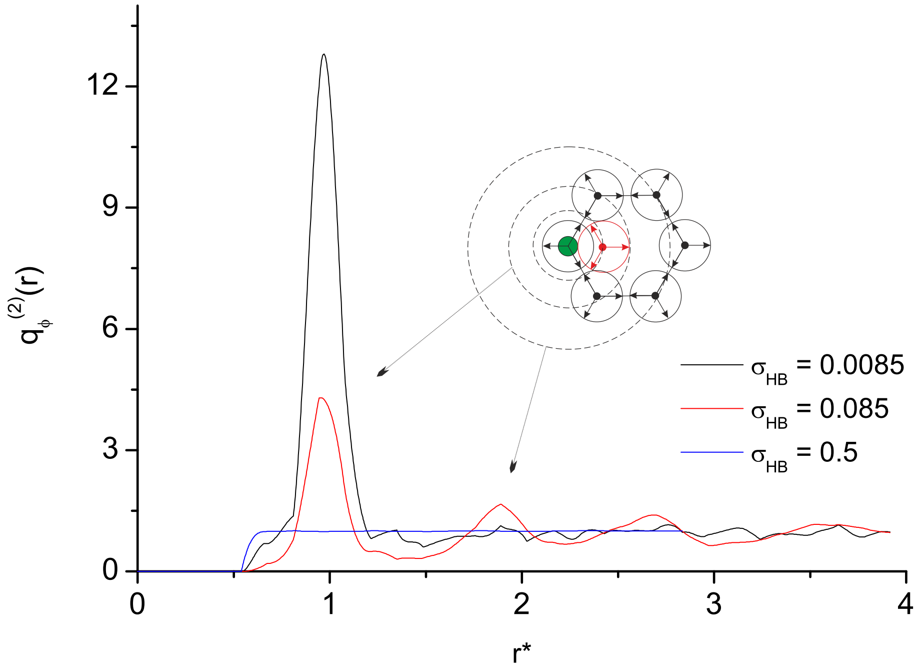

Figure 3.10: Orientational distribution (3.38) of MB water as a function of distance at $T^* = 0.16$

The calculation of the $g_\phi^{(2)}(r)$ from (3.38) allows to evaluate the orientation of the molecules in different solvation shells.

If the orientational part of the potential is switched off the molecules are oriented randomly and z_{ij} is constant starting form the distance corresponding to the very first peak on the RDF, Fig. 3.10.

The peaks of $g_{\phi}^{(2)}(r)$ show that in different solvation shells the molecules are aligned with respect to the central molecule. This alignment roughly corresponds to the hexagonal ice lattice.

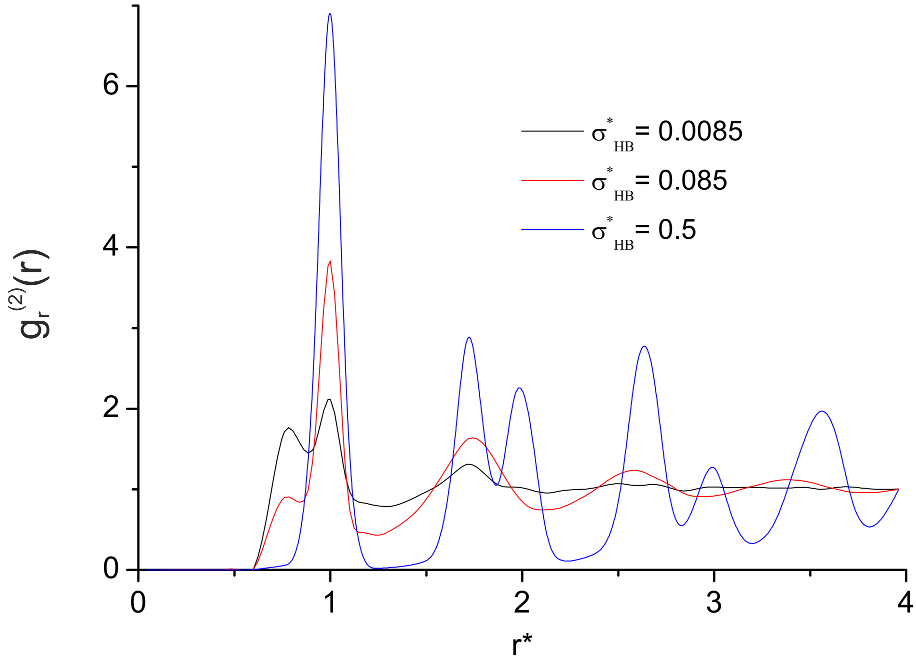

Figure 3.11: Radial distribution function for different σ^*_{HB} in orientational part of MB potential, at temperature 300K

The comparison between RDFs of the SPC and BN2D water models, Fig. 3.9, shows that the BN2D water model has unnatural small maximum at 0.7, that was described by the author of the BN2D water model [81].

The first small peak on RDF at 0.7 corresponds to the interstitial water, Fig. 3.9. These molecules are randomly oriented which is demonstrated by the absence of the peak on the $g_{\phi}^{(2)}(r)$, Fig. 3.10. This is reasonable as these molecules do not form hydrogen bonds with the central molecule. If the σ_{HB} of the orientational part is decreased only the first peak remains on $g_{\phi}^{(2)}(r)$, thus strong HB alignment destroys the orientation structure beyond the first solvation shell.

Directionality of the hydrogen bond

The MB model is very convenient for studying the properties of hydrogen bonding. In fact, it was originally designed for this purpose - to incorporate explicitly hydrogen bonds into a simple molecular model. In particular, the directionality of the hydrogen bond can be studied by varying the parameter σ^*_{HB}. Low values of this parameter model a very directional hydrogen bond when the HB interaction is effective when the ‘arms’ of the molecules are aligned along a straight line. This also implies only one HB for one arm of the molecule. High values of σ^*_{HB} allow HB interactions when the orientation of the molecules is more relaxed, thus leading to bent HBs and branched bonds, when one 'arm' can make two bonds.

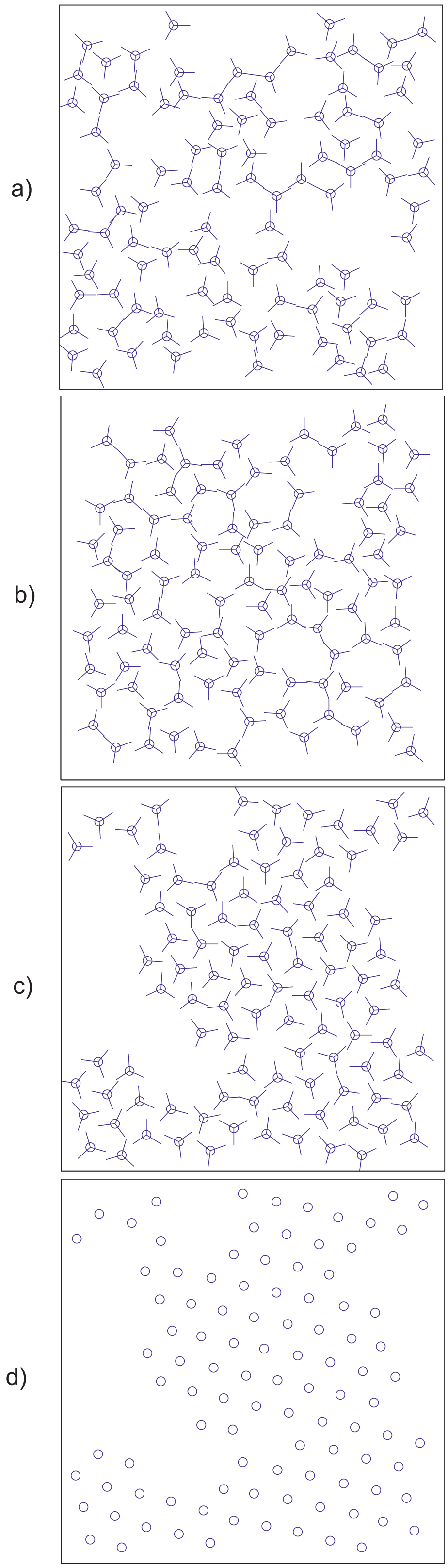

Figure 3.12: Structures formed for different σ^*_{HB} in orientational part of the MB potential, at temperature 300K. Where a) $\sigma^*_{HB} = 0.0085$, b) $\sigma^*_{HB} = 0.085$, c,d) $\sigma^*_{HB} = 0.5$

Our analysis of the implementation of the BN2D water model using structural and dynamical properties was conducted at the temperature of 300 K and the density of 1054 $\frac{kg}{m^3}$. The RDF curves in Fig. 3.11 and Fig. 3.12 show that increasing σ^*_{HB} to 0.5 leads to a crystal like structure. A clear separation of phases is seen in Fig. 3.12. The long range ordering of molecules is apparent when only the locations of the molecules are plotted Fig. 3.12.d. This is also confirmed by the RDF. Similar RDF were obtained for TIP5P ice at 250 K [57]. The dynamics of the molecules is characterised by oscillations around metastable positions, Fig. 3.13, and slow rotation without changing direction for long time Fig. 3.14. This also resembles the crystal phase behaviour.

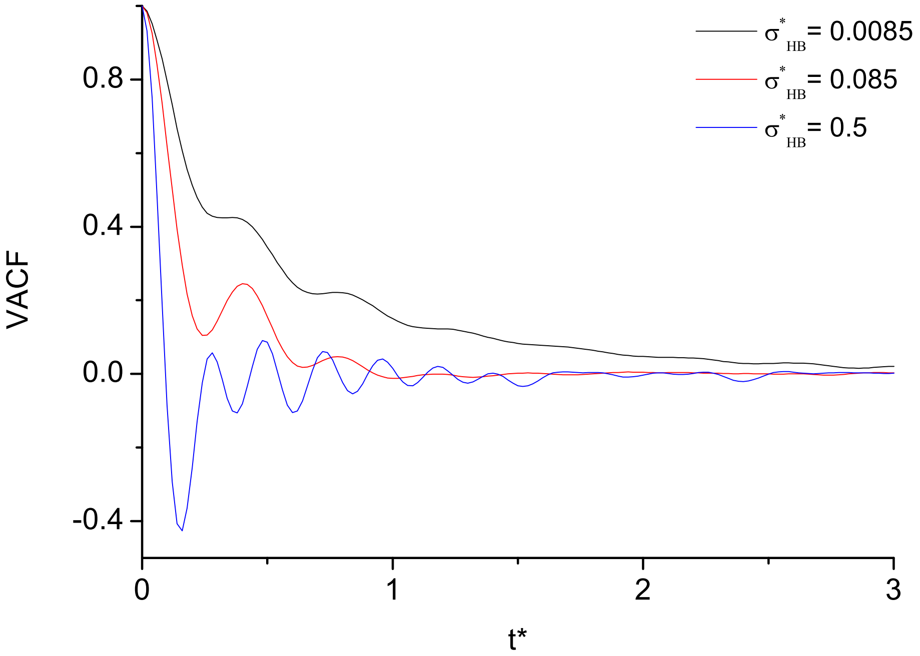

Figure 3.13: Velocity autocorrelation function for different σ^*_{HB} in orientational part of the MB potential, at temperature 300 K

If the value of σ^*_{HB} is decreased to 0.0085 the effect is, in a sense, opposite. The system remains in liquid states, but the order is lost beyond the second solvation shell, Fig. 3.11 and Fig. 3.12. Strong directionality of HB results in the appearance of many non-bonded molecules that rotate almost freely, Fig. 3.14. There are also dimers and trimers, Fig. 3.11 and Fig. 3.12. All molecules tend to keep their translational motion in the same direction for long times, in contrast to real water, which VACF decays much faster.

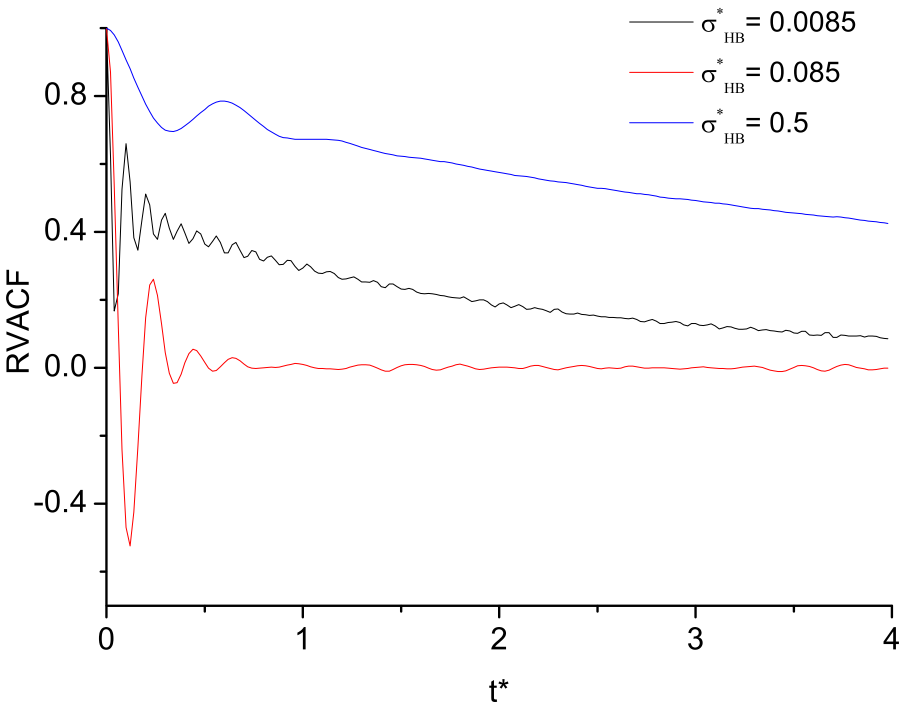

Figure 3.14: Rotation velocity autocorrelation function for different σ^*_{HB} in orientational part of the MB potential, at temperature 300 K

Overall, different values of σ^*_{HB} for the orientational part of the MB potential show that the structural and dynamical properties are changed dramatically. The changes lead to either unnatural solid phases (which should not be formed at this temperature and density) or liquid phases with abnormal structural and dynamical properties that deviate from real water behaviour.

Stability analysis

In general, the BN2D water model simulation is stable if the timestep is less than $dt^* = 0.01$. Fig. 3.15 shows that the standard deviation of the rotational velocity rapidly increases when the timestep exceeds this value. The translational velocities are less affected by the timestep, thus the maximal timestep is restricted by the rotation of the MB molecule.

In the NPT ensemble the stability for the long course of the run is maintained with a set of parameters, such as the number of particles, masses M_s and M_V and the timestep, which yields a slow energy drift if timestep exceeds $dt^* = 0.005$.

3.1.7 Summary

The BN2D water model can be used for simulations using Molecular Dynamics. The results presented here show that BN2D water model mimics real water anomalous properties, dynamics and structure.

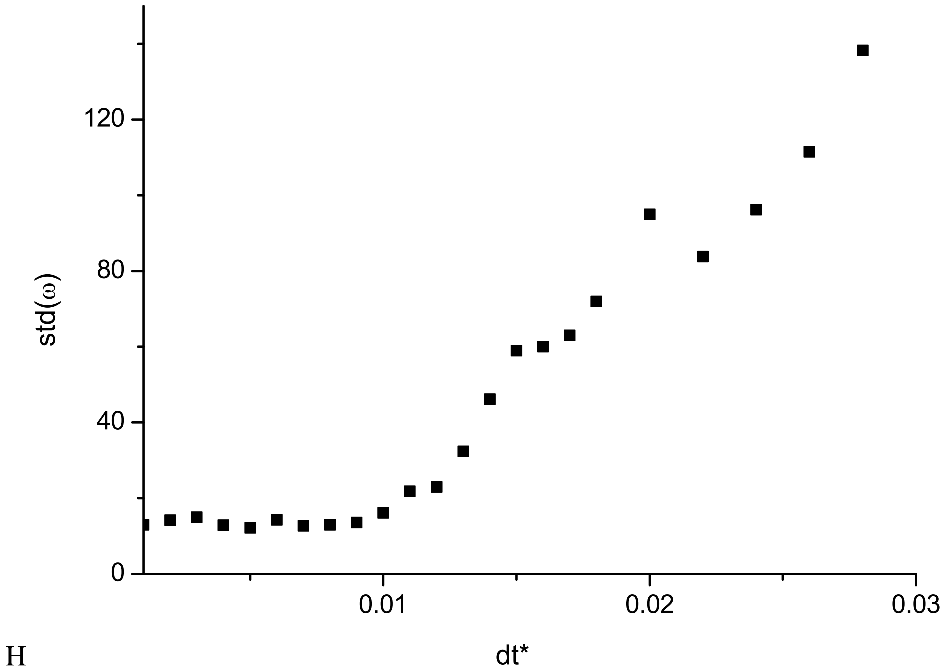

Figure 3.15: The standard deviation of the rotational velocity with the timestep dt^* (NVE ensemble).

We showed that different values of σ^*_{HB} for the orientational part of the MB potential dramatically change the structural and dynamical properties. The changes lead to unnatural solid phases or liquid phases with abnormal structural and dynamical properties that deviate from the real water properties.

For the first time thermodynamic formulas for the BN2D water model were derived when NVE ensemble is used. Also we derived equations of motion for the BN2D water model when NPT ensemble is used.

We also showed, that the calculation of the pressure in the NVE and NPT ensembles is different. In the NVE ensemble full kinetic energy is used, while in the NPT ensemble rotational part is excluded. Our simulation results confirm the correctness of the obtained formulas which produce the same thermodynaic state for the different ensembles.

More details about BN2D water model simulation can be found in Appendix A.7.

The benefits of the investigated model are most obvious for very large systems approaching hydrodynamic scales because the model will allow direct atomistic verification of the hydrodynamic description. Furthermore, using this model, a hybrid approach combining both atomistic MD and hydrodynamic descriptions can be investigated and verified.

The following section is entirely devoted to the BN2D water model in the context of the ‘two way’ coupling described in Chapter 2.

3.2 'Two way' coupling using BN2D water model

In molecular modelling the focus is increasingly shifting towards large molecular systems such as biological macromolecules, the aggregates of molecules (for example various kinds of membranes, including biological), or even entire living cell organelles with all their molecular complexities (the so called 'crowded' biomolecular systems) [82, 83]. Necessarily approximations have to be used to make large scale representation of the system computationally feasible. These include various coarse graining techniques, continuum modelling, combinations of the two, and other approaches.

The key point in using such approximations is their validity. To perform the validation of a system under consideration it has to be computationally tractable at both small and large scales. For example, to check the validity of hydrodynamic description of a system of specific size over specific time, it has first to be modelled at these size and time using atomistic representation. Then the hydrodynamic representation of the system can be modelled and validated against the "ab initio" atomistic results.

Besides the development of approximated descriptions, such systems provide a test bed for hybrid approaches when fundamentally different descriptions are used simultaneously at different locations of the system.

In the hydrodynamic limit the number of particles in atomistic molecular dynamics simulations makes critical difference in terms of computational efforts. Here 2D models can offer a reasonable compromise between the accuracy and the computationally efficiency. For water the BN2D model reproduces many important aspects of experimentally observed behaviour, while it is significantly faster in comparison with high-fidelity 3D water models such as TIP4P .

The BN2D water model is extended to hydrodynamics by using hybrid Molecular Dynamics (MD) / Fluctuating Hydrodynamics (FH) frameworks. The hybrid framework was first developed for the 2D liquid argon in equilibrium [84] and also non-equilibrium conditions [47]. As was explained before the idea of this multiscale approach is to use a physical analogy with two-phase flow modelling to concurrently represent the system using continuum and atomistic phases of the same liquid. The criteria of mixing are the preservation of the appropriate macroscopic conservation laws (such as mass and momentum) and thermal fluctuations as required by the fluctuation-dissipation theorem.

3.2.1 Simulation

The coupling framework described in this work yields new equations of motion, that are integrated instead of the standard MD equations used for the study of BN2D water model. The equations of motion for the MB particles (2.42) and (2.54) were applied, although the angles were advanced using (3.6).

Partially, this is because the LL-FH solution is not available for the rotational degrees of freedom. Although, in order to avoid speculations regarding the consistency of the models used here, following investigation and assumptions were made. Since the distance between the centre and the arms of MB particle is small, it is assumed that the external force field due to the coupling does not change at this distance. Therefore, the coupling technique is applied to the translational velocities of MB particles only.

The FH phase was obtained using conservation (2.4) and (2.15) together with the definitions from the (2.9) and (2.18), where operators L^{ρ} and L^{u} were used the same as in the ‘two way’ 2D liquid argon case, effectively (2.40) and (2.53).

Simulations are conducted on a regular grid in a 2D square box split into 5 by 5 cells with 10000 MB water molecules and 25 nodes of FH values at the temperature of $300[K]$ and the density of $\rho = 1054\left[\frac{kg}{m^3}\right]$.

The simulations are carried out in dimensionless units given as for the BN2D water model in the previous sections.

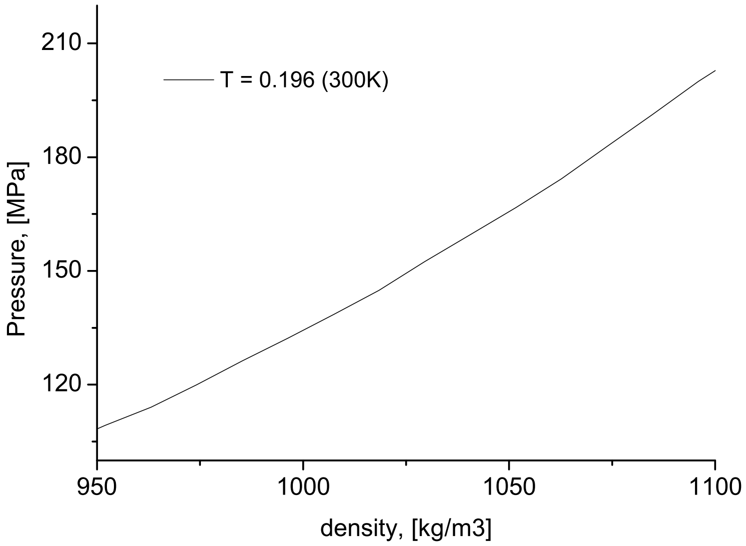

Figure 3.16: Equation of state for MB water model.

As was demonstrated before, for the particular conditions ($T = 300[K]$ and $\rho = 1054\left[\frac{kg}{m^3}\right]$) the MB water model quantitatively represents real water.

The LL-FH simulation requires macroscopic transport parameters of continuum phase, such as bulk and shear viscosities, as well as the equation of state Fig. 3.16 for calculating pressure, which was obtained from the pure MB simulations.

The commonly used method to obtain viscosities is by using the Green-Kubo relationships [4], where the bulk viscosity is calculated as an integral over time

$$\eta = \frac{V_0}{k_B T} \lim_{t \to \infty} \int_0^t B_{ACF}(t')dt', \tag{3.49}$$

where V_0 is the system's volume,

$$B_{ACF}(t') = \langle \delta P(t') \delta P(0) \rangle, \tag{3.50}$$

and $\delta P(t) = P(t) - P_{avg}$ is the pressure fluctuations.

For the shear viscosity the following relationship was used:

$$\xi = \frac{V_0}{k_B T} \int_0^t S_{ACF}(t')dt', \tag{3.51}$$

where

$$S_{ACF}(t') = \langle P_{xy}(t') \cdot P_{xy}(0) \rangle. \tag{3.52}$$

The off-diagonal components of the pressure tensor are calculated using

$$P_{xy} = \frac{1}{V} \sum_{i=1}^{N} \sum_{j=i+1}^{N} \left(m \cdot u_i^x \cdot u_i^y + f_{ij}^x \cdot r_{ij}^y \right), \tag{3.53}$$

where u_i is the particle's translational velocity, f_{ij} is the intermolecular force, r_{ij} is the distance between the molecules and the superscripts denote x and y components.

The MB water model parameters are given in Table. 3.1.

The ratio between the FH and MD simulations timesteps is $dt_{FH}/dt_{MD} = 10$, updating/exchanging the averaged over the cell values at every 10^{th} MD iteration.

The coupling parameters were chosen $\alpha^*, \beta^* = 2$, the values were selected such that the coupling strength is weak to avoid unphysical behaviour and at the same time strong enough to demonstrate the effect of coupling. Values of the coupling parameter s have no particular importance, thus they were set to $0.1/0.5/0.8$ to demonstrate the influence on the FH phase behaviour in the mixture of the FH and MD phases. Here, a constant parameter $s(x)$ profile was used across the system.

3.2.2 Analysis

Standard deviation of fluctuations of the mixture velocity x component $\tilde{u}_x$ for the coupled systems, pure MD phase (MB) and FH phase are shown in the Fig. 3.17. Standard deviations of the density are not present here, since they show the same trend. The effect of pulsations is also believed to be present here as it was in Chapter 2. Overall, the standard deviation values are very close.

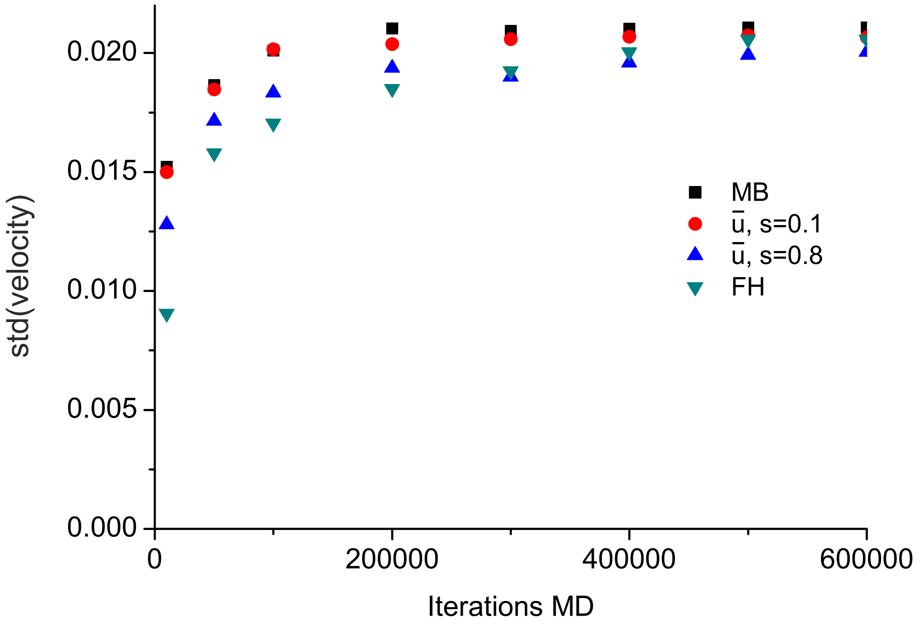

Figure 3.17: Standard deviation of velocity x component of the pure MD phase (MB) $\sum_p u_{xp}$, FH phase u_x and coupled system's mixture velocity $\tilde{u}_x$

The difference between the velocity of the mixture $\tilde{u}_x$ and the MD phase $\sum_p u_{xp}$, Fig. 3.18, shows that when $s = 0.1$ the difference is small, that means the velocities follow each other in both phases, while for $s = 0.8$ the difference is significantly larger and have complicated dynamics signifying the largely independent time evolution of the velocities.

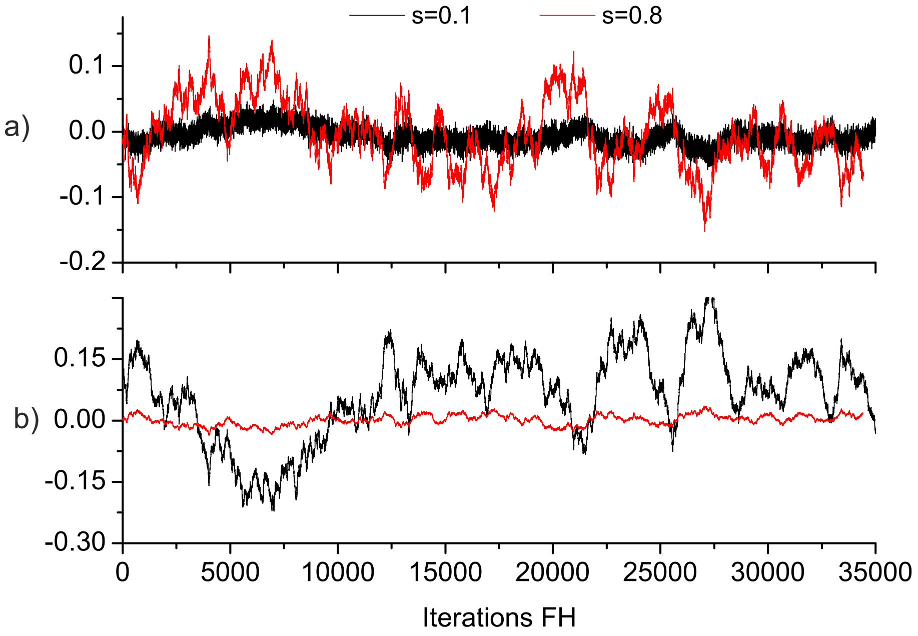

Figure 3.18: The difference between the mixture and phase velocities a) $\tilde{u}_x - \sum_p u_{xp}$ and b) $\tilde{u}_x - u_x$ for $s = 0.1$ and $s = 0.8$

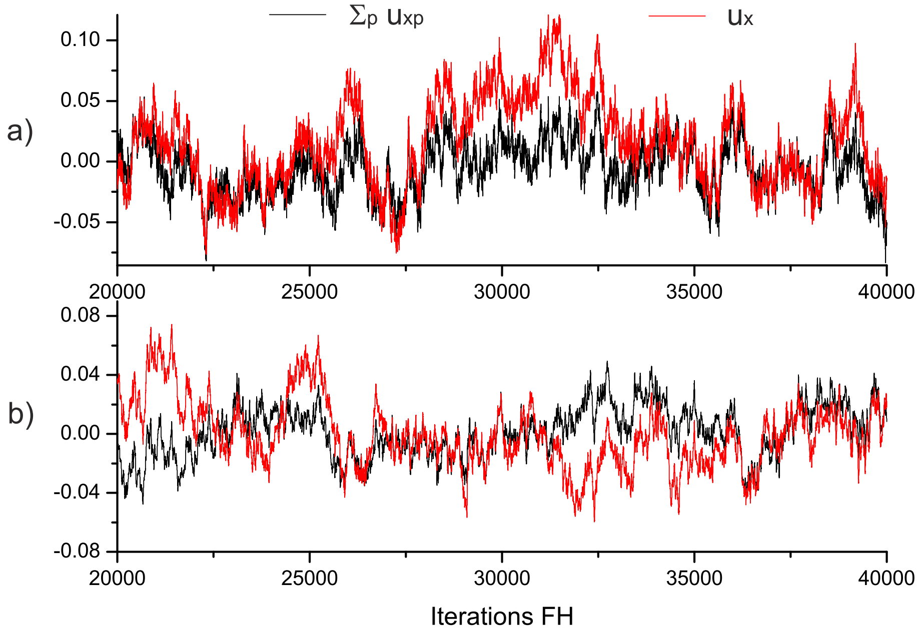

Figure 3.19: Velocity x component profiles of the MD phase $\sum_p u_{xp}$ and FH phase u_x; 'two way' coupling, BN2D water model; a) $s = 0.1$, b) $s = 0.8$

The effect of coupling, Fig. 3.18 and Fig. 3.19, shows that $\tilde{u}$ inherits fluctuations of the FH phase when $s \to 1$ and MD phase when $s \to 0$. As well as each phase velocities follow different pattern Fig. 3.19 for the different coupling parameter s values .

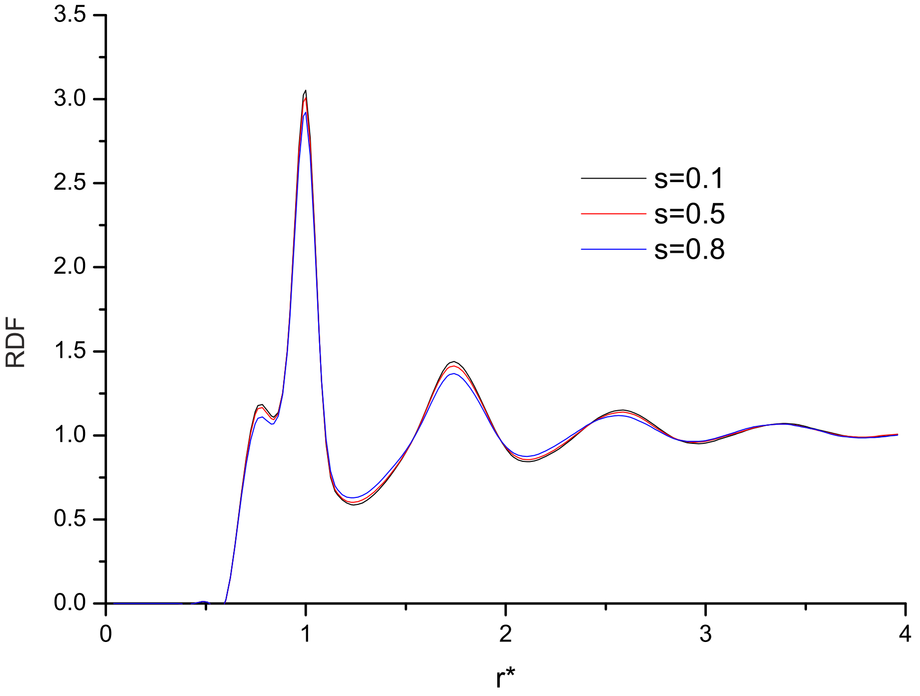

Figure 3.20: Radial distribution function of BN2D water model for different coupling parameter s values

The radial distribution function of the molecules, Fig. 3.20, remains the same as for the MB model without coupling. This means that the external force field, the 'coupling', does not affect the distribution of the MB molecules in local neighbourhood.

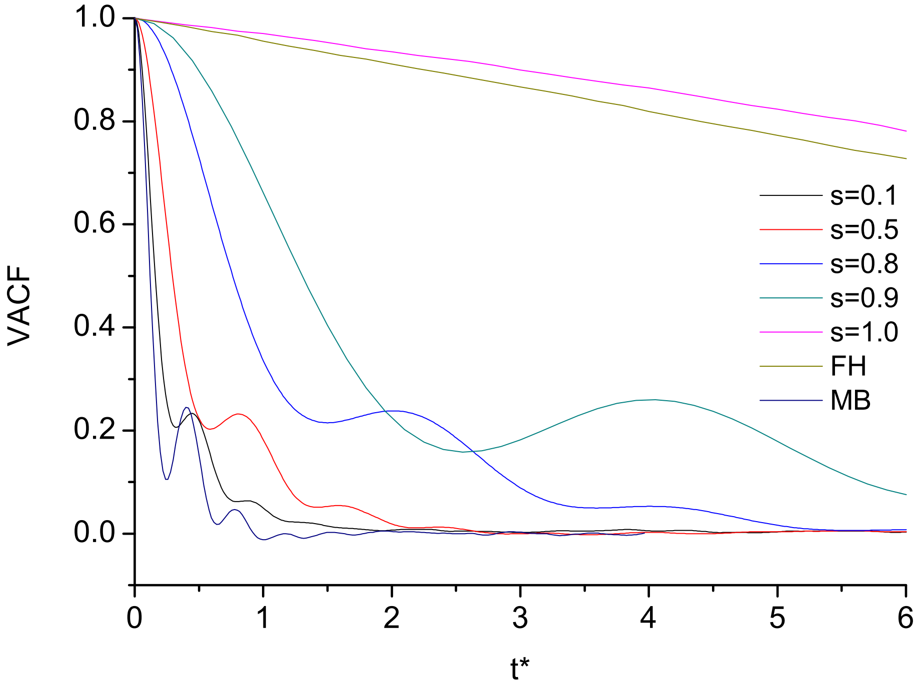

Figure 3.21: Translational velocity autocorrelation function for different s values calculated from the particles velocities

As was noted before, translational velocities of the MB particles are coupled with the LL-FH velocities, leaving the rotational degree of freedom uncoupled. The consistent representation of rotation is not available/required in the LL-FH framework. The angular velocity of MB particles was controlled using angular velocity rescaling to maintain the set temperature.

The translational velocity autocorrelation function (VACF) calculated using the actual particle's velocity $\frac{dx_{ip}}{dt}$, (2.42), is shown in Fig. 3.21. For larger values of the coupling parameter s VACF becomes more stretched in time and in the limits $s \to 0$ and $s \to 1$ it approaches the corresponding VACFs of the pure MD and LL-FH simulations.

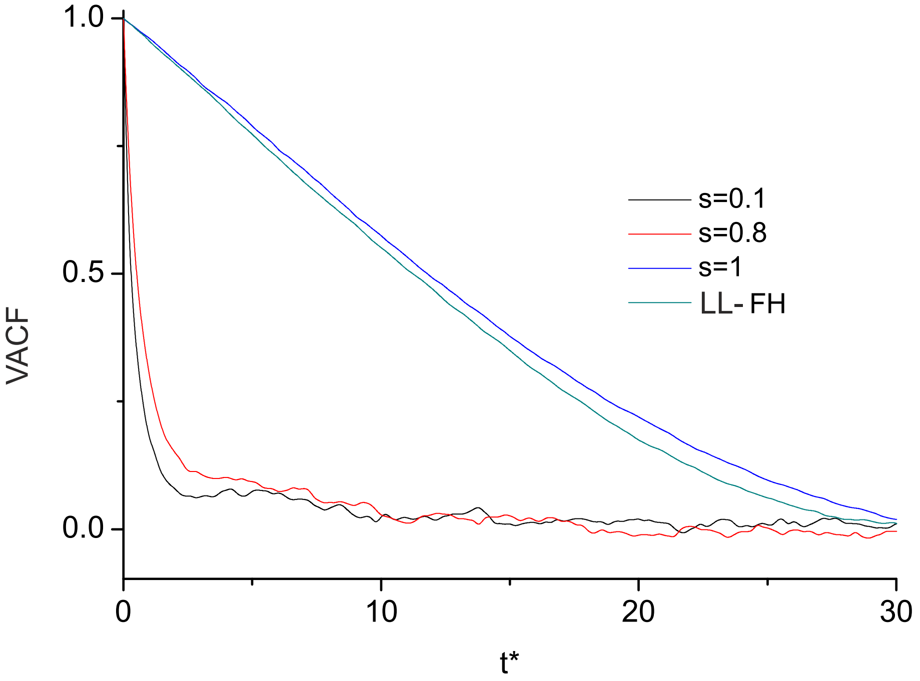

Figure 3.22: Translational velocity autocorrelation function for different s values calculated from the $\tilde{u}$ velocity fluctuations in the cell centres

The cell averaged (phase) fluctuations of the velocity, $\tilde{u}$, were used to calculate the translational velocity autocorrelation function (VACF) of Fig. 3.22. As can be seen the limiting case $s = 1$ for the coupled system produces similar VACF to the classical LL-FH model [61], while for $s \neq 1$ the faster decay of correlations signifies the dynamical properties of the liquid similar to the atomistic MD representation.

With the increase of the coupling parameter s VACF calculated from the velocities of particles Fig. 3.21 tends to the cell averaged $\tilde{u}$ VACF Fig. 3.22.

The velocity autocorrelation function and radial distribution function analysis show, that with the increase of the coupling parameter s MD particles loose their ability to move independently in the 'external force field' (due to the coupling) and eventually at the limit $s \to 1$ we get the 'static structure' of MD particles moving with the FH phase velocity.

Unfortunately, regardless the ability of BN2D water model to be in qualitative agreement with the real water and mimic its anomalous properties, BN2D water model implementation in biomolecular simulations is limited due to the two-dimensionality.

3.2.3 Conclusions

The results presented here reiterated that BN2D water model mimics real water anomalous properties.

We showed that different values of σ^*_{HB} for the orientational part of the MB water potential dramatically change the structural and dynamical properties. The changes lead to unnatural solid phases or liquid phases with abnormal structural and dynamical properties that deviate from the real water properties.

For the first time thermodynamic formulas for the BN2D water model were derived when NVE ensemble is used. Also we derived equations of motion for the BN2D water model when NPT ensemble is used.

We also showed, that the calculation of pressure in the NVE and NPT ensembles is different. In the NVE ensemble full kinetic energy is used, while in the NPT ensemble rotational part is excluded. Our simulation results confirm the correctness of the obtained formulas which produce the same thermodynamic state for the different ensembles.

Also we have studied dynamic properties of the BN2D water model, that was not reported before.

The benefits of the investigated model are most obvious for very large systems approaching hydrodynamic scales because the model will allow direct atomistic verification of the whole system.

We demonstrated, that the coupling approach based on the two-phase modelling, Landau Lifshitz- Fluctuating Hydrodynamics and Molecular Dynamics simulations can be successfully applied to the BN2D water model.

We showed, that the fluctuations of the velocities and densities of one phase can be smoothly enforced on the other, thus constituting the macro- and micro- scale coupling.

Also we showed, that the structural properties, the radial distribution function for MB particles, is not affected by the coupling.

With the increase of the coupling parameter s the velocity autocorrelation function (VACF) for MB particles tends to the pure FH phase VACF and the FH phase VACF tends to the pure MB water model VACF.

In the next chapter we present the application of the proposed coupling method to three-dimensional systems, including a popular SPC/E water model . Also a variable profile of the parameter s is discussed.

3.3 SPC/E water model implementation of the hybrid framework

Here we reiterate the importance of biomolecular systems simulations and focus on the SPC/E water model in the context of proposed coupling method.

As we mentioned in the introduction, the dynamics of proteins in water can be investigated by analysing the collective motion of particles in a liquid or biomolecular solutions. In this case glassy dynamics can be employed, where large domains consisting of water and biomolecules are found to move as a whole with very different dynamics in different domains [85]. Similarly, Umezawa et al. [86] reported that on a surface of a protein a coherent behaviour of large conglomerates of water molecules, microscopic “water vortices”, can be observed. It is now commonly recognised, that surrounding solvent molecules play important role in the process of protein folding [8]. Recent investigations demonstrate the connection between water molecules dynamics in the vicinity of the proteins and protein conformations motions [9]. According to the study, protein chains are guided by the water hydration shell at the periods of major conformation rearrangements. The ability to predict and control this guidance, which drives protein to a particular conformation, is highly demanded, because it defines all the properties and functionality of the protein. Since in these processes the range of scales spans several orders of magnitude, coupling method studied here can be employed. We have shown, that this coupling method is free from the problem of destroying and introducing atoms when crossing the atomistic/continuum interface zone, in contrast to other hybrid Molecular Dynamics/Hydrodynamics methods, which are based on the mass and momentum flux through the interface zone.

In the previous sections, coupling or communication between the large and small scales was successfully implemented, for 2D liquid argon and BN2D water model. Now the proposed coupling method can be applied to the realistic three-dimensional SPC/E water model, which is in qualitative and quantitative agreement with experiment [3].

3.3.1 Model and details of computation

The SPC/E water model represents water as a triatomic molecule with rigid bonds, Fig. 3.23, where red and white balls indicate oxygen and hydrogen atoms with relevant charges, respectively. The dashed line circle signifies the effective size of the molecule.

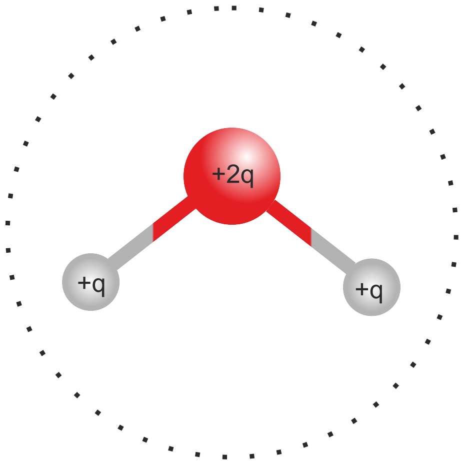

Figure 3.23: SPC/E water model representation

The interaction potential of the SPC/E water molecule is described by the following combination of energies

$$E_{total}(r^N) = E_{disp} + E_{LRC} + E_{coulomb}, \tag{3.54}$$

where on the right hand side the first is the pair dispersion energy, the second is the long-range correction to the pair dispersion energy, and finally the Coulomb potential energy. More details on this model can be found in [51].

The results in this section were obtained in collaboration with Cambridge University and Queen Mary University of London colleagues Dr Sergey Karabasov, Dr Anton Markesteijn and Dr Ivan Korotkin, who have incorporated the 'one way' coupling in the GROMACS [52] code as an add-on.

Basically, in the time loop ('md.c' file) new routines were inserted for the calculation of the FH phase densities and momentum and collection of the statistics. In the 'update.c' file velocity and coordinates evaluation routines were replaced with the new equations of motion that were obtained in the previous chapters ('one way' coupling).

This add-on allows to do serial and parallel [87] computing with the majority of available water models and peptides. Also GROMACS has multiple tools for analysis, which are very useful for the further studies.

SPC/E water model available in GROMACS 4.6.5. was used in simulations. Standard conditions were applied in the NVT ensemble simulation, with temperature $T = 298.15[K]$. The timestep $dt = 0.25 fs$. Velocity rescaling was used with relaxation parameter set to 100 times bigger than the timestep. More details on the velocity rescaling can be found in GROMACS 4.6.5 manual, pages $31-32$ [52]. The coupling parameters were $\alpha, \beta = 1000 \left[\frac{nm^2}{ps}\right]$, that in dimensionless units are $\alpha^*, \beta^* \approx 15600$. For a set of constant values of the coupling parameter s and 9000 molecules.

As we mentioned before an interpolation is used in the regions between the grid points. In order to increase the accuracy of the interpolated data, our colleagues replaced linear interpolation with the cubic spline interpolation.

3.3.2 Cubic spline interpolation

The cubic spline interpolation can be better demonstrated by a one-dimensional example. Assume that on a line four values are available a_{-1}, a_0, a_1, a_2, then the interpolated value at the local position t that is in the range $[0;1]$ is obtained using the following expression

$$p(t) = \frac{1}{2} \begin{pmatrix} 1 & t & t^2 & t^3 \end{pmatrix} \begin{pmatrix} 0 & 2 & 0 & 0 \\ -1 & 0 & 1 & 0 \\ 2 & -5 & 4 & -1 \\ -1 & 3 & -3 & 1 \end{pmatrix} \begin{pmatrix} a_{-1} \\ a_0 \\ a_1 \\ a_2 \end{pmatrix}$$

This procedure is applied for each dimension.

The difference between the linear and cubic spline interpolation for the u_x velocity is shown on Fig. 3.24 and Fig. 3.25.

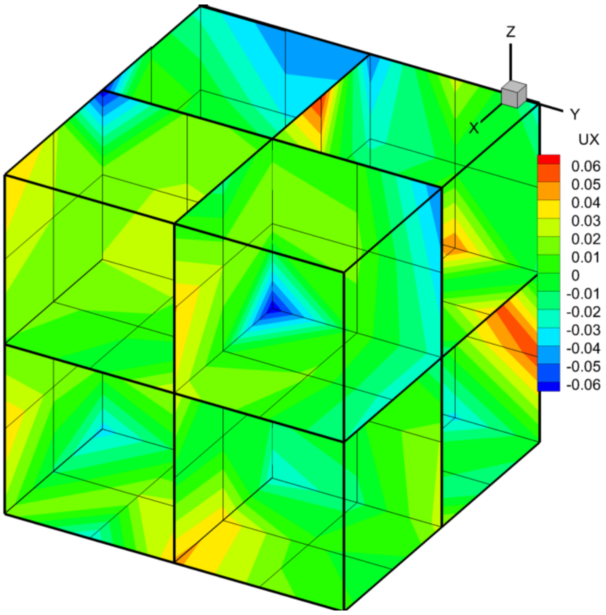

Figure 3.24: Three-dimensional linear interpolation of the velocity component u_x

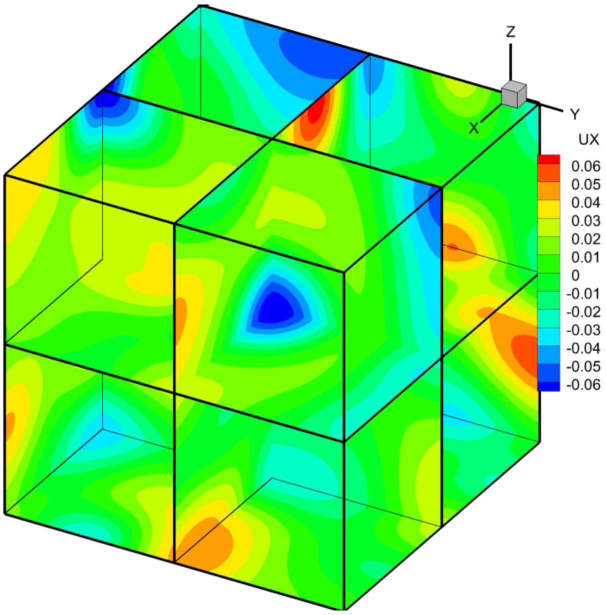

Figure 3.25: Cubic spline interpolation of the velocity component u_x

This improves the accuracy of the terms related to the phase densities and the velocities in the region between the grid points, which are used in the equations of particle's motion. Consequently, particles in the region between the grid points experience smoother change of the external force field, which is due to the applied coupling.

3.3.3 Finite size of the water molecules

Before the water model is implemented in terms of the 'one way' coupling method, the existence of pulsations of the MD phase densities and velocities must be discussed.

As we suggested before, these pulsations lead to the higher values of standard deviations. To verify that, an advanced mapping technique of the small scales to the large scales or the 'blob' filter is applied [1], which effect can be demonstrated on the change of the MD phase fluctuations as well as values of the standard deviations.

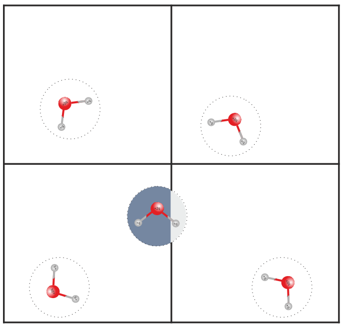

Figure 3.26: Contributions of a particle to the MD phase density and momentum is calculated as a fractions of its volume d_{mol}^3 in different cells

This filter was initially developed for TIP3P water molecules, although it can be applied even to the monoatomic argon in order to reduce the pulsations. This method employs an assumption, that the atom is not a point particle, hence it occupies a certain volume. Thus, a characteristic volume must be assigned to each molecule, for the TIP3P water molecule Voulgarakisand et. al. [1] proposed to use $d_{mol} = 2.4$ Å, which is also used in this section. In this case if a molecule partially crossed the cell's border, then its presence must be accounted for in both cells. In other words, the contributions of a particle to the MD phase density and momentum is calculated as a fractions of its volume d^3_{mol} in different cells Fig. 3.26. The effect of this technique on the SPC/E water model MD phase fluctuations is illustrated in Fig. 3.27 and Fig. 3.28.

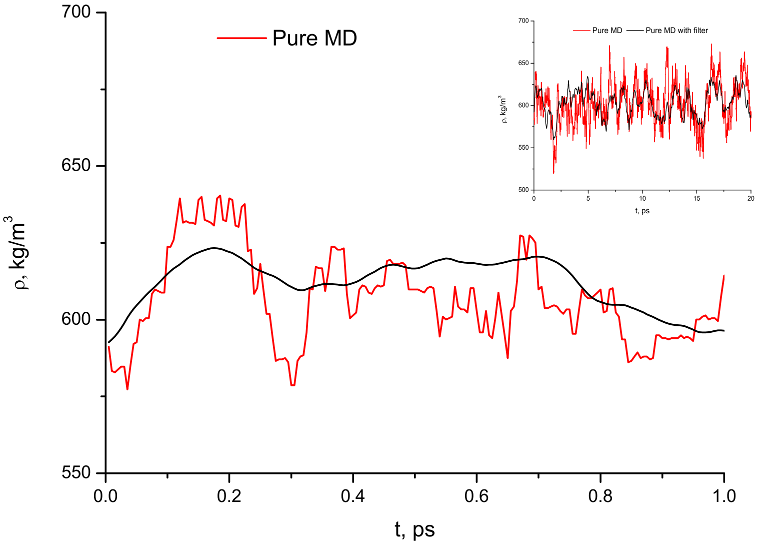

Figure 3.27: SPC/E water model MD phase density fluctuations in a random cell with and without 'blob' filter

It can be seen that the pulsations in the cells are smaller, although the velocity fluctuations are not affected as much as the density fluctuations. This is because the MD phase density is calculated by an amount of migrated particles between the cells, while the velocity fluctuations do not required particles to leave or enter a cell to change the value.

Overall, the 'blob' filter smoothes the pulsations of the MD phase densities and velocities, hence minimizes 'jumps' of the MD phase, when molecule migrates from one cell to another.

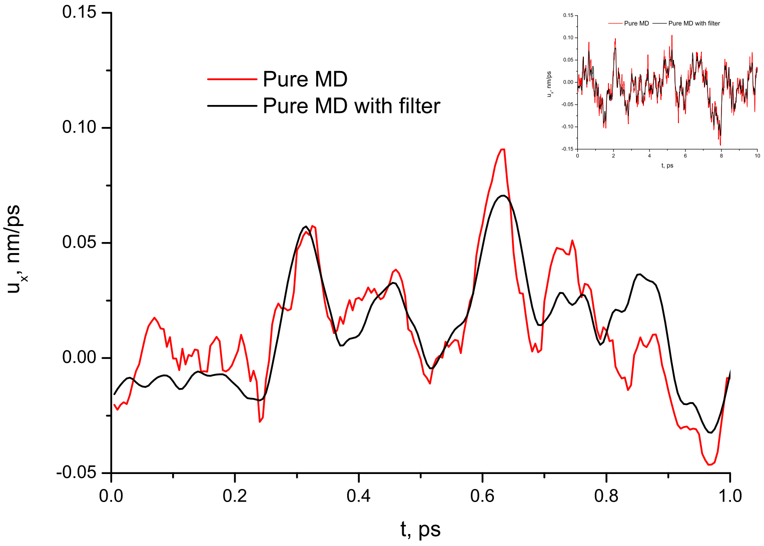

Figure 3.28: SPC/E water model velocity x component fluctuations in a random cell with and without 'blob' filter

As we reported in the previous sections the standard deviations for the pure MD phase are higher than for the coupled systems or the pure FH phase. After the 'blob' filter is applied the standard deviations become smaller due to the elimination of the pulsations, Fig. 3.29 and Fig. 3.30, where the pure MD systems are simulated with and without the 'blob' filter.

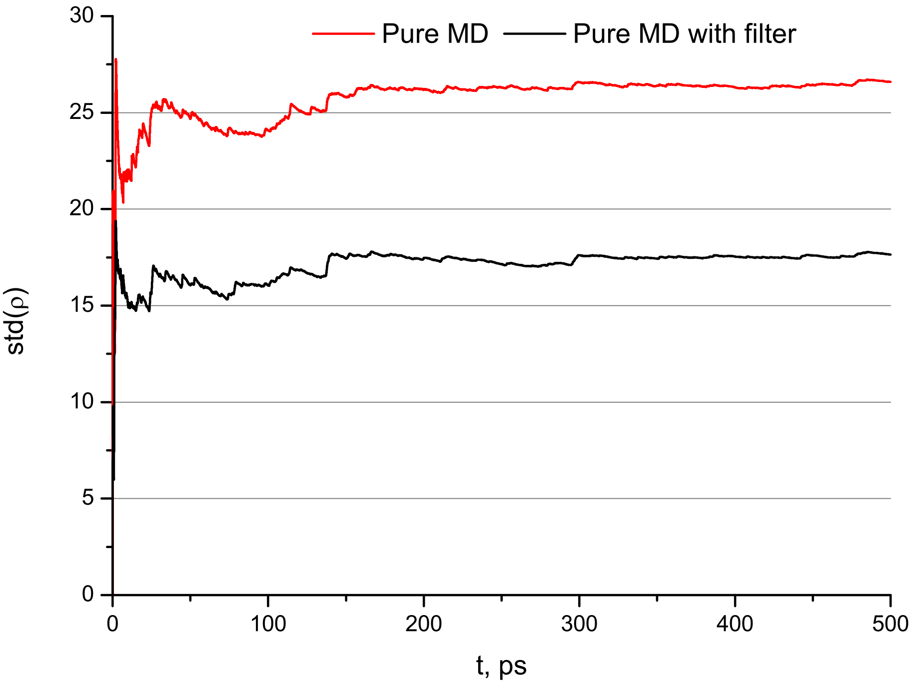

Figure 3.29: Standard deviation of the SPC/E water model MD phase density fluctuations with and without 'blob' filter, where ρ is measured in $\frac{Da}{nm^3}$

The standard deviations for the 3D systems can be estimated using classical relationships [61], which are as follows: for the density

$$std(\rho) = \frac{1}{c_T}\sqrt{\rho k_B \frac{T}{V_{cell}}}, \tag{3.55}$$

where c_T is the speed of sound and V_{cell} is the cell's volume.

The standard deviation of the velocity in the 3D case can be estimated using relationship

$$std(u) = \sqrt{k_B \frac{T}{\rho V_{cell}}}, \tag{3.56}$$

in general there is no difference in the statistical sense between the velocity components and the velocity magnitude, thus we calculate standard deviations for the velocity x component.

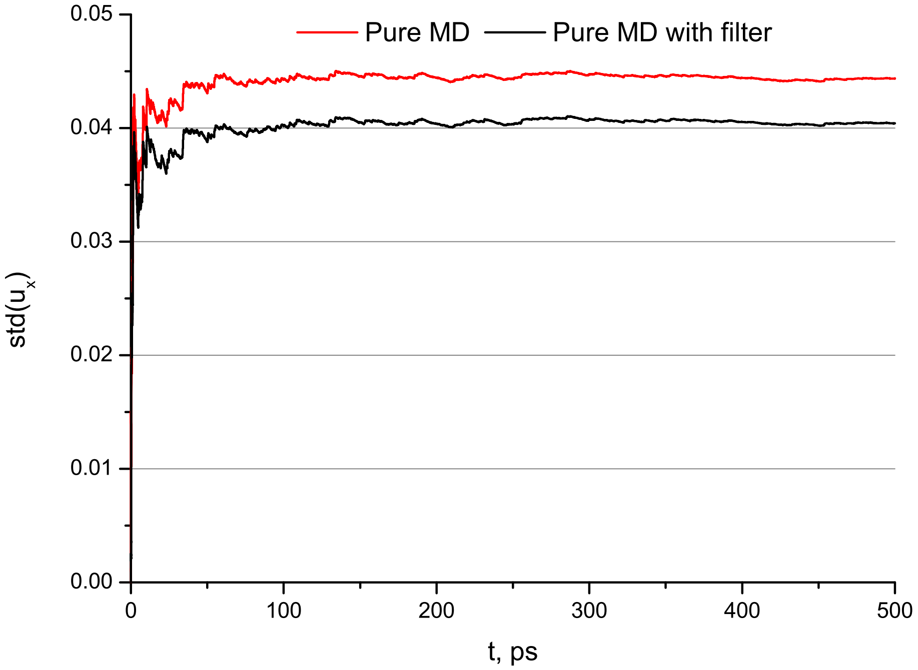

Figure 3.30: Standard deviation of the SPC/E water model MD phase x velocity component fluctuations in $\frac{nm}{ps}$ with and without 'blob' filter

According to the formulas above, the standard deviation of the MD phase density must be approximately $18\frac{Da}{nm^3}$ and the velocity $0.04\frac{nm}{ps}$, that is very close to the value obtained with the 'blob filter'.

3.3.4 Pure water

Further results are presented for the SPC/E water model with the 'blob' filter.

As we predicted, the SPC/E water trends are the same as for the other models studied in the previous sections, when the coupling was applied.

Close order analysis shows that water molecule's radial distribution functions of the oxygen-oxygen and oxygen-hydrogen do not change with the coupling method Fig. 3.31 and Fig. 3.32.

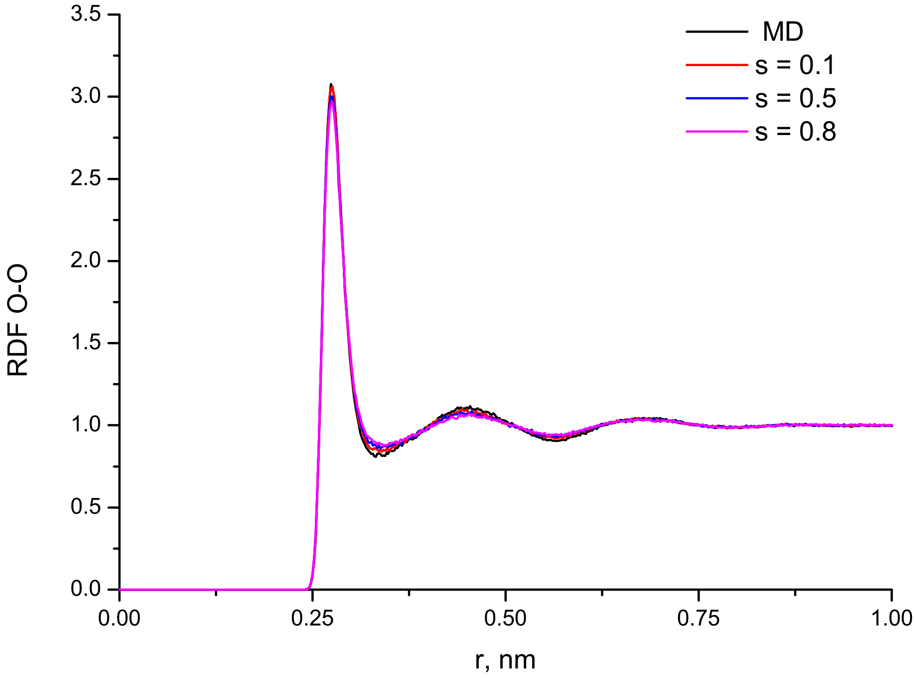

Figure 3.31: Radial distribution function of SPC/E water model $O-O$ (oxygen-oxygen)

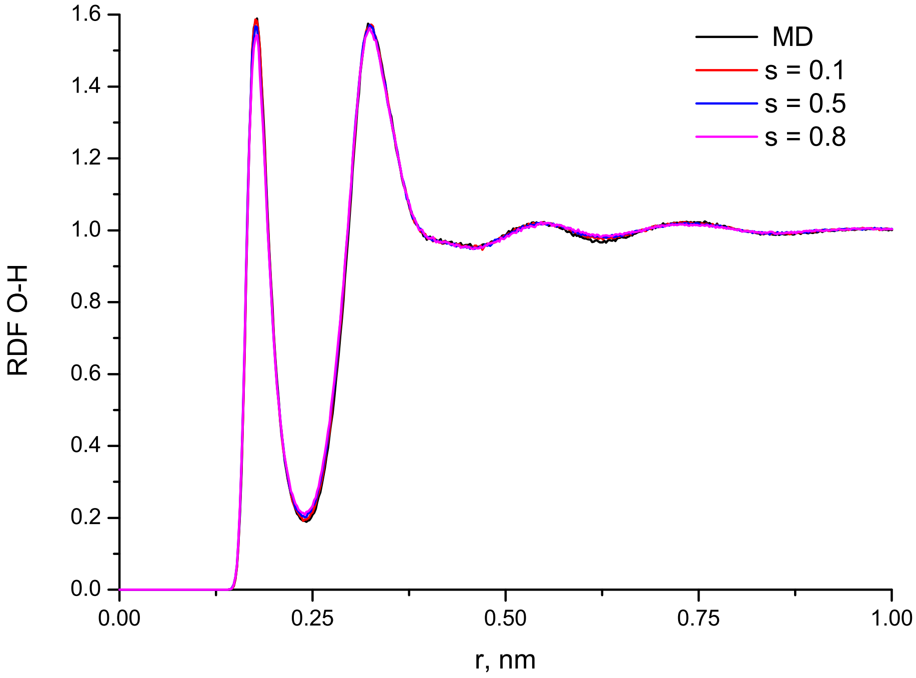

Figure 3.32: Radial distribution function of SPC/E water model $O-H$ (oxygen - hydrogen)

The dynamical properties of the model changed in the same manner, Fig. 3.33, as for 2D models in the previous sections, with the increase of the coupling parameter s VACF gets stretched and tends to the FH phase VACF.

When the coupling parameter s is small VACF resembles standard SPC/E water model VACF and when the coupling parameter s gets larger VACF becomes more and more similar to the pure

FH phase VACF. Especially, when $s = 1$ VACF of the MD particles is the same as FH phase.

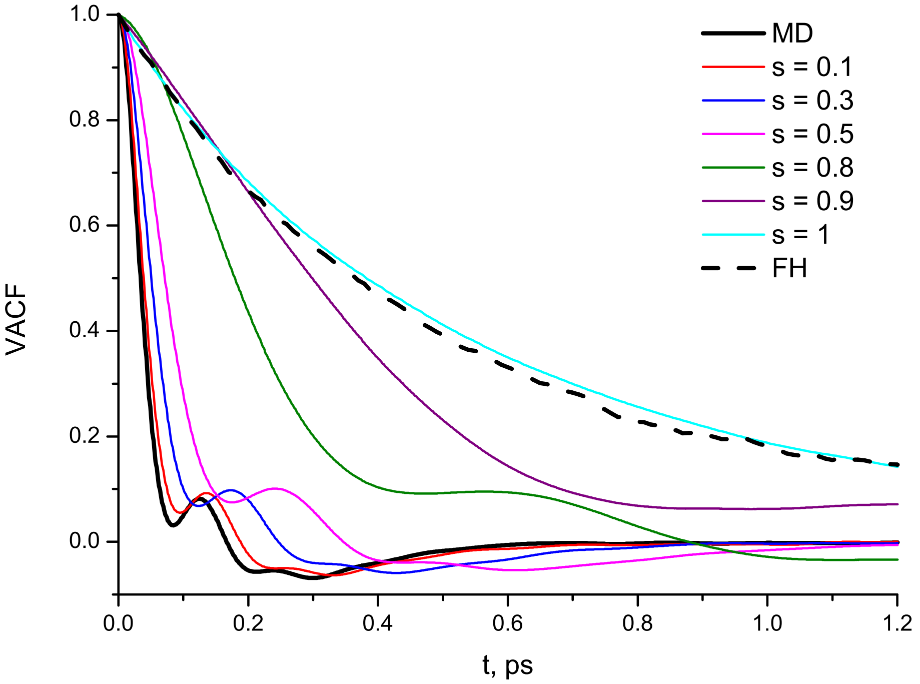

Figure 3.33: Velocity autocorrelation function of the SPC/E water model particles for different parameter s

That means that α^*, β^* parameters were chosen large enough to demonstrate the effect of the coupling and small enough to do not disrupt the close order between the molecules.

As a result, water molecules with increase of the coupling parameter s inherit bulk water dynamical properties and preserve close order, which is unique for each model. It means that particles experience collective motion that is characteristic to the continuum, when s is large.

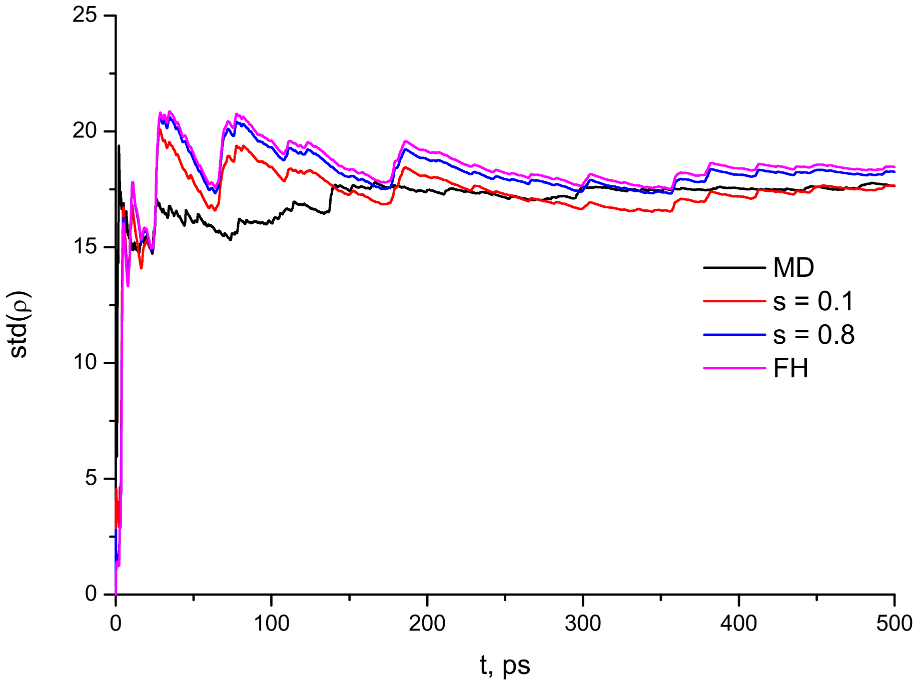

Figure 3.34: Standard deviations of the density for the pure and coupled system of SPC/E water model MD phase with different parameter *s*

When the 'blob' filter is used, the standard deviations are very close to the coupled and pure phases, Fig. 3.34 and Fig. 3.35, although the MD phase density fluctuations *std's* are slightly smaller, than the pure FH phase. In order to adjust the *std* values to the theoretical one, (3.55) and (3.56), the occupied volume by a molecule d_{mol}^3 must be changed. The larger volume is decreasing, while the smaller volume is increasing the *std* value.

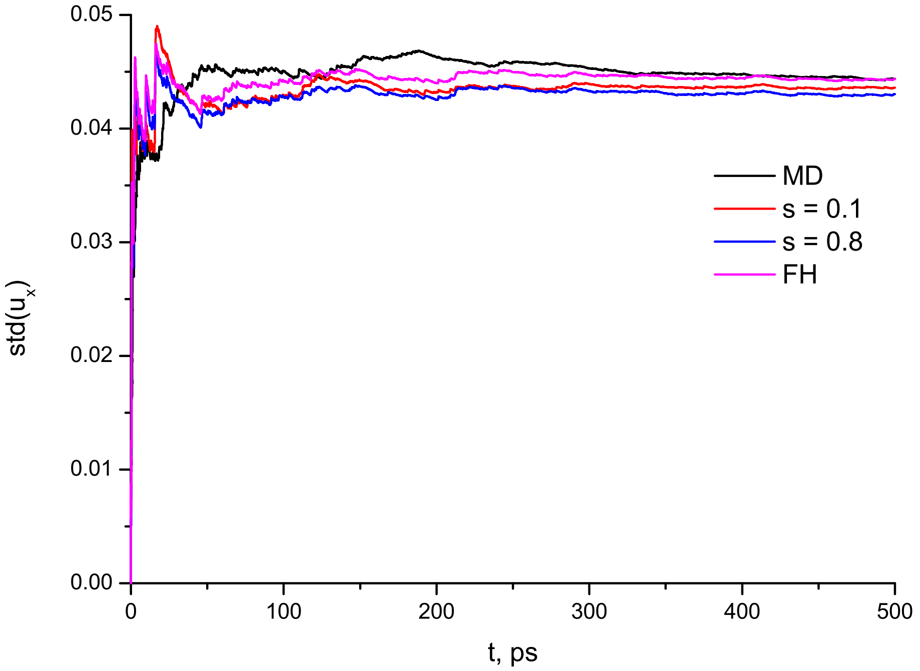

Figure 3.35: Standard deviations of the velocity *x* component for pure and coupled system of SPC/E water model MD phase with different parameter *s*

Summarizing, the SPC/E model was tested using GROMACS with the ‘one way’ coupling add-on and obtained that the same trends as for the other models studied in this work. We have demonstrated, that the coupling can be improved if ‘blob’ filter [1] is implemented, which reduces pulsations of the fluctuations of the MD phase densities and velocities. This yields more accurate standard deviations of the MD phase fluctuations.

To study peptides or proteins in solvent a variable profile of the parameter s is required, such that in the center in the vicinity of the peptide $s = 0$ and gradually changes to the edges, where $s = 1$ and represents bulk water.

3.3.5 Variable coupling parameter s

We have tested a sphere type profile of the coupling parameter s for the 3D liquid argon. Where in the sphere centre $s = 0$ was pure MD phase and at the edges $s = 1$ pure FH phase. The test provided similar trends with respect to the magnitude of the coupling parameter s for the statistics as well as VACF and RDF. Where s is large VACFs are stretched along the time axis and for small values of s VACFs resemble pure argon. The RDF curves are the same and correspond to the pure argon in each cell regardless the value of s.

Furthermore, if the sphere type profile of the parameter s is used, then MD particles close to the $s = 1$ border can stick to the FH phase and leave a vacancy in its previous position. In the region $s = 1$ MD particles do not interact between each other, hence they are dragged by the FH phase without resistance. Consequently, when MD particles stick to the FH phase collectively, empty areas appear in the region, where $s \neq 1$. Although, after certain period of time MD particle return back to the region where $s \neq 1$. This effect is not visible in the MD particles close order (RDF) analysis, since it is a macroscale effect.

Initially, particles in the center were marked in red colour, where $s = 0$, gradually changing colour to blue on the edges, where $s = 0.99$, Fig. 3.36.

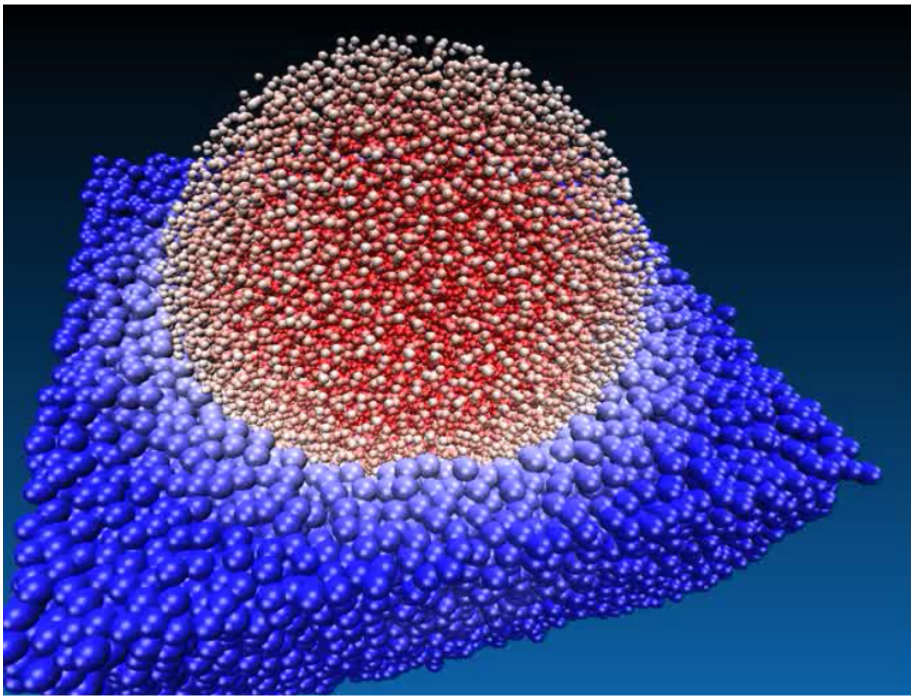

Figure 3.36: 3D liquid argon with sphere type profile of the coupling parameter s. Initially, particles in the center were marked in red colour, where $s = 0$, gradually changing colour to blue on the edges, where $s = 0.99$ (view of a slice)

The size of the particles at the edges is bigger than particles, which are at the center region. Thus, we illustrate that the behaviour of the particles is more inert, when they are located in the regions with the larger s values. At the edges movement of the particles is 'jelly'-like (smooth and slow) while at the center region the particles are 'lighter' and moving much faster.

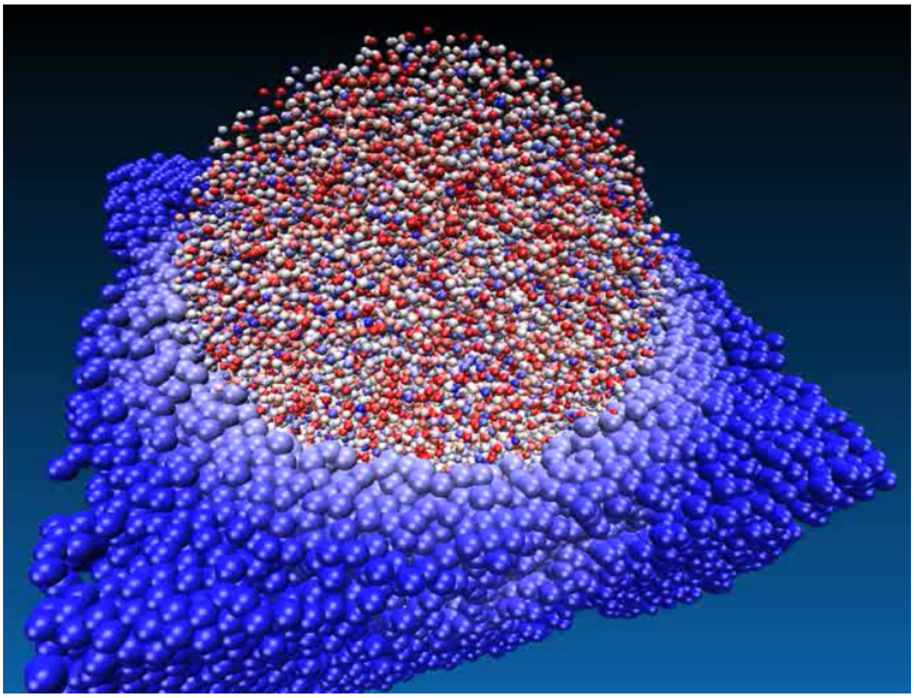

Figure 3.37: A snapshot of the simulation of 3D liquid argon with sphere type profile of the coupling parameter s. Initially, particles in the center were marked in red colour, where $s = 0$, gradually changing colour to blue on the edges, where $s = 0.99$ (view of a slice)

As can be seen some red particles can migrate to the edges and stick to the large s region for a while Fig. 3.37. Contrary, the blue particles increase their kinetic energy while moving towards the center.

This is demonstrated on the video of 3D liquid argon with the sphere type profile of the coupling parameter s on the CD: file name '5.1.Dr.I.Korotkin. 3D liquid argon (sphere profile s).mpg'.

3.3.6 Peptide in water

When peptide is introduced in water it is important to position the sphere profile of the coupling parameter s at the peptide's geometrical center, since its representation in the LL-FH is not available. The size of the $s = 0$ region must be large enough to encompass the peptide with surrounding water.

A small system is simulated, which consists of dialanine [88] and 1444 SPC/E water molecules. Standard conditions with thermostat are used, resulting in the NVT ensemble. Timestep $0.001\,[ps]$, coupling parameters are set to $\alpha, \beta = 1000 \left[\frac{nm^2}{ps}\right]$. The coupling parameter s is zero for 40% of the simulation domain and positioned at its center. Then coupling parameter s gradually (linear) increases to 0.99 at the edges, Fig. 3.38.

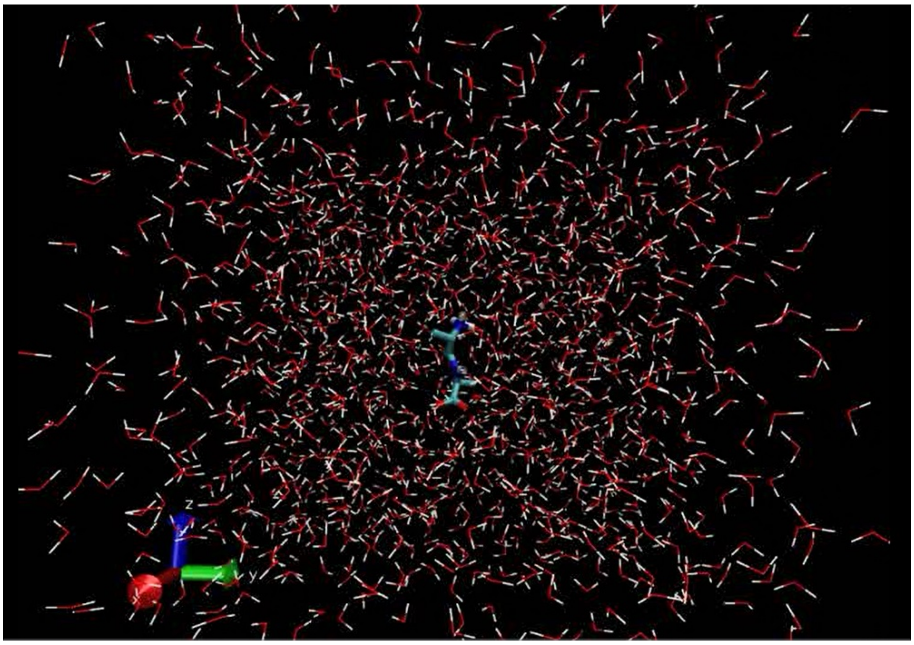

Figure 3.38: Initial distribution of dialanine and 1444 SPC/E water molecules in simulation using variable coupling parameter s profile. Parameter s is zero for 40% of the simulation domain and positioned at its center. Then parameter s gradually (linear) increases to 0.99 at the edges

The water molecules in the vicinity of the dialanine move quickly, while at the edges their movements are 'jelly'-like (smooth and slow).

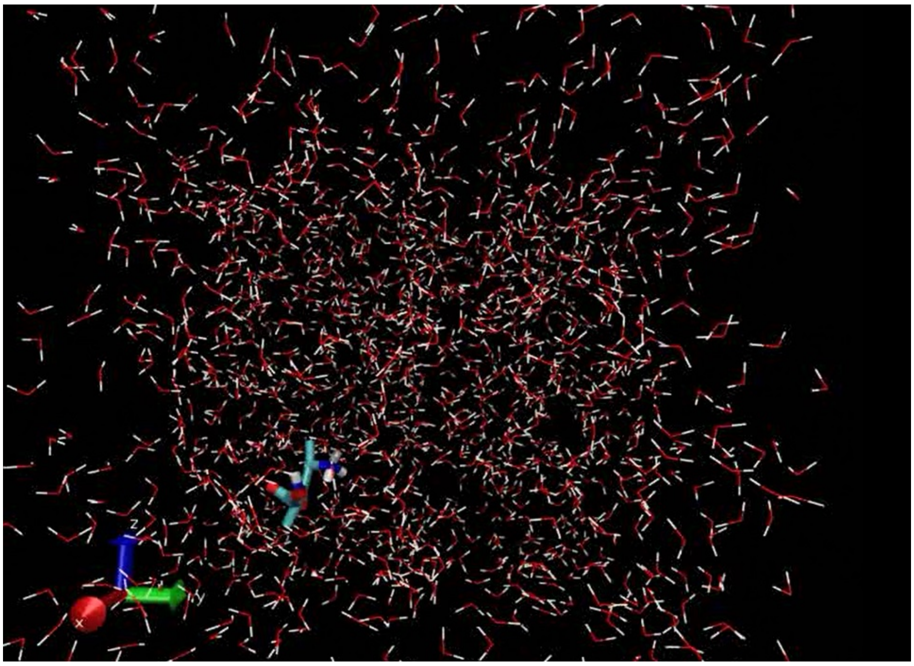

Figure 3.39: A snapshot of distribution of dialanine and 1444 SPC/E water molecules in simulation using variable coupling parameter s profile. Parameter s is zero for 40% of the simulation domain and positioned at its center. Then parameter s gradually (linear) increases to 0.99 at the edges

We have noticed, that after some time peptide is dragged to the simulation domain outskirts, if it gets in the region, where $s \neq 0$, Fig. 3.39. In this case the peptide starts to experience forces from the FH phase, which eventually leads the simulation to crash. This is due to the lack of the peptide representation in the LL-FH simulation. As we mentioned already, in order to overcome this issue, $s = 0$ region must be large enough to include studied object (peptide) and water molecules as well as its center must be connected to the object's (peptide) geometrical center.

Video demonstration of the simulation when sphere type profile of the coupling parameter s is fixed in the center of the simulation domain is available on the CD: file name '5.2.Dr.I.Korotkin. dialanine and 1444 SPCE water (fixed sphere type s).mpg'.

A larger system, dialanine and 30000 SPC/E water molecules was simulated at the normal conditions with the timestep $0.001[ps]$. Nose-Hoover thermostat was used with the relaxation parameter set to $0.1[ps]$. Periodic boundary conditions were used with coupling parameters set to $\alpha, \beta = 20000\left[\frac{nm^2}{ps}\right]$. Sphere type profile of the coupling parameter s was used. Two simulations were conducted using 8 cores. In the first simulation (660 000 MD iterations) sphere center was fixed at the simulation domain center and in the second simulation (860 000 MD iterations) it was fixed to the dialanine center of mass.

Video demonstration of the first simulation is available on the CD: file name '5.3.Dr.I.Korotkin. dialanine and 30000 SPCE water (fixed sphere type s).mpg', which shows the same behaviour of the dialanine as for the smaller system (1444 SPC/E water molecules). Where peptide is dragged to the large coupling parameter s region.

The second simulation, where parameter s profile center is linked to the dialanine's geometrical center is demonstrated on the CD: file name '5.4.Dr.I.Korotkin. dialanine and 30000 SPCE water (moving sphere type s).mpg'. As we can see the sphere profile follows the dialanine.

Summarizing, the proposed coupling method can be used for the real size system simulation, such as protein immersed in the water.

4

Conclusions

CONTENTS

4.1 BN2D water model 125

4.2 Bridging large and small scales 125

4.3 Pure water 126

4.4 Variable coupling parameter s 127

4.5 Peptide in water 127

4.6 Outlook 127

4.1 BN2D water model

We have shown that BN2D water model mimics real water anomalous properties in both NVE and NPT ensembles. This qualitative agreement with the real water was already reported by [5] who used Monte Carlo simulation (NPT ensemble).

We showed that different values of σ^*_{HB} for the orientational part of the MB potential dramatically change the structural and dynamical properties. The changes lead to unnatural solid phases or liquid phases with abnormal structural and dynamical properties that deviate from the real water properties.

For the first time thermodynamic formulas for BN2D model were derived when the NVE ensemble is used. Also we derived equations of motion for BN2D model when the NPT ensemble is used.

We also showed, that the calculation of the pressure in the NVE and NPT ensembles is different. In the NVE ensemble full kinetic energy is used, while in the NPT ensemble rotational part is excluded. Our simulation results confirm the correctness of the obtained formulas that produce the same thermodynamic state for different ensembles.

We have studied dynamic properties of the BN2D model, that was not reported before. The obtained autocorrelation functions coincide with the ones from 3D realistic models, such as SPC. The minima on VACF and RVACF are located at approximately correct positions, which confirms the correctness of the values of the moment of inertia and mass. The moment of inertia of MB particle can be additionally adjusted such that RVACFs from SPC and MB models coincide even better.

The benefits of the investigated 2D model are most obvious for very large systems approaching hydrodynamic scales because the model will allow direct atomistic verification of the whole system, since computational costs are scaled with N^D, where N is the number of particles and D is the number of spatial dimensions.

4.2 Bridging large and small scales

We have successfully tested the framework of the coupling method between the MD and FH phases. These tests consisted of two parts. The ‘one way’ coupling and the ‘two way’ coupling. The first was incomplete in the context of communications between the phases (only MD phase fluctuations changed), while the former showed substantial changes in the both phase fluctuations (thus communication is fully implemented).

We showed, that the fluctuations of the velocities and densities of the phases can be smoothly enforced on each other, thus constituting the large and small scale coupling.

We also estimated and made recommendations for the lower limit of the parameters used in the coupling methods.

We investigated structural and dynamical properties resulting is a conclusion that for the larger values of the coupling parameter s the MD particles motion is affected by the external field due to the coupling.

We showed that the structural properties, such as Radial Distribution Function of particles is not affected by the coupling.

We demonstrated that with the increase of the coupling parameter s the velocity autocorrelation function (VACF) of particles tends to the pure FH phase VACF and the FH phase VACF tends to the pure MD phase VACF.

We showed that coupling approach based on the two-phase modelling, Landau Lifshitz- Fluctuating Hydrodynamics and Molecular Dynamics simulations can be successfully applied to the liquid argon, BN2D and SPC/E water models.

We provide with a good estimation of the coupling parameters α^*, β^* values for the 2D liquid argon, BN2D and SPC/E water models. The values are large enough to demonstrate the coupling effect and small enough to do not change the RDF of the particles and produce artifacts.

We presented results obtained in collaboration with Cambridge University and Queen Mary University of London colleagues, who have incorporated the ‘one way’ coupling in the GROMACS code [52] as an add-on.

The ‘blob’ filter [1] was used which smooths transition of the particles from cell to cell and eventually eliminates pulsations that are present in the density and velocity fluctuations of the MD phase. We showed that these pulsations lead to the higher values of the standard deviations of the densities and momenta.

4.3 Pure water

The SPC/E water model was tested using the ‘one way’ coupling and showed the same trends as for the liquid argon and BN2D water model.

We showed that SPC/E water molecules with the increase of the coupling parameter s inherit bulk water dynamical properties and preserve close order (RDF), which is unique for each model. It means that particles experience collective motion that is characteristic to the continuum, when s is large.

4.4 Variable coupling parameter s

We have presented a sphere type profile of the coupling parameter s for 3D liquid argon. Where in the sphere centre $s = 0$ was the pure MD phase and at the edges $s = 1$ pure FH phase. The test provided similar trends with respect to the magnitude of the coupling parameter s for the statistics as well as VACF and RDF.

We demonstrated that MD particles can migrate from the center to the edges of the simulation domain and stick to the large coupling parameter s region for a while and then return back to the $s \neq 1$ region.

We have shown that the MD particles, which are located in the larger coupling parameter s region are more inert, then those in the region of the smaller s. At the edges the movement of the particles is 'jelly'-like (smooth and slow) while at the center region the particles are 'lighter' and moving much faster.

Overall, method investigated in this work encompasses regions with the atomistic description and transition zone (overlap-region), where the last can be naturally joined with the continuum models, thus increase geometrical size of the system, that results in the substantial reduction of the degrees of freedom and computational costs.

4.5 Peptide in water

When peptide is introduced in the water it is important to position the sphere profile of the coupling parameter s at the peptide's geometrical center, and large enough to encompass peptide, since its representation in the LL-FH is not available.

We have noticed, that if peptide gets in the region, where $s \neq 0$, it starts to experience forces from the FH phase, which eventually drag the peptide to the $s = 1$ region and leads the simulation to crash.

4.6 Outlook

For the further development of the method the following points must be addressed:

1. A 'two way' coupling must be incorporated into the GROMACS.
2. Non-equilibrium or non- adiabatic systems can be studied if energy equation is integrated in LL-FH simulation.
3. The time lapse in both the MD and FH representations must be scaled.

Summarizing, the coupling method is effective for the communication between the large and the small scales, it is free from the problem of destroying and introducing atoms when crossing the atomistic-continuum interface zone, contrary to other hybrid Molecular Dynamics/ Hydrodynamics methods, it preserves geometrical size of the system and it is not limited to a particular interaction potential.

Bibliography

[1] N. K. Voulgarakisand and J.-W. Chu, “Bridging fluctuating hydrodynamics and molecular dynamics simulations of fluids,” *The Journal of Chemical Physics*, vol. 130, 2009.

[2] S. Fritsch, S. Poblete, C. Junghans, L. D. Site, and K. Kremer, “Adaptive resolution molecular dynamics simulation through coupling to an internal particle reservoir,” *PRL*, vol. 108, p. 170602, 2012.

[3] G. S. Kell, “Density, thermal expansivity, and compressibility of liquid water from 0 to 150 deg. c. : Correlations and tables for atmospheric pressure and saturation reviewed and expressed on 1968 temperature scale,” *Journal Of Chemical and Engineering Data*, vol. 20, pp. 97–105, 1975.

[4] M. E. Tuckerman, *Statistical Mechanics: Theory and Molecular Simulation*. Oxford: Oxford University Press, 2012.

[5] K. A. T. Silverstein, A. D. J. Haymet, and K. A. Dill, “A simple model of water and the hydrophobic effect,” *J. Am. Chem. Soc*, vol. 120, pp. 3166–3175, 1998.

[6] S. L. Seager, *Organic and Biochemistry for Today*. Boston: Cengage Learning Inc, 2010.

[7] A. Bruce, A. Johnson, J. Lewis, M. Raff, K. Roberts, and P. Walters, *The Shape and Structure of Proteins. Molecular Biology of the Cell.Fourth Edition*. New York and London: Garland Science, 2002.

[8] H. Frauenfelder, G. Chen, J. Berendzen, P. W. Fenimore, H. Jansson, B. H. McMahon, I. R. Stroe, J. Swenson, and R. D. A. Young, “Unified model of protein dynamics proc,” *Natl. Acad. Sci.USA*, vol. 106, pp. 5129–5134, 2009.

[9] D. Nerukh and S. Karabasov, “Water-peptide dynamics during conformational transitions,” *The Journal of Physical Chemistry Letters*, vol. 4 (5), pp. 815–819, 2013.

[10] C. J. Cramer and D. G. Truhlar, “Implicit solvation models: Equilibria, structure, spectra, and dynamics,” *Chem. Rev.*, vol. 99, p. 2161−2200, 1999.

[11] G. Morra, *Role of electrostatics explored with molecular dynamics simulations for protein stability and folding*. PhD thesis, Freien Universitat Berlin, 2005.

[12] The CHARMM Development Project, “Charmm,” 2014.

[13] Peter Kollman’s group, “Amber,” 2014.

[14] O. Zikanov, *Essential Computational Fluid Dynamics*. New York: John Wiley, 2010.

[15] J. H. Irving and J. G. Kirkwood, “The statistical mechanical theory of transport processes iv. the equations of hydrodynamics,” *J.Chem.Phys*, vol. 18, p. 817, 1950.

[16] J. Brody, P. Yager, R. Goldstein, and R. H. Austin, “Biotechnology at low reynolds numbers,” *Biophys. J.*, vol. 71(6), p. 3430–3441, 1996.

[17] E.Shapiro, D. Drikakis, J. Gargiuli, and P. Vadgama, “Interface capturing in dual-flow microfluidics,” *Journal of Computational and Theoretical Nanoscience*, vol. 4, p. 1–5, 2007.

[18] G. Greenstein and A. Zajonc, *The Quantum Challenge: Modern Research on the Foundations of Quantum Mechanics, Second edition*. Sudbury: Jones and Bartlett Publishers, 2006.

[19] J. Kevorkian and J. Cole, *Perturbation Methods in Applied Mathematics*. London: Springer-Verlag, 2004.

[20] E. Weinan, *Principles of Multiscale Modelling*. Cambridge: Cambridge University Press, 2011.

[21] E. Buckingham, “On physically similar systems; illustrations of the use of dimensional equations,” *Physical Review*, vol. 4, pp. 345–376, 1914.

[22] G. I. Barenblatt, *Scaling, Self-Similarity, and Intermediate Asymptotics*. Cambridge: Cambridge University Press, 1996.

[23] K. Morton and D. Mayers, *Numerical Solution of Partial Differential Equations, An Introduction*. New York: Cambridge University Press, 2005.

[24] M.Ainsworth and T. Oden, *A Posteriori Error Estimation in Finite Element Analysis*. New York: John Wiley, 2000.

[25] M. P. Allen and D. J. Tildesley, *Computer Simulation of Liquids*. USA: Oxford University Press, 2000.

[26] W. Briggs, V. Henson, and S. McCormick, *A Multigrid Tutorial, 2nd ed.* SIAM, 2000.

[27] W. Press, S. Teukolsky, W. Vetterling, and B. Flannery, *Numerical Recipes: The Art of Scientific Computing .3rd ed.* New York: Cambridge University Press, 2007.

[28] A. Toselli and O. Wildlund, *Domain Decomposition Methods.* London: Springer-Verlag, 1981.

[29] P. J. Hoogerbrugge and J. M. V. A. Koelman, "Simulating microscopic hydrodynamic phenomena with dissipative particle dynamics," *Europhysics Letters*, vol. 19(3), p. 155–160, 1992.

[30] P. Espanol, "Dissipative particle dynamics with energy conservation," *Europhysics Letter*, vol. 40, p. 631, 1997.

[31] H. Wu, J. Xu, S. Zhang, and H. Wen, "Gpu accelerated dissipative particle dynamics with parallel cell-list updating," *IEIT Journal of Adaptive and Dynamic Computing*, vol. 1, pp. 33–42, 2011.

[32] S. O'Connell and P. Thompson, "Molecular dynamics-continuum hybrid computations: a tool for studying complex fluid flows," *Phys Rev E*, vol. 52, p. 5792, 1995.

[33] N.Hadjiconstantinou, "Discussion of recent developments in hybrid atomistic continuum methods for multiscale hydrodynamics," *Bull Polish Acad Sci: Tech Sci*, vol. 53, pp. 335–342, 2005.

[34] K. G. Fedosov D.A., "Triple-decker: interfacing atomistic-mesocopic-continuum flow regimes," *J. Comp.Phys*, p. 1157–1171, 2009.

[35] B. I. Schwartzentruber T.E., "A hybrid particle-continuum method applied to shock waves," *J. Comp.Phys*, vol. 215, pp. 402–416, 2006.

[36] K. P. Kotsalis E., Walther J., "Control of density fluctuations in atomistic-continuum simulations of dense liquids," *Physical Review E*, vol. 76, pp. 016709–1–7, 2007.

[37] K. P. Kotsalis E Walther J., Kaxiras E., "Control algorithm for multiscale flow simulations of water," *Physical Review E*, vol. 79, 2009.

[38] G. D. Fabritiis, R. Delgado-Buscalioni, and P. V. Coveney, "Multiscale modelling of liquids with molecular specificity," *Phys. Rev. Lett.*, vol. 97, p. 134501, 2006.

[39] X. B. Nie, S. Y. Chen, W. N. E, and M. O. Robbins, "A continuum and molecular dynamics hybrid method for micro- and nano-fluid flow," *J. Fluid Mech.*, vol. 500, pp. 55–64, 2004.

[40] E. G. Flekkoy, G. Wagner, and J. Feder, "Hybrid model for combined particle and continuum dynamics," *Europhys. Lett.*, vol. 52, p. 271–276, 2000.

[41] S. Mikhlin, *On the Schwarz algorithm (in Russian).* Moscow: Doklady Akademii Nauk SSSR, 1951.

[42] A. Asproulis, M. Kalweit, and D. Drikakis, "A hybrid molecular continuum method using point wise coupling," *Advances in Engineering Software*, vol. 46, p. 85–92, 2012.

[43] R. Steijl and G. Barakos, "Coupled navier–stokes /molecular dynamics simulations in nonperiodic domains based on particle forcing," *Int. J. Numer. Meth. Fluids*, vol. 69, p. 1326–1349, 2012.

[44] B. M. J., S. Keten, and T. Ackbarow, "Theoretical and computational hierarchical nanomechanics of protein materials: Deformation and fracture.," *Progress in Materials Science*, vol. 54, pp. 1101–1241, 2008.

[45] F. de Meyer, Venturoli, and B.Smit, "Molecular simulations of lipid-mediated protein-protein interactions," *Biophy. J.*, vol. 95, pp. 1851–1865, 2008.

[46] H. Frauenfelder, G. Chen, J. Berendzen, P. Fenimore, H. Jansson, B. McMahon, I. Stroe, J. Swenson, and R.D.Young, "A unified model of protein dynamics," *Proc. Natl. Acad. Sci. USA*, vol. 106, pp. 5129–5134, 2009.

[47] A. Markesteijn, S. Karabasov, A. Scukins, D. Nerukh, V. Glotov, and V. Goloviznin, "Concurrent multiscale modelling of atomistic and hydrodynamic processes in liquids," *Philosophical Transactions of the Royal Society*, vol. A 372, p. 20130379, 2014.

[48] A. Markesteijn and S. Karabasov, "Time asynchronous relative dimension in space method for multi-scale problems in fluid dynamics," *Journal of Computational Physics*, vol. 258, no. 10, pp. 137–164, 2014.

[49] D. Nerukh, "Non -markov state model of peptide dynamics," *Journal of Molecular Liquids*, vol. 176, pp. 65–70, 2012.

[50] A. B. Naim, "Statistical mechanics of "waterlike" particles in two dimensions. i. physical model and application of the percus–yevick equation," *J. Chem. Phys*, vol. 54, p. 3682, 1971.

[51] H. J. C. Berendsen, J. R. Grigera, and T. P. Straatsma, "The missing term in effective pair potentials," *J. Phys. Chem*, vol. 91(24), p. 6269–6271, 1987.

[52] Royal Institute of Technology and Uppsala University, "Gromacs," 2014.

[53] D. Drew and S.L.Passman, *Theory of Multicomponent Fluids*. New York: Springers, 1999.

[54] J. Anderson, E. Dick, G. Degrez, R. Grundmann, J. Degroote, and J. Vierendeels, *Computational Fluid Dynamics*. Berlin: Springer, 2009.

[55] G. D. Fabritiis, M. Serrano, R. Delgado-Buscalioni, and P. Coveney, "Fluctuating hydrodynamic modeling of fluids at the nanoscale," *Physical Review E*, vol. 75, p. 026307, 2007.

[56] T. Darden, D. York, and L. Pedersen, "Particle mesh ewald: An n log(n) method for ewald sums in large systems," *J. Chem. Phys.*, vol. 98, p. 10089, 1993.

[57] C. Vega, C. McBride, E. Sanz, and J. L. Abascal, "Radial distribution functions and densities for the spc /e, tip4p and tip5p models for liquid water and ices ih, ic, ii, iii, iv, v,vi, vii, viii, ix, xi and xii," *Physical Chemistry Chemical Physics*, vol. 7, pp. 1450–1456, 2005.

[58] T. Hynninen, C. Dias, A. Mkrtchyand, V. Heinonen, M. Karttunen, A. Fostera, and T. Ala-Nissila., "A molecular dynamics implementation of the 3d mercedes-benz water model.," *Computer Physics Communication*, 2011.

[59] D. C. Rapaport, *The Art of Molecular Dynamics Simulation .Second Edition*. Cambridge: Cambridge University Press, 2004.

[60] J. W. Gibbs, *Elementary Principles in Statistical Mechanics*. New York: Charles Scribner's Sons, 1902.

[61] L. Landau and E. Lifshitz, *Fluid Mechanics*. Pergamon press, 1966.

[62] U. M. B. Marconi, A. Puglisi, L. Rondon, and A. Vulpiani, "Fluctuation-dissipation: Response theory in statistical physics," *Physics Reports*, vol. 461 (4–6), p. 111–195, 2008.

[63] M. L. Mehta, *Random Matrices, 3rd ed.* New York: Academic Press, 1991.

[64] A. Markesteijn, S. Karabasov, V. Glotov, and V. Goloviznin, "A new non-linear two-time-level central leapfrog scheme in staggered conservation-flux variables for fluctuating hydrodynamics equations with gpu implementation," *Computer Methods in Applied Mechanics and Engineering*, vol. under revision, 2014.

[65] V. Glotov, V. Goloviznin, S. Karabasov, and A. Markesteijn, "New two level leapfrog scheme for modeling the stochastic landau–lifshitz equations," *Computational Mathematics and Mathematical Physics*, vol. 54 (2), p. 315–334, 2014.

[66] R. B. Stewart and R. T. Jacobsen, "Thermodynamic properties of argon from the triple point to 1200k with pressure to 1000 mpa," *Center of Applied Thermodynamic Studies*, 1988.

[67] Y. Kataoka, "Studies of liquid water by computer simulations. iii. dynamical properties of a 2d model," *Bull. Chem. Soc. Jpn*, vol. 57, pp. 1522–1527, 1983.

[68] Y. Kataoka, "A molecular dynamical study of the mutual diffusion coefficient and cooperative motion in a 2-dimensional aquaeous solution," *Bull. Chem. Soc. Jpn*, vol. 59, pp. 3341–3346, 1985.

[69] K. Okazaki, S. Nosé, Y. Kataoka, and T. Yamamoto, "Study of liquid water by computer simulations. i. static properties of a 2d model," *The Journal of Chemical Physics*, vol. 75, no. 12, pp. 5864–5874, 1981.

[70] F. Hirata and P. J. Rossky, "A realization of 'v structure' in liquid water," *J. Chem. Phys*, vol. 74, pp. 6867–6874, 1981.

[71] C. L. Dias, T. Ala-Nissala, M. Karttunen, I. Vattulainen, and M. Grant, "Microscopic mechanism for cold denaturation," *Physical Review Letters*, vol. 100, p. 118101, 2008.

[72] C. L. Dias, "Using microscopic mechanism for pressure and cold denaturations of proteins," *Physical Review Letters*, vol. 109, p. 048104, 2012.

[73] T. Urbič, V. Vlachy, Y. V. Kalyuzhnyi, N. T. Southall, and K. A. Dill, "A two-dimensional model of water: Solvation of nonpolar solutes," *The Journal of Chemical Physics*, vol. 116, p. 723, 2002.

[74] T. Urbič, V. Vlachy, Y. V. Kalyuzhnyi, and K. A. Dill, "Orientation-dependent integral equation theory for a two-dimensional model of water," *The Journal of Chemical Physics*, vol. 118, p. 5516, 2003.

[75] T. Urbič, V. Vlachy, Y. V. Kalyuzhnyi, and K. A. Dill, "Theory for the solvation of nonpolar solutes in water," *The Journal of Chemical Physics*, vol. 127, p. 174505, 2007.

[76] T. Urbič, V. Vlachy, Y. V. Kalyuzhnyi, and K. A. Dill, "An improved thermodynamic perturbation theory for mercedes-benz water," *The Journal of Chemical Physics*, vol. 127, p. 174511, 2007.

[77] T. Urbič and M. F. Holovkol, "Mercedes–benz water molecules near hydrophobic wall: Integral equation theories vs monte carlo simulations," *The Journal of Chemical Physics*, vol. 135, p. 134706, 2011.

[78] E. M. Pearson, "Laplace-transform technique for deriving thermodynamic equations from the classical microcanonical ensemble," *Phys. Rev. A*, vol. 32, pp. 3030–3039, 1985.

[79] G. A. Korn and T. M. Korn, *Mathematical Handbook for Scientists and Engineers*. Oxford: Courier Dover Publications, 2000.

[80] P. Mark and L. Nilsson, "Structure and dynamics of the tip3p, spc, and spc /e water models at 298 k," *J. Phys. Chem. A*, vol. 105 (43), p. 9954–9960, 2001.

[81] A. B. Naim, *Molecular Theory of Water and Aqueous Solutions*. Singapore: World Scientific, 2010.

[82] A. Thomas and A. Elcock, "Molecular simulations suggest protein salt bridges are uniquely suited to life at high temperatures," *J. Am. Chem. Soc*, vol. 126, pp. 2208–2214, 2004.

[83] S. McGuffee and A. Elcock, "Diffusion, crowding and protein stability in a dynamic molecular model of the bacterial cytoplasm.," *PLoS Comput. Biol.*, vol. 6, p. e1000694, 2010.

[84] E. Pavlov, M. Taiji, A. Scukins, A. Markesteijn, S. Karabasov, and D. Nerukh, "Visualising and controlling the flows in biomolecular systems at and between multiple scales: from atoms to hydrodynamics at different locations in time and space," *Royal Society of Chemistry*, vol. DOI:10.1039/C3FD00159H, 2014.

[85] P. Kumar, G. Franzese, S. Buldyrev, and E. Stanley, "Molecular dynamics study of orientational cooperativity in water," *Phys. Rev. E*, vol. 73, p. 041505, 2006.

[86] K. Umezawa, R. Morikawa, H. Nakamura, and J. Higo, "Solvent flow patterns fluctuating largely around a protein and correlation with solvent density fluctuations: a molecular dynamics study," *J. Chem. Phys*, vol. 132, p. 155103, 2010.

[87] The Open MPI Project, "Open mpi," 2014.

[88] The Research Collaboratory for Structural Bioinformatics, "Rscb protein data bank," 2014.

5

Supplementary files

Four video files are available (provided by Dr Ivan Korotkin) on the CD attached to the thesis. Each file demonstrates the effect of the coupling (investigated in this work) on the different systems (3D liquid argon and dialanine in SPC/E water). These video files (`.mpg` format) can be played using Windows Media Player.

5.1 Simulation of three-dimensional liquid argon with the variable coupling parameter s profile

Demonstration of three-dimensional liquid argon simulation using the coupling method when sphere type profile of the coupling parameter s is used (CD: file name '5.1.Dr.I.Korotkin. 3D liquid argon (sphere profile s).mpg').

5.2 Simulation of dialanine with 1444 SPC/E water molecules when the variable coupling parameter s profile is fixed to the simulation domain center

Demonstration of dialanine with 1444 SPC/E water molecules simulation when sphere type profile of the coupling parameter s is fixed in the center of the simulation domain (CD: file name ‘5.2.Dr.I.Korotkin. dialanine and 1444 SPCE water (fixed sphere type s).mpg’).

5.3 Simulation of dialanine with 30000 SPC/E water molecules when the variable coupling parameter s profile is fixed to the simulation domain center

Demonstration of dialanine with 30000 SPC/E water molecules simulation when sphere type profile of the coupling parameter s is fixed in the center of the simulation domain (CD: file name ‘5.3.Dr.I.Korotkin. dialanine and 30000 SPCE water (fixed sphere type s).mpg’).

5.4 Simulation of dialanine with 30000 SPC/E water molecules when the variable coupling parameter s profile is moving with the peptide’s geometrical center

Demonstration of dialanine with 30000 SPC/E water molecules simulation when sphere type profile of the coupling parameter s is linked to the dialanine’s geometrical center (CD: file name ‘5.4.Dr.I.Korotkin. dialanine and 30000 SPCE water (moving sphere type s).mpg’).

List of Publications

1. Anton Markesteijn, Sergey Karabasov, Arturs Scukins, Dmitry Nerukh, Vyacheslav Glotov and Vasily Goloviznin. Concurrent multiscale modelling of atomistic and hydrodynamic processes in liquids. 2014. Philosophical Transactions of the Royal Society. A 372. 20130379.
2. Evgen Pavlov, Makoto Taiji, Arturs Scukins, Anton Markesteijn, Sergey Karabasov and Dmitry Nerukh. Visualising and controlling the flows in biomolecular systems at and between multiple scales: from atoms to hydrodynamics at different locations in time and space. 2014. Royal Society of Chemistry. DOI:10.1039/C3FD00159H.
3. Arturs Scukins, Vitaliy Bardik, Evgen Pavlov and Dmitry Nerukh. Molecular Dynamics implementation of BN2D or 'Mercedes Benz' water model. **submitted**.
4. Arturs Scukins, Vitaliy Bardik, Evgen Pavlov and Dmitry Nerukh. Structure and collective dynamics of two dimensional water I: Molecular Dynamics implementation of Mercedes Benz model. **submitted**.
5. Arturs Scukins, Dmitry Nerukh, Evgen Pavlov, Sergey Karabasov and Anton Markesteijn. Structure and collective dynamics of two dimensional water II: multiscale Molecular Dynamics / Hydrodynamics implementation of Mercedes Benz model. **submitted**.

Conferences

1. Dmitry Nerukh, Sergey Karabasov, Arturs Scukins, Evgen Pavlov, Ivan Korotkin, Vladimir Farafonov, and Makoto Taiji, Hybrid molecular dynamics–hydrodynamics approach for multiscale modelling of liquid molecular systems, 10th Congress of the World Association of Theoretical and Computational Chemists (WATOC 2014) (Santiago, Chile, 2014)

2. Dmitry Nerukh, Sergey Karabasov, Arturs Scukins, Evgen Pavlov, Ivan Korotkin, Vladimir Farafonov, and Makoto Taiji, Hybrid molecular dynamics–hydrodynamics framework for modelling liquid molecular systems, EMLG - JMLG annual meeting 2014 (Rome, Italy, 2014)

3. Dmitry Nerukh, Arturs Scukins, Evgen Pavlov, Sergey Karabasov, Anton Markesteijn, Hybrid molecular dynamics - hydrodynamics framework for modelling liquids, Liquids 2014 (Lisbon, Portugal, 2014)

4. Evgen Pavlov, Makoto Taiji, Arturs Scukins, Ivan Korotkin, Anton Markesteijn, Sergey Karabasov, Dmitry Nerukh, Visualising and controlling the flows in biomolecular systems at and between multiple scales: from atoms to hydrodynamics at different locations in time and space, Faraday Discussion 169: Molecular Simulations and Visualization (Nottingham, UK, 2014)

5. Sergey Karabasov, Dmitry Nerukh, Arturs Scukins, Evgen Pavlov, Anton Markesteijn, Pardis Tabaee, Makoto Taiji, Modelling solutions of biomolecules at atomistic and continuum representation at the same time: hybrid MD/hydrodynamics framework, CCPBioSim / CCP5 Multiscale Modelling Conference (Manchester, UK, 2014)

6. Dmitry Nerukh, Arturs Scukins, Evgen Pavlov, Sergey Karabasov, Anton Markesteijn, and Vitaliy Bardik, Modelling liquid solutions at atomistic and continuum representation at the same time: hybrid MD/hydrodynamics implementation of two dimensional water model, Methods and Applications of Computational Chemistry (Kharkov, Ukraine, 2013)

7. Dmitry Nerukh, Arturs Scukins, Evgen Pavlov, Vladimir Ryabov, Sergey Karabasov, and

Anton Markesteijn, Molecular dynamics/hydrodynamics hybrid description of liquids and biomolecular solutions, EMLG - JMLG annual meeting 2013 (Lille, France, 2013)

A Appendix

A.1 Relaxation method

The relaxation method is an iterative method for solving systems of equations.

Using finite differences framework, initial partial differential equation can be discretized in the following manner

$$u^{n+1} = Bu^n + g, \tag{A.1}$$

where u is the solution, $n+1$ is the next time layer, B is the iteration matrix and g is the constant vector.

For this case, the relaxation method can be expressed as

$$u^{n+1} = (1-\omega)u^n + \omega(Bu^n + g), \tag{A.2}$$

where ω is a parameter that minimizes spectral radius of the relaxed iteration matrix, which is given by $B_\omega = (1-\omega)I + \omega B$.

More detailed description on the relaxation methods can be found in [27].

A.2 Method of characteristics ('one way' coupling case)

The Landau Lifshitz-Fluctuating Hydrodynamics (LL-FH) equations can be expressed in the characteristic form

$$\frac{\partial\phi}{\partial t}+A\frac{\partial\phi}{\partial x}=f(\phi), \tag{A.3}$$

where $\phi=(\rho,u,P)$ are the conservative variables and $f(\phi)$ denotes the right hand side. The matrix A is given by

$$A=\begin{pmatrix} u & \rho & 0 \\ 0 & u & 1/\rho \\ 0 & \rho c^2 & u \end{pmatrix}$$

.

Thereby, the LL-FH equations can be rewritten in the terms of eigenvalues and eigenvectors.

Following eigenvalues of the matrix A are obtained $\lambda_1=u+c$, $\lambda_2=u-c$, $\lambda_3=u$, where c is the speed of sound.

Consequently, the eigenvectors are given by $\vec{v}_1=(0,1,\frac{1}{\rho c})$, $\vec{v}_2=(0,1,-\frac{1}{\rho c})$ and $\vec{v}_3=(-c^2,0,1)$.

The eigenvector matrix is expressed as

$$\Omega=\begin{pmatrix} 0 & 1 & \frac{1}{\rho c} \\ 0 & 1 & -\frac{1}{\rho c} \\ -c^2 & 0 & 1 \end{pmatrix}$$

.

Now, the LL-FH equations are multiplied with the eigenvector matrix Ω derived above

$$\Omega\frac{\partial\phi}{\partial t}+\Omega A\frac{\partial\phi}{\partial x}=\Omega f(\phi). \tag{A.4}$$

According to the well known relationship $A\Omega=\Lambda\Omega$ equation above becomes

$$\Omega\frac{\partial\phi}{\partial t}+\Lambda\Omega\frac{\partial\phi}{\partial x}=\Omega f(\phi), \tag{A.5}$$

where the eigenvalue matrix is given by

$$\Lambda=\begin{pmatrix} u+c & 0 & 0 \\ 0 & u-c & 0 \\ 0 & 0 & u \end{pmatrix}$$

.

Using principles above, the LL-FH equations can be written explicitly

$$\begin{gathered}\left[\frac{\partial u}{\partial t}+\frac{1}{\rho c}\frac{\partial P}{\partial t}\right]+(u+c)\left[\frac{\partial u}{\partial x}+\frac{1}{\rho c}\frac{\partial P}{\partial x}\right]=F_1 \\ \left[\frac{\partial u}{\partial t}-\frac{1}{\rho c}\frac{\partial P}{\partial t}\right]+(u-c)\left[\frac{\partial u}{\partial x}-\frac{1}{\rho c}\frac{\partial P}{\partial x}\right]=F_2 \\ \left[\frac{\partial P}{\partial t}-c^2\frac{\partial\rho}{\partial t}\right]+u\left[\frac{\partial P}{\partial x}-c^2\frac{\partial\rho}{\partial x}\right]=F_3.\end{gathered} \tag{A.6}$$

Riemann invariants R, Q, S can be introduced, such that (A.6) is reduced to

$$\begin{aligned}\frac{\partial R}{\partial t} + (u+c)\frac{\partial R}{\partial x} &= F_1 \\ \frac{\partial Q}{\partial t} + (u-c)\frac{\partial Q}{\partial x} &= F_2 \\ \frac{\partial S}{\partial t} + u\frac{\partial S}{\partial x} &= F_3.\end{aligned} \tag{A.7}$$

These Riemann invariants can be associated with the two pressure waves and one entropy wave. Before the Riemann invariants are determined following relationship must be noted $c = c(\rho) = \sqrt{\frac{\partial P}{\partial \rho}}$, which can be reordered as $\partial P = c^2 \partial \rho$.

Using relationship above invariants can be extracted assuming that

$$\left[\frac{\partial u}{\partial t} + \frac{1}{\rho c}\frac{\partial P}{\partial t}\right] = \left[\frac{\partial u}{\partial t} + \frac{c}{\rho}\frac{\partial \rho}{\partial t}\right] = \left[\frac{\partial u}{\partial t} + c\frac{\partial \ln \rho}{\partial t}\right], \tag{A.8}$$

thus $R = u + c\ln\rho$, $Q = u - c\ln\rho$.

The last equation of the LL-FH is not solved in this work, since adiabatic system is studied, where energy equation is decoupled from the mass and momentum conservation equations.

Generally speaking, S is an entropy if the ideal gas is studied. A well known relationship for ideal gas

$$c^2 = \frac{\gamma p}{\rho} \tag{A.9}$$

provides with the following derivations $\partial\rho \cdot \frac{1}{\rho} - \partial P \cdot \frac{\rho}{\gamma P} \cdot \frac{1}{\rho} = \partial \ln\rho - \partial \ln P^{1/\gamma} = \frac{1}{\gamma}\partial\left(\frac{\rho^\gamma}{P}\right)$ leading to the entropy for the ideal gas, that must be constant and equal to $S = \frac{\rho^\gamma}{P}$.

A.3 Method of characteristics ('two way' coupling case)

The so called 'two way' coupling governing equations of the FH phase are summarized here.

It is advisable to introduce following variables

$$\rho' = \tilde{\rho} - \sum_p \rho_p, \tag{A.10}$$

$$u'\rho' = \tilde{u}_j\tilde{\rho} - \sum_p \rho_p u_{jp}, \tag{A.11}$$

where the first definition, that is density difference between the mixture and MD phase densities, can be regarded as the perturbation density. The second definition, which is the difference between the mixture and MD phase momentum can be regarded as the perturbation momentum.

Following the definitions above, the LL-FH mass conservation equation can be expressed as

$$\frac{\partial}{\partial t}\rho' + \frac{\partial}{\partial x_i}\tilde{u}_i\rho' = Q_\rho, \tag{A.12}$$

where

$$Q_\rho = \frac{\partial}{\partial x_i}\left[s\left(1-s\right)\alpha\frac{\partial}{\partial x_i}\left(\rho'\right)\right] \tag{A.13}$$

followed by the LL-FH momentum conservation equation

$$\frac{\partial}{\partial t}u'_j\rho' + \frac{\partial}{\partial x_i}\tilde{u}_i u'_j\rho' = sF_j + Q_u, \tag{A.14}$$

where

$$Q_u = \frac{\partial}{\partial x_j}\left[s\left(1-s\right)\beta\frac{\partial}{\partial x_j}\left(u'_j\rho'\right)\right]. \tag{A.15}$$

The FH phase force per volume term F_j is defined in the same manner as in the standard LL-FH simulation

$$F_j = \frac{\partial}{\partial x_j}\left(\Pi_{ij} + \tilde{\Pi}_{ij}\right), \tag{A.16}$$

where the dissipative stress tensor is defined as

$$\Pi_{ij} = -\left(p - \xi\frac{\partial u_j}{\partial x_j}\right)\delta_{ij} + \eta\left(\frac{\partial u_j}{\partial x_i} + \frac{\partial u_i}{\partial x_j} - 2D^{-1}\frac{\partial u_j}{\partial x_j}\cdot\delta_{ij}\right), \tag{A.17}$$

with ξ and η are the shear and bulk viscosities, D is the dimension of the system, p is the pressure and δ_{ij} is the Kronecker delta function.

In order to estimate the stochastic stress tensor fluctuation-dissipation theorem (FDT) [62] is used, which predicts the behaviour of non-equilibrium thermodynamical systems.

The theorem provides the balance between the fluctuations in the system and its dissipative properties. If the balance is violated then system's behaviour can be either dominated by the fluctuations or become too dissipative. In the first case we get instabilities, while in the second case very small fluctuations. Thus it is important to maintain the balance between these two properties.

The FDT provides us with the covariance of stochastic stress tensor

$$\langle\tilde{\Pi}_{ij}(r,t)\cdot\tilde{\Pi}_{kl}(r',t')\rangle = 2k_BT\left[\eta\left(\delta_{ik}\delta_{jl} + \delta_{il}\delta_{jk}\right) + \left(\xi - \frac{2}{3}\eta\right)\delta_{ij}\delta_{kl}\right] \tag{A.18}$$
$$\times\delta(r-r')\delta(t-t')$$

that yields stochastic stress [61] expressed as

$$\tilde{\Pi}_{ij} = \sqrt{\frac{2k_BT}{\delta t\delta V}}\left(\sqrt{2}\sqrt{\eta}\cdot\mathbf{G}^s_{ij} + \sqrt{D}\sqrt{\xi}\frac{tr[\mathbf{G}]}{D}\mathbf{E}_{ij}\right), \tag{A.19}$$

where $\mathbf{G}$ is Gaussian random matrix, $\mathbf{G}^s_{ij} = \frac{\mathbf{G}_{ij}+\mathbf{G}^T_{ij}}{2} - \frac{tr[\mathbf{G}]}{D}\mathbf{E}_{ij}$, $\mathbf{E}$ is the unity matrix and $tr[\mathbf{G}] = G_{11} + G_{22} + G_{33}$, which stands for the matrix trace, k_B is Boltzmann constant, T is the temperature. The Gaussian random matrix $\mathbf{G}$ is a matrix which elements are randomly generated with the Gaussian distribution [63].

The set of equations (A.12) - (A.15) is solved numerically using a second-order centred finite-difference scheme based on the characteristic decomposition method. For the 'two way' coupling governing equations (A.12) and (A.15) can be expressed in the matrix format (for simplicity one-dimensional case is considered here)

$$U_t + AU_x = Q, \tag{A.20}$$

where variables are expressed as

$$U = \begin{pmatrix} \rho' \\ \rho' u'_j \end{pmatrix}$$

the derivative with respect to time

$$U_t = \begin{pmatrix} \frac{\partial \rho'}{\partial t} \\ \\ \frac{\partial \rho' u'_j}{\partial t} \end{pmatrix}$$

followed by the spatial derivative

$$U_x = \begin{pmatrix} \frac{\partial \rho'}{\partial x_i} \\ \\ \frac{\partial \rho' u'_j}{\partial x_i} \end{pmatrix}$$

We apply operator splitting technique, thus the right hand side temporally is assumed to be $Q = 0$.

The matrix $\mathbf{A}$ is given by

$$A = \begin{pmatrix} \tilde{u}_j & 0 \\ 0 & \tilde{u}_j \end{pmatrix}$$

, that leads to the characteristic speeds $\lambda_{1,2} = \tilde{u}$ and Riemann invariants are ρ' and $\rho' u'_j$.

Finally, the right hand side Q is used when the conservative values are evaluated.

A.4 Ergodicity

Assuming, that studied N - body system obey ergodic hypothesis, MD simulations can be used to determine macroscopic thermodynamic properties of the system.

The ergodicity theorem states that the time average is the same as an ensemble average (denoted as $\langle\rangle$), where the ensemble is an idealization consisting of a large number of virtual copies of the system considered simultaneously, each of which represents a possible state of the real system could be in [4, 59].

A.5 Thermodynamics of BN2D water model in the NVE ensemble

The relationships between the thermodynamic variables and macroscopic parameters, such as temperature T, pressure P, isochoric heat capacity C_V, isothermal compressibility β_T, thermal expansion coefficient α_P are given by:

$$T = \left(\frac{\partial S}{\partial E}\right)_V^{-1}, \tag{A.21}$$

$$P = T\left(\frac{\partial S}{\partial V}\right)_E, \tag{A.22}$$

$$C_V = \left[\left(\frac{\partial T}{\partial E}\right)_V\right]^{-1}, \tag{A.23}$$

$$\frac{1}{\beta_T} = -V\left(\frac{\partial P}{\partial V}\right)_T = -V\left[\left(\frac{\partial P}{\partial V}\right)_S + \frac{T}{C_V}\left(\frac{\partial P}{\partial T}\right)_V^2\right], \tag{A.24}$$

$$\alpha_P = \frac{1}{V}\left(\frac{\partial V}{\partial T}\right)_P = \beta_S\left(\frac{dP}{dT}\right)_V. \tag{A.25}$$

In order to evaluate these thermodynamic properties from molecular dynamics results statistical mechanics should be used. The MD theory framework naturally leads to the NVE ensemble. The phase space volume [78, 4] is defined as

$$\Omega(N,V,E) = M\int dp^N \ldots dq^N \delta(E - H(p^N,q^N)) \tag{A.26}$$

and the phase space density as

$$\Sigma(N,V,E) = M\int dp^N \ldots dq^N \Theta(E - H(p^N,q^N)), \tag{A.27}$$

where p and q are the phase space momenta and coordinates, N is the number of particles, V is the volume of the system, E is the total energy, $H(q^N,p^N)$ is the Hamiltonian, M is the normalization constant, and Θ is the Heaviside step function [79].

A useful relationship between the phase space volume and density is available[78]

$$\Omega(N,V,E) = \frac{\partial}{\partial E}\Sigma(N,V,E). \tag{A.28}$$

In the context of statistical mechanics, for a large number of molecules the entropy can be defined as [78]

$$S = k_B \; ln\Sigma. \tag{A.29}$$

It is assumed that system's Hamiltonian can be separated into the potential and the kinetic energies [4]

$$H(q^N, p^N) = \Phi(q^N) + K(p^N). \tag{A.30}$$

Thus the Laplace transform applied to the microcanonical ensemble (NVE) partition function or phase space volume (A.26) results in following expression

$$\begin{aligned} L[\Omega] &= M \int dp^N \int dq^N \int dE \; e^{-\beta E} \delta(E - \Phi(q^N) - K(p^N)) \\ &= M \int dq^N \; e^{-\beta\Phi(q^N)} \int dp^N \; e^{-\beta K(p^N)}, \end{aligned} \tag{A.31}$$

with

$$M = \frac{E_0}{N! h^{3N}}, \tag{A.32}$$

where h is Plank constant, E_0 is the thickness of the energy shell [4].

When BN2D water model is studied, the kinetic energy has three components (K_x, K_y, K_ϕ). The two transitional kinetic energies are

$$K_x(p_x) = \frac{p_x^2}{2m}, \tag{A.33}$$

$$K_y(p_y) = \frac{p_y^2}{2m}, \tag{A.34}$$

and the rotational kinetic energy is

$$K_\phi(p_\omega) = \frac{p_\omega^2}{2I}, \tag{A.35}$$

where p_x, p_y are the momentum along x and y respectively, p_ω is the rotational velocity.

Following substitution is performed $p'^2_{x,y} = \frac{p_i^2}{2m}$, $p_i = p'_i\sqrt{2m}$ and $dp_i = dp'_i\sqrt{2m}$, where i denotes spatial coordinate x and y. Note, that in (A.31) $dp^N = dp_x^1 \, dp_x^2 ... dp_x^N ... dp_y^1 \, dp_y^2 ... dp_y^N$, where N is the number of particles. While for the rotational part $dp_\omega = dp'_\omega\sqrt{2I}$. Since the parts of the integral are independent, they can be solved separately assuming that

$$\int dp^N \; e^{-\beta K(p^N)} = (2m\pi)^{2N/2}(2I\pi)^{N/2}\beta^{-3N/2}, \tag{A.36}$$

since

$$\int dp'\, e^{-\beta p'^2} = \sqrt{\frac{\pi}{\beta}}. \tag{A.37}$$

Now, Laplace transform applied to the phase space volume can be rewritten as

$$L[\Omega] = M \int dq^N\, e^{-\beta\Phi(q^N)}\, (2m\pi)^N (2I\pi)^{N/2} \beta^{-3N/2} = M\, (2m\pi)^N (2I\pi)^{N/2} \int dq^N\, e^{-\beta\Phi(q^N)}\, \beta^{-3N/2}. \tag{A.38}$$

Applying the inverse Laplace transform to the integral above

$$L^{-1}\left(\int dq^N\, e^{-\beta\Phi(q^N)} \beta^{-3N/2}\right) = \frac{1}{2\pi i}\int_{-i\infty}^{i\infty} dq^N \beta^{-3N/2} e^{\beta(E-\Phi(q^N))} d\beta \tag{A.39}$$

the phase space volume is obtained, where the kinetic part is eliminated form the integral

$$\Omega(N,V,E) = M\, (2m\pi)^N (2I\pi)^{N/2} \times \int dq^N \frac{(E-\Phi(q^N))^{3N/2-1}}{\Gamma(3N/2)} \Theta(E-\Phi(q^N)). \tag{A.40}$$

Using relationship between the phase space volume and density

$$\Omega(N,V,E) = \frac{\partial}{\partial E}\Sigma(N,V,E),$$

the phase space density is obtained

$$\Sigma(N,V,E) = M\, (2m\pi)^N (2I\pi)^{N/2} \times \int dq^N \frac{(E-\Phi(q^N))^{3N/2}}{\Gamma(3N/2+1)} \Theta(E-\Phi(q^N)). \tag{A.41}$$

Using the definition of the entropy (A.29) and thermodynamic relationships (A.21) - (A.24) the thermodynamic parameters can be calculated for the NVE ensemble using MD simulation.

A.5.1 Temperature

The temperature is defined as (A.21) yielding

$$k_B\, T = \frac{\Sigma}{\Omega} = \frac{2}{3N}\langle K \rangle, \tag{A.42}$$

where $\langle\rangle$ is the ensemble or time average, E is the total energy.

A.5.2 Pressure

Since the pressure is defined as (A.22) we get

$$P = \frac{1}{\Omega}\frac{\partial \Sigma}{\partial V}, \tag{A.43}$$

the volume V in the two-dimensional system is replaced with the area A.

The volume dependence is contained implicitly in the integration limits, thus by changing variables in the integral we render the limits independent of the box size.

Using the substitutions in the phase space

$$q = A^{\frac{1}{2}} q^* \tag{A.44}$$

and

$$p = A^{\frac{1}{2}} p^* \tag{A.45}$$

the phase space integrals become

$$\Sigma(N,V,E) = M_1 A^N \times \int dq^{*N} \frac{(E - \Phi((A^{1/2}q^*)^N))^{3N/2}}{\Gamma(3N/2+1)} \times \Theta(E - \Phi((A^{1/2}q^*)^N)) \tag{A.46}$$

and

$$\Omega(N,V,E) = M_1 A^N \times \int dq^{*N} \frac{(E - \Phi((A^{1/2}q^*)^N))^{3N/2-1}}{\Gamma(3N/2)} \times \Theta(E - \Phi((A^{1/2}q^*)^N), \tag{A.47}$$

where $M_1 = M \cdot (2m\pi)^N (2I\pi)^{N/2}$.

The phase space density derivative with respect to the area yields pressure

$$P = \frac{1}{\Omega}\frac{\partial \Sigma}{\partial A} = \frac{N}{A}\frac{2}{3N}\langle K \rangle - \left\langle \frac{\partial \Phi}{\partial A} \right\rangle = \rho\, k_B T - \left\langle \frac{\partial \Phi}{\partial A} \right\rangle, \tag{A.48}$$

where $\rho = N/A$ is the number density.

A.5.3 Isochoric heat capacity

The isochoric heat capacity (A.23) is calculated as

$$\frac{1}{C_V} = \frac{1}{k_B}\left(\frac{1}{\Omega}\frac{\partial \Sigma}{\partial E} - \frac{\Sigma}{\Omega^2}\frac{\partial \Omega}{\partial E}\right) = \frac{1}{k_B}\left(1 - \frac{\Sigma}{\Omega^2}\frac{\partial \Omega}{\partial E}\right), \tag{A.49}$$

which is reduced to

$$\frac{C_V}{Nk_B} = \left(\frac{2}{3}\langle K \rangle \left\langle K^{-1} \right\rangle + N(1 - \langle K \rangle \left\langle K^{-1} \right\rangle)\right)^{-1}. \tag{A.50}$$

A.5.4 Isothermal compressibility

The first term in the equation (A.24) for the isothermal compressibility is defined as

$$-A\left(\frac{\partial P}{\partial A}\right)_S = -A\left(\frac{\partial\left(\frac{1}{\Omega}\frac{\partial \Sigma}{\partial A}\right)}{\partial A}\right)_S = -A\left(\frac{1}{\Omega}\frac{\partial^2 \Sigma}{\partial A^2}\right)_S + A\left(\frac{1}{\Omega}\frac{\partial \Sigma}{\partial A}\frac{1}{\Omega}\frac{\partial \Omega}{\partial A}\right)_S, \tag{A.51}$$

which yields

$$\begin{aligned}\left(\frac{\partial P}{\partial A}\right)_S = \left(\frac{N(N-1)}{A^2}k_BT - \left\langle\frac{\partial^2\Phi}{\partial A^2}\right\rangle - -2\rho\left\langle\frac{\partial\Phi}{\partial A}\right\rangle + (3N/2-1)\left\langle K^{-1}\left(\frac{\partial\Phi}{\partial A}\right)^2\right\rangle\right) - \\ -\left(\rho-(3N/2-1)\left\langle K^{-1}\frac{\partial\Phi}{\partial A}\right\rangle\right)P.\end{aligned} \tag{A.52}$$

The technique from [78] was used for the systems with translational degrees of freedom only. This particular application to BN2D water model shows that the angular degree of freedom must be treated in the same manner as the translational degrees of freedom.

A.6 Equations of motion in the NPT ensemble

In the NPT ensemble virtual variables (q', p', s_t, V, t') are introduced. These variable can be related to the real variables (q, p, s_t, V, t) when scaling of time and coordinates is performed. Where $'$ denotes virtual variable, q is the coordinate, p is the impulse or momentum, V is the volume, t is time and s_t is the new variable which is discussed later.

Relationship between these variable can be established if following strategy is used: the time is scaled with the new variable s_t and the coordinates are scaled with the length, which is defined as $V^{1/d}$, where d stands for the dimensionality [4, 59]. In mathematical terms these relationships are expressed as

$$q_i = V^{1/d}q', \tag{A.53}$$

$$t = \int^t \frac{1}{s_t}\cdot dt'. \tag{A.54}$$

Eventually, the volume V and parameter s_t are assumed to be the new degrees of freedom. As a result, the change in the volume will maintain constant pressure in the system, and the change of s_t constant temperature, since MD particles velocities depend from the time rate.

Using relationships above and statistical mechanics framework, the real momentum is proportional to the virtual momentum and the proportionality coefficient is defined as

$$p = c\cdot p'. \tag{A.55}$$

The coefficient c is unknown, although it can be derived using classical mechanics concepts. Since momentum is a product of the mass m and velocity

$$p = m\cdot\frac{dq}{dt}, \tag{A.56}$$

where velocity is a derivative of the coordinate with respect to time.

Using relationships (A.53) and (A.54) momentum can be expressed in the terms of virtual variables

$$p = s_t V^{1/d} m \cdot \frac{dq'}{dt'}. \tag{A.57}$$

The full derivative is given by $\dot{q} = V^{1/d}\dot{q}' + (\frac{\dot{V}}{Vd}V^{1/d})q'$, the velocities must be measured relative to the rate at which the region size changes. Thus the flow component $\dot{V}$ must be dismissed from the atomic velocities, that is essential to ensure the correct definition of the temperature [59].

From the statistical mechanics perspective a relationship between the coordinates and momentum is given by

$$\frac{dq'}{dt'} = \frac{dH}{dp'}, \tag{A.58}$$

where H is system's Hamiltonian.

The Hamiltonian is a sum of kinetic and potential energy from all degrees of freedom. Therefore, according to the statistical mechanics principles full system Hamiltonian is expressed as

$$H = \sum_i \frac{p_i^2}{2m_i} + \sum_i \frac{p_{i\phi}^2}{2I} + \Phi(q,\phi) + \frac{p_{s_t}^2}{2M_s} + gkT\ln s_t + \frac{p_v^2}{2M_V} + P_{ex}V, \tag{A.59}$$

where p_{s_t} and p_v are conjugate momenta for s_t and V respectively, I is the moment of inertia, M_s and M_V are the proportionality coefficients (generalized masses), summation is done over all particles.

For the virtual time $g = d \cdot N + 1$, where N is the number of particles, and for the real time $g = d \cdot N$ [59, 25, 4].

Now, the derivative $\frac{dq'}{dt'}$ can be substituted in (A.57) considering the relationship between the real and virtual momentum

$$p = m \cdot s_t V^{1/d} \frac{d[c^2 p'^2/2m]}{dp'} \tag{A.60}$$

that can be reduced to

$$p = s_t V^{1/d} c[c \cdot p'] = s_t V^{1/d} cp. \tag{A.61}$$

Eliminating p from the both sides, proportionality parameter is given by

$$c = \frac{1}{s_t V^{1/d}}. \tag{A.62}$$

Thus the relationship between the momentum in terms of available parameters is

$$p_i = \frac{p_i'}{s_t V^{1/d}}. \tag{A.63}$$

Furthermore, an assumption is made, that the angle between the MB arms and x-axis is not scaled, since the angle in the MB model is separated from the spatial space. Thus, following transformation is true for the angular coordinate

$$\phi_i = \phi'_i. \tag{A.64}$$

Following similar procedure to the momentum above, a relationship between the real and virtual rotational momentum is

$$p_\phi = c_\phi \cdot p'_\phi, \tag{A.65}$$

where c_ϕ is the proportionality coefficient.

It is known, that rotational momentum is a product of the moment of inertia I and angular velocity

$$p_\phi = I \cdot \frac{d\phi}{dt} \tag{A.66}$$

that in terms of the virtual angle and time can be written as

$$p_\phi = s_t \cdot I \frac{d\phi'}{dt'}. \tag{A.67}$$

Using statistical mechanics, virtual angular velocity is defined as a derivative of the system's Hamiltonian with respect to the momentum

$$\frac{d\phi'}{dt'} = \frac{dH}{dp'_\phi}. \tag{A.68}$$

Substituting virtual angular velocity in the equation for the virtual angular momentum following expression is obtained

$$p_\phi = s_t \cdot I \frac{dH}{dp'_\phi}, \tag{A.69}$$

that can be simplified to

$$p_\phi = I \cdot s_t \frac{d[c_\phi^2 p'^2_\phi / 2I]}{dp'_\phi} \tag{A.70}$$

and later reduced to

$$p_\phi = s_t \cdot c_\phi [c_\phi \cdot p' \phi] = s_t \cdot c_\phi \cdot p_\phi. \tag{A.71}$$

Eliminating angular momentum on the both sides, the proportionality coefficient is given by

$$c_\phi = \frac{1}{s_t}. \tag{A.72}$$

The relationship between the real and virtual angular momentum becomes

$$p_\phi = \frac{p'_\phi}{s_t}. \tag{A.73}$$

The full system's Hamiltonian in terms of the virtual variable and available parameters is expressed as

$$H = \sum_i V^{-2/d} {s_t}^{-2} \frac{p'^2_i}{2m_i} + \sum_i {s_t}^{-2} \frac{{p'}_{i\phi}^{2}}{2I} + \Phi(V^{1/d} q', \phi') + \frac{p_{s_t}^2}{2M_s} + gkT \ln s_t + \frac{p_v^2}{2M_V} + P_{ex} V. \tag{A.74}$$

Using statistical mechanics principles together with the obtained relationships above, a set of equations of motion is obtained.

The virtual velocities are given by

$$\frac{dq'_i}{dt'} = \frac{\partial H}{\partial p'_i} = V^{-2/d} {s_t}^{-2} \frac{p'_i}{m_i}, \tag{A.75}$$

followed by the virtual forces

$$\frac{dp'_i}{dt'} = -\frac{\partial H}{\partial q'_i} = -\frac{\partial \Phi(V^{1/d} q', \phi')}{\partial q_i} V^{1/d}, \tag{A.76}$$

the virtual angular velocity is expressed as

$$\frac{d\phi'_i}{dt'} = \frac{\partial H}{\partial p'_{\phi_i}} = {s_t}^{-2} \frac{p'_{\phi_i}}{I}, \tag{A.77}$$

followed by the virtual torque

$$\frac{dp'_{\phi_i}}{dt'} = -\frac{\partial H}{\partial \phi'_i} = -\frac{\partial \Phi(V^{1/d} q', \phi')}{\partial \phi'}, \tag{A.78}$$

an additional degree of freedom s_t change rate is given by

$$\frac{ds}{dt'} = \frac{\partial H}{\partial p_{s_t}} = \frac{p_{s_t}}{M_s}, \tag{A.79}$$

followed by the conjugate momentum for s_t change rate

$$\frac{dp_{s_t}}{dt'} = -\frac{\partial H}{\partial s_t} = \left[V^{-2/d} {s_t}^{-2} \sum_i \frac{p'^2_i}{m_i} + {s_t}^{-2} \sum_i \frac{p'^2_{\phi_i}}{I} - gkT \right] / s_t, \tag{A.80}$$

volume change rate is given by

$$\frac{dV}{dt'} = \frac{\partial H}{\partial p_v} = \frac{p_v}{M_V}, \tag{A.81}$$

followed by the conjugate momenta for volume change rate

$$\frac{dp_v}{dt'} = -\frac{\partial H}{\partial V} = \left[V^{-2/d} {s_t}^{-2} \sum_i \frac{p'^2_i}{m_i} - \frac{\partial \Phi(q_i)}{\partial q_i} q_i \right] / (d \cdot V) - P_{ex}. \tag{A.82}$$

The equations above can be rewritten in terms of the virtual variables, if a derivative of (A.75) - (A.82) is taken with respect to the virtual time t'. Following set of equations is obtained if derivative is taken with respect to the real time t:

$$\ddot{q}'_i = V^{-1/d} \frac{f_i}{m_i} - \left[\frac{\dot{s}_t}{s_t} + \frac{2}{d} \frac{\dot{V}}{V} \right] \dot{q}'_i, \tag{A.83}$$

$$\ddot{\phi}' = \frac{f_{\phi_i}}{I} - \left[\frac{\dot{s}_t}{s_t} \right] \cdot \dot{\phi}'_i, \tag{A.84}$$

$$\ddot{s}_t = \frac{{\dot{s}_t}^2}{s_t} + s_t \left(V^{2/d} \sum_i m_i {\dot{q}'_i}{}^2 + \sum_i I {\dot{\phi}'_i}{}^2 - gkT \right) / M_s, \tag{A.85}$$

$$\ddot{V} = \frac{\dot{s}_t \dot{V}}{s_t} + \frac{{s_t}^2}{d \cdot M_V \cdot V} \times \left(\left[V^{2/d} \sum_i m_i \dot{q}_i'^2 + V^{1/d} \sum_i F_i \cdot q_i' \right] - P_{ex} \cdot d \cdot V \right), \tag{A.86}$$

where $\ddot{}$ denotes $\frac{\partial^2}{\partial t^2}$. The set of equations can be expressed in terms of the real variables, if relationships in (A.53) is used:

$$\ddot{q}_i = \frac{f_i}{m_i} - \left[\frac{\dot{s}_t}{s_t}\right] \left[\dot{q}_i - \frac{q_i}{Vd}\dot{V}\right] + \frac{1}{d}\frac{q_i \ddot{V}}{V} + q_i \left(\frac{\dot{V}}{Vd}\right)^2 (1-d), \tag{A.87}$$

$$\ddot{\phi}_i = \frac{\tau_i}{I} - \left[\frac{\dot{s}_t}{s_t}\right] \cdot \dot{\phi}_i, \tag{A.88}$$

$$\ddot{s}_t = \frac{{\dot{s}_t}^2}{s_t} + \frac{s_t}{M_s} \left(\sum_i m_i \left[\dot{q}_i - \frac{q_i}{Vd}\dot{V}\right]^2 + \sum_i I {\dot{\phi}_i}^2 - gkT \right), \tag{A.89}$$

$$\ddot{V} = \frac{\dot{s}_t \dot{V}}{s_t} + \frac{s_t^2}{d \cdot M_V \cdot V} \times \left(\left[\sum_i m_i \left[\dot{q}_i - \frac{q_i}{Vd}\dot{V}\right]^2 + \sum_i F_i \cdot q_i \right] - P_{ex} \cdot d \cdot V \right). \tag{A.90}$$

A.7 Program structure for the MB water model

Most of the standard routines were used form ‘D. C. Rapaport, ”The Art of Molecular Dynamics Simulation” (Second Edition), Cambridge University Press, UK, 2004’. That makes easier to modify and improve the code if user is familiar with the book. The book contains detailed explanations of the implemented and available algorithms, methodology and analysis methods.

The BN2D water model simulation code consists of the two header files `mb_class_defs.h` and `macro.h`, main file `main.cpp` and input file `input.txt`.

Five classes are available, the *MB* class is for MB model, the *NVE* and *NPT* classes for the relevant ensemble respectively, the *RDF* and *VACF* classes for the structural and dynamical properties respectively.

Derivatives of the potential with respect to the area can be found in Appendix A.8.

A.8 Potential derivatives

Integration of MD equations of motion requires forces that act on each particle. For the conservative potential fields the force acting on the i^{th} molecule is calculated as a negative gradient of the potential field. For the BN2D water model in addition to the translational force the derivative with respect to an angle ϕ produces the torque τ:

$$\tau = -\frac{\partial \Phi}{\partial \phi}. \tag{A.91}$$

The additional degree of freedom ϕ gives rise to the angular velocity ω. A corresponding moment of inertia I should be introduced in order to characterize the rotation of water molecules (I is an equivalent for the mass for rotation).

The formulas for thermodynamic properties depend, besides the kinetic energy, on the derivatives of the potential with respect to the area/volume. The first and second order derivatives of the potential energy with respect to the area are:

$$\frac{d\Phi}{dA} = \frac{1}{2A}\sum_{i=1}^{N-1}\sum_{j=i+1}^{N} dx\frac{d\Phi_{ij}}{dx} + dy\frac{d\Phi_{ij}}{dy}, \tag{A.92}$$

and

$$\frac{d^2\Phi}{dA^2} = \frac{1}{4A^2}\sum_{i=1}^{N-1}\sum_{j=i+1}^{N} dx^2\frac{d^2\Phi_{ij}}{dx^2} + 2\cdot dxdy\frac{d^2\Phi_{ij}}{dxdy} + dy^2\frac{d^2\Phi_{ij}}{dy^2}, \tag{A.93}$$

where Φ_{ij} is the potential, dx and dy are the distances along x and y direction between the i^{th} and j^{th} particles respectively.

A.8.1 Lennard-Jones part

The derivatives of the Lennard Jones part of the potential for i^{th} particle leads to:

$$F_{LJ} = -\nabla_q\Phi_{LJ} = -\frac{\Phi_{LJ}}{dr_{ij}}\frac{dr_{ij}}{dq}, \tag{A.94}$$

where $r_{ij} = \sqrt{(x_j - x_i)^2 + (y_j - y_i)^2}$ and q denotes x_i or y_i coordinate, the notation of ∇_q is either $\frac{\partial}{\partial x_i}$ or $\frac{\partial}{\partial y_i}$.

Using equation

$$\Phi_{LJ}(r) = \varepsilon_{LJ}\left(\left(\frac{\sigma_{LJ}}{r_{ij}}\right)^{12} - \left(\frac{\sigma_{LJ}}{r_{ij}}\right)^{6}\right), \tag{A.95}$$

where $\sigma_{LJ}, \varepsilon_{LJ}$ are the model parameters describing the length and depth of the potential and r_{ij} is the distance between interacting particles, we get

$$\frac{d\Phi_{LJ}}{dr_{ij}} = -24\cdot\varepsilon_{LJ}\cdot\sigma^6\left(2\,\sigma^6 r_{ij}^{-14} - r_{ij}^{-8}\right)\cdot r_{ij},$$

where the distance derivatives with respect to x_i and y_i are

$$\frac{dr_{ij}}{dx_i} = -\frac{x_j - x_i}{r_{ij}},$$

and

$$\frac{dr_{ij}}{dy_i} = -\frac{y_j - y_i}{r_{ij}}$$

respectively.

The second order derivatives of the LJ potential with respect to x_i and y_i components are

$$\frac{d^2\Phi_{LJ}}{dq^2} = 24 \cdot \varepsilon_{LJ} \cdot \sigma^6 \left(\frac{\left(26\,\sigma^6 - 7\,r_{ij}^6\right) \cdot \left(\frac{dr_{ij}}{dq}\right)^2}{r_{ij}^{14}} + + \frac{r_{ij}\left(-2\sigma^6 + r_{ij}^6\right)\left(\frac{d^2 r_{ij}}{dq^2}\right)}{r_{ij}^{14}} \right),$$

where

$$\frac{d^2 r_{ij}}{dx_i^2} = -\frac{(x_j - x_i)^2}{r_{ij}^3} + \frac{1}{r_{ij}}$$

and

$$\frac{d^2 r_{ij}}{dy_i^2} = -\frac{(y_j - y_i)^2}{r_{ij}^3} + \frac{1}{r_{ij}}.$$

The torque of Lennard-Jones potential is zero.

A.8.2 Hydrogen bonding part

The derivative of the HB part of the potential with respect to x_i, y_i, and ϕ_i are derived as follows

$$\frac{1}{\varepsilon_{HB}} \nabla_q \Phi_{HB} = \nabla_q G(r_{ij} - r_{HB}) \sum_{ij}^{N} G(\vec{i}_k \cdot \vec{u}_{ij} - 1) G(\vec{j}_l \cdot \vec{u}_{ij} + 1) + \tag{A.96}$$

$$+ G(r_{ij} - r_{HB}) \sum_{ij}^{N} \nabla_q G(\vec{i}_k \cdot \vec{u}_{ij} - 1) G(\vec{j}_l \cdot \vec{u}_{ij} + 1) + G(r_{ij} - r_{HB}) \sum_{ij}^{N} G(\vec{i}_k \cdot \vec{u}_{ij} - 1) \nabla_q G(\vec{j}_l \cdot \vec{u}_{ij} + 1).$$

Introducing new notation $h_i = \vec{i}_k \cdot \vec{u}_{ij}$ and $h_j = \vec{j}_l \cdot \vec{u}_{ij}$, the scalar products h_i and h_j become

$$h_i = \frac{(x_j - x_i) \cdot cos\ \phi_i + (y_j - y_i) \cdot sin\ \phi_i}{r_{ij}},$$

and

$$h_j = \frac{(x_j - x_i) \cdot cos\ \phi_j + (y_j - y_i) \cdot sin\ \phi_j}{r_{ij}}$$

respectively.

Using the notation above we expand the terms in (A.96) to

$$\nabla_q G(r_{ij} - r_{HB}) = \frac{dG(r_{ij} - r_{HB})}{dr_{ij}} \frac{dr_{ij}}{dq},$$

where

$$\frac{dG(r_{ij} - r_{HB})}{dr_{ij}} = -\frac{(r_{ij} - r_{HB})}{\sigma_{HB}^2} G(r_{ij} - r_{HB}).$$

The orientation dependent terms become

$$\nabla_q G(h_i - 1) = \frac{dG(h_i - 1)}{dh_i} \frac{dh_i}{dq} = -\frac{(h_i - 1)}{\sigma_\theta^2} G(h_i - 1) \frac{dh_i}{dq},$$

and

$$\nabla_q G(h_j + 1) = \frac{dG(h_j + 1)}{dh_i} \frac{dh_j}{dq} = -\frac{(h_j + 1)}{\sigma_\theta^2} G(h_j + 1) \frac{dh_j}{dq},$$

where

$$\frac{dh_i}{dx_i} = -\frac{cos\ \phi_i}{r_{ij}} - \frac{(x_j - x_i)\cdot cos\ \phi_i + (y_j - y_i)\cdot sin\ \phi_i}{r_{ij}^2}\frac{dr_{ij}}{dx_i},$$

$$\frac{dh_j}{dx_i} = -\frac{cos\ \phi_j}{r_{ij}} - \frac{(x_j - x_i)\cdot cos\ \phi_j + (y_j - y_i)\cdot sin\ \phi_j}{r_{ij}^2}\frac{dr_{ij}}{dx_i},$$

$$\frac{dh_i}{dy_i} = -\frac{sin\ \phi_i}{r_{ij}} - \frac{(x_j - x_i)\cdot cos\ \phi_i + (y_j - y_i)\cdot sin\ \phi_i}{r_{ij}^2}\frac{dr_{ij}}{dy_i},$$

$$\frac{dh_j}{dy_i} = -\frac{sin\ \phi_j}{r_{ij}} - \frac{(x_j - x_i)\cdot cos\ \phi_j + (y_j - y_i)\cdot sin\ \phi_j}{r_{ij}^2}\frac{dr_{ij}}{dy_i}.$$

The torque of the HB part for the i^{th} particle is

$$\nabla_{\phi_i}\Phi_{HB} = \varepsilon_{HB}\cdot G(r_{ij} - r_{HB})\cdot\sum_{ij}^{N}\nabla_{\phi_i}G(h_i - 1)G(h_j + 1),$$

where

$$\frac{dh_i}{d\phi_i} = \frac{-(x_j - x_i)sin\ \phi_i + (y_j - y_i)cos\ \phi_i}{r_{ij}}.$$

Introducing new notations $A = G(r_{ij} - r_{HB})$, $B = G(h_i - 1)$, $C = G(h_j + 1)$ the second order derivatives of the potential with respect to the coordinate for the HB part are obtained

$$\frac{d^2\Phi_{HB}}{dq^2} = \frac{d^2\left(A\sum B\cdot C\right)}{dq^2} = \nabla_q^2 A\sum B\cdot C + A\sum\nabla_q^2 B\cdot C + A\sum B\cdot\nabla_q^2 C + \tag{A.97}$$
$$+2\left(A\sum\nabla_q B\cdot\nabla_q C + \nabla_q A\sum B\cdot\nabla_q C + \nabla_q A\sum\nabla_q B\cdot C\right).$$

The second order derivative of the Gauss function $G(f(q)) = e^{-\frac{f(q)^2}{2\sigma^2}}$ is

$$\frac{d^2G(f(q))}{dq^2} = \frac{G(f(q))\left((-\sigma^2 + f(q)^2)\cdot\left(\frac{df(q)}{dq}\right)^2 - \sigma^2\cdot f(q)\cdot\left(\frac{d^2f(q)}{dq^2}\right)\right)}{\sigma^4},$$

while

$$\frac{d^2h_i}{dx^2} = (y_i - y_j)\left(\frac{sin(\phi_i)(-2(x_i - x_j)^2 + (y_i - y_j)^2)}{r_{ij}^5} + \frac{3\ \cos(\phi_i)(x_i - x_j)(y_i - y_j)}{r_{ij}^5}\right),$$

$$\frac{d^2h_i}{dy^2} = (x_i - x_j)\left(\frac{cos(\phi_i)((x_i - x_j)^2 - 2(y_i - y_j)^2)}{r_{ij}^5} + \frac{3\ \sin(\phi_i)(x_i - x_j)(y_i - y_j)}{r_{ij}^5}\right),$$

$$\frac{d^2h_j}{dx^2} = (y_i - y_j)\left(\frac{sin(\phi_j)(-2(x_i - x_j)^2 + (y_i - y_j)^2)}{r_{ij}^5} + \frac{3\ \cos(\phi_j)(x_i - x_j)(y_i - y_j)}{r_{ij}^5}\right),$$

$$\frac{d^2h_j}{dy^2} = (x_i - x_j)\left(\frac{cos(\phi_j)((x_i - x_j)^2 - 2(y_i - y_j)^2)}{r_{ij}^5} + \frac{3\ \sin(\phi_j)(x_i - x_j)(y_i - y_j)}{r_{ij}^5}\right).$$

A.9 Predictor-Corrector method

Predictor-Corrector (PC) methods use information from the previous timesteps (here Adams approach is described [59]).

Predictor step for the time layer $t+dt$ is an extrapolation of the information obtained from the previous timesteps and can be expressed as

$$x(t+dt) = x(t) + dt \cdot \dot{x}(t) + dt^2 \sum_{i=1}^{k-1} \alpha_i \ddot{x}(t+[1-i]dt), \tag{A.98}$$

where $\ddot{x}$ is acceleration and coefficients α_i are already known [59]. These coefficients were obtained by satisfying $k-1$ set of equations

$$\sum_{i=1}^{k-1} (1-i)^q \alpha_i = \frac{1}{(q+1)(q+2)}, \tag{A.99}$$

where $q = 0, ..., k-2$.

The predictor step for the velocity is given by

$$dt \cdot \dot{x}(t+dt) = x(t+dt) - x(t) + dt^2 \sum_{i=1}^{k-1} \alpha'_i \ddot{x}(t+[1-i]dt), \tag{A.100}$$

where α'_i is already known and satisfied following relationship

$$\sum_{i=1}^{k-1} (1-i)^q \alpha'_i = \frac{1}{(q+2)}. \tag{A.101}$$

After acceleration evaluation at the next timestep $\ddot{x}(t+dt)$ corrector step is applied to the coordinate

$$x(t+dt) = x(t) + dt \cdot \dot{x}(t) + dt^2 \sum_{i=1}^{k-1} \beta_i \ddot{x}(t+[2-i]dt), \tag{A.102}$$

followed by the correction of the velocities

$$dt \cdot \dot{x}(t+dt) = x(t+dt) - x(t) + dt^2 \sum_{i=1}^{k-1} \beta'_i \ddot{x}(t+[2-i]dt), \tag{A.103}$$

where β_i and β'_i are already known by satisfying

$$\sum_{i=1}^{k-1} (2-i)^q \beta_i = \frac{1}{(q+1)(q+2)}, \tag{A.104}$$

and

$$\sum_{i=1}^{k-1} (2-i)^q \beta'_i = \frac{1}{(q+2)}. \tag{A.105}$$

For the NPT simulation of the BN2D model k was set equal to 4.